JARNO REUNA

ANTI-REFLECTIVE COATINGS FOR MULTI-JUNCTION SOLAR CELLS

Master of Science thesis

Examiners: Prof. Mircea Guina and D.Sc. Ville Polojärvi
Examiners and topic approved by the Faculty Council of the Faculty of Natural Sciences
on 17th August 2016

Abstract

JARNO REUNA: Anti-reflective Coatings for Multi-junction Solar Cells
Tampere University of Technology
Master of Science thesis, 127 pages, 9 Appendix pages
November 2016
Master's Degree Programme in Science and Engineering
Major:Advanced Engineering Physics
Examiners: Prof. Mircea Guina, D.Sc. Ville Polojärvi
Keywords: Anti-reflective Coating, Thin Film, Multi-junction Solar Cell, III-V Semiconductors, EBE, PECVD, AFM, SEM, I-V measurements

Multi-junction solar cells (MJSC) are dominating technology for energy production in space applications and hold important prospects for terrestrial concentrated photovoltaics used in direct solar irradiance areas. To increase their efficiency, these solar cells require anti-reflective (AR) coatings that minimize surface reflections. This thesis focuses on fabrication of different dielectric thin films and their material characterization for AR coatings. The results are used in design and fabrication of effective coatings for MJSCs.

In particular, the work focused on MgF_2-based coatings and studying the effects of substrate temperature on the refractive index and mechanical properties of MgF_2 films deposited by electron beam evaporation. Similarly, we studied the process parameters of nanoporous SiO_2 deposited by plasma-enhanced chemical vapor deposition at different substrate temperatures and precursor gas ratios. Then for the two different spinnable siloxane coating, we studied parameters including spinning speed and lid position. The study revealed that MgF_2 refractive index increases with substrate temperature until temperature of over 250 °C. For SiO_2 the decrease in temperature and altered gas ratio generated porous structure that lowered the refractive index.

The characterization results were used to simulate and optimize four different AR coatings for triple-junction InGaP/GaAs/GaInNAsSb solar cell using Essential Macleod design program. The coatings were MgF_2/TiO_2, nanoporous SiO_2 with TiO_2, siloxane layer with TiO_2 and a triple layer coating of $MgF_2/Al_2O_3/TiO_2$. The coatings were compared to the conventional SiO_2/TiO_2 AR coating. The coated cells were tested with solar simulator under AM1.5D spectrum and all coating designs showed proper functionality.

On average, the coatings reduced the amount of the reflected light to a one third of the initial reflectance. This directly increases the current density produced by the cells, approximately about 30 %. The maximum power and the efficiency of the cell are improved roughly the same amount. It was shown that the studied materials are suitable constituents for AR coatings and that their optical and mechanical properties are tunable via fabrication parameters. The results of this thesis enable improving AR coating designs via optimization and computer simulation, according to the cell structure in question.

Tiivistelmä

JARNO REUNA: Heijastamattomat pinnoitteet moniliitosaurinkokennoille
Tampereen teknillinen yliopisto
Diplomityö, 127 sivua, 9 liitesivua
Marraskuu 2016
Teknisluonnontieteellinen koulutusohjelma
Pääaine: Teknillinen Fysiikka
Tarkastajat: Prof. Mircea Guina, TkT. Ville Polojärvi
Avainsanat: Heijastamaton pinnoite, ohutkalvo, moniliitosaurinkokenno, III-V -puolijohteet, EBE, PECVD, AFM, SEM, virta-jännitemittaukset

Tutkimuksen kohteena oli korkean hyötysuhteen moniliitosaurinkokennojen heijastamattomat pinnoitteet. Päätavoitteena oli valmistaa ja optimoida dielektrisiä ohutkalvoja ja karakterisoida niiden optisia ja mekaanisia ominaisuuksia heijastamattomia pinnoitteita varten. Kerätyn datan avulla suunniteltiin ja tuotettiin heijastamattomia pinnoitteita optoelektoniikan tutkimuskeskuksessa valmistettaville aurinkokennoille.

Tyhjöhöyrystetyn magnesiumfluoridin (MgF_2) ominaisuuksia tutkittiin kasvatuslämpötilan funktiona ellipsometrian ja eri mikroskopioiden avulla. Vastaavasti nanohuokoisesta piidioksidista (SiO_2) tutkittiin kasvatuslämpötilan ja prekursiivisten kaasujen suhteen vaikutusta taitekertoimeen ja rakenteeseen. Myös siloksaaneihin pohjautuvien spinnattavien pinnotteiden ominaisuuksia tutkittiin spinnausnopeuden ja kannen asennon funktiona. Selvitettyjä taitekertoimia sovellettiin heijastamattomien pinnoitteiden simuloinnissa ja optimoinnissa, joka tehtiin Essential Macleod ohutkalvojen optimointiohjelmalla. Ohutkalvopinnoitteita testattiin InGaP/GaAs/GaInNAsSb kolmiliitoskennolla, jonka virta-jännite ominaisuuksia mitattiin aurinkosimulaattorilla AM1.5D spektriä vastaavalla irradianssilla. Testaukseen valittiin neljä erilaista pinnoitetta, jotka olivat MgF_2/TiO_2 kaksoispinnoite, nanohuokoinen piidioksidi titaniumoksidin kanssa SiO_2/TiO_2, siloksaanipinnoite yhdessä TiO_2:n kanssa, sekä kolmoispinnoite $MgF_2/Al_2O_3/TiO_2$. Tuloksia verrattiin aiemmin käytettyyn SiO_2/TiO_2 pinnoitteeseen.

Pinnoitteet laskivat keskimäärin kennon pinnalta tapahtuvan heijastuksen kolmannekseen siitä, mitä se olisi ollut ilman pinnoitetta. Tämä näkyi suoraan kennojen tuottamassa virrantiheydessä noin 30 %:n kasvuna. Lisäksi pinnoitteet paransivat kennojen maksimitehoa ja hyötysuhdetta suunnilleen samassa suhteessa.

Tutkimuksen perusteella tarkastellut materiaalit ovat erittäin hyvin soveltuvia moniliitosaurinkokennojen heijastamattomiin pinnoitteisiin ja lisäksi niiden optisia ja mekaanisia ominaisuuksia voidaan säädellä valmistusparametrien avulla. Pinnoitteiden kerrospaksuuksia ja prosessiparametreja optimoimalla voidaan saavuttaa entistä parempia tuloksia, kun pinnoitteet suunnitellaan kennokohtaisesti vastaamaan liitosten virtasovituksia.

Preface

This work was conducted at the Optoelectronics Research Centre (ORC) that belongs to the Faculty of Science and Environmental Engineering of Tampere University of Technology. I'd like to thank both the Fortum foundation and Tekes project BrightSky for financial support and D.Sc Pekka Savolainen, the director of ORC, for making this work possible.

For the opportunity to make this thesis and for a great thesis subject I want to thank professor Mircea Guina, who supervised the thesis and provided support along the process. For instructions and guidance through the project D.Sc Ville Polojärvi deserves my immense gratitude. For support and advice I thank D.Sc Antti Tukiainen and D.Sc Arto Aho, whom shared their substantial expertise on solar cells. The rest of the solar cell processing team, M.Sc Timo Aho, M.Sc Marianna Raappana and B.Sc Lauri Hytönen, have my thanks for introducing the practical processes in fabrication and characterization of thin films. M.Sc Riku Isoaho is to be thanked for helping me in the I-V measurements. I thank professor Tapio Niemi for sharing his knowledge of thin films and providing useful contacts. For collaboration in ellipsometric measurements I thank Ph.D Pertti Pääkkönen from the University of Eastern Finland. Also the Pibond corporation has my thanks for providing siloxane samples. Addition to that I'll thank all the other personnel that helped me along the way. If there was a question, I always received a clarifying answer. All in all I'd like to thank the entire ORC for an excellent atmosphere, that makes every work day more than worth it.

Lastly I'll thank my family and friends for support during the process and especially Susanna for being there for me.

Tampere, November 23rd, 2016

Jarno Reuna

Table of Contents

1 Introduction **1**

2 Optical Thin Films and Applications **4**

2.1 Theory of Light and Matter Interaction 4

2.1.1 Dielectric Medium and Light 7

2.1.2 Polarization of Light and Reflectivity 11

2.2 Anti-reflective Coatings 18

2.2.1 Background of Optical Thin Films 19

2.2.2 Designing an Anti-reflective Coating 25

2.3 Multi-junction Solar Cells 28

2.3.1 Principle of Operation and General Structure 30

2.3.2 Properties of Multi-junction Solar Cells 37

3 Manufacturing and Characterization Methods **41**

3.1 Fabrication of Anti-reflective Coatings 41

3.1.1 Electron Beam Evaporation 41

3.1.2 Plasma Enhanced Chemical Vapor Deposition 43

3.1.3 Spinning Method for Thin Film Manufacture 45

3.1.4 Simulation and Optimization of the Anti-reflective Coatings . 46

3.2 Characterization Methods of Thin Films and Solar Cells with Anti-reflective Coatings 49

3.2.1 Ellipsometric Measurements and Spectrophotometry 49

3.2.2 Atomic Force Microscope 56

3.2.3 Scanning Electron Microscope 59

3.2.4 Solar Cell Characterizations 62

4 Material Characteristics and Coating Analysis **64**

4.1 Thin Film Characterizations 64

4.1.1 Characterization of MgF_2 Thin Films 64

4.1.2 Characterization of SiO_2 Nanoporous Films 77

4.1.3 Characterization of SC510K and SC800i Siloxanes 86

4.2 The Applicability of the Anti-reflective Coatings for Multi-junction Solar Cells . . . 94
4.2.1 The Anti-reflective MgF_2/TiO_2 Double Layer . . . 100
4.2.2 The Nanoporous SiO_2 Based Anti-reflective Coating . . . 102
4.2.3 The Siloxane SC510K Based Anti-Reflective Coating . . . 105
4.2.4 The $MgF_2/Al_2O_3/TiO_2$ Triple Layer Anti-Reflective Coating . 107
4.2.5 Comparison of the different Anti-reflective Designs . . . 110

5 Conclusions 114

Appendix A Growth Parameter Tables 128

Appendix B Additional AFM Data 130

Appendix C Physical constants 136

List of abbreviations and symbols

AFM	Atomic Force Microscope
ALD	Atomic Layer Deposition
AM	Air Mass
AR	Anti-reflective
BSE	Back Scattered Electrons
CVD	Chemical Vapor Deposition
CPV	Concentrated Photovoltaics
EBE	Electron Beam Evaporator
EBR	Edge Bead Remover
EMA	Effective Medium Approximation
FESEM	Field Emission Scanning Electron Microscope
FWOT	Full Wavelength Optical Thickness
HR	Highly Reflective
IBS	Ion-Beam Sputtering
IAD	Ion-Beam Assisted Deposition
IR	Infrared
I-V	Current-Voltage
MBE	Molecular Beam Epitaxy
MJSC	Multi-junction Solar Cell
NIL	Nano-Imprint Lithography
ORC	Optoelectric Research Center
QWOT	Quarter Wavelength Optical Thickness

PE	Primary Electrons
PECVD	Plasma Enhanced Chemical Vapor Deposition
PL	Photoluminescence
PVD	Physical Vapor Deposition
PV	Photovoltaic
RAE	Rotating Analyzer Ellipsometer
RT	Room Temperature
SC	Solar Cell
SE	Secondary Electrons
SEM	Scanning Electron Microscope
SPM	Scanning Probe Microscope
TE	Transverse Electric
TM	Transverse Magnetic
TUT	Tampere University of Technology
URA	Universal Reflectance Accessory
UV	Ultraviolet
VASE	Variable Angle Spectroscopic Ellipsometer

α	absorption coefficient
δ	phase thickness
Δ	phase change
ϵ	dielectric constant
η	tilted optical admittance
η_{eff}	efficiency
λ	wavelength
μ	magnetic permeability
ν	frequency
ω	angular frequency
ϕ	phase

Ψ relative amplitude change

ρ_d charge density

ρ amplitude reflection coefficient

σ specific conductivity

τ amplitude transmission coefficient

θ_i angle of incident

θ_r angle of reflection

θ_t angle of transmission

Θ photon flux

$< a >$ average height

B normalized electric field

$\mathbf{B}$ magnetic induction vector

c speed of light

C normalized magnetic field

d film thickness

$\tilde{d}$ periodic term in ellipsometry

d_{quartz} film thickness measured by the crystal monitor

$\mathbf{D}$ electric displacement vector

$\mathbf{E}$ electric field vector

E_g band gap energy

$\mathcal{E}$ electric field amplitude

$\mathscr{E}$ tangential component of electric field amplitude

ΔE energy transition

EQE external quantum efficiency

FF fill factor

FF_0 ideal fill factor

h Planck's constant

$\hbar$ reduced Planck's constant

$\mathbf{H}$	magnetic field vector
$\mathcal{H}$	magnetic field amplitude
$\mathscr{H}$	tangential component of magnetic field amplitude
i	imaginary unit
I_0	saturation current
$I_{01/02}$	diode currents
I_{int}	intensity
I_m	current corresponding to the maximum power
I_{ph}	photocurrent
I_{sc}	short-circuit current
IQE	internal quantum efficiency
$\mathbf{j}$	electric current density vector
J_{sc}	short-circuit current density
k	extinction coefficient
k_B	Boltzmann's constant
K	surface kurtosis
l	distance
$\tilde{n}$	complex refractive index
n	refractive index
p	parallel
p	pressure
P	power
P_{opt}	optical power
P_{max}	maximum power
q	charge of an electron
r_s	shunt resistance term
R	reflectance
R_s	series resistance

R_p	shunt or parallel resistance
ra	roughness average
$rmsr$	root mean square of roughness
t	time
T	temperature
T_{approx}	approximated tooling factor
T_F	tooling factor
T_s	substrate temperature
T_{tr}	transmittance
s	perpendicular
S	surface skewness
v	velocity
V	voltage
V_m	voltage corresponding to the maximum power
V_{oc}	open-circuit voltage
y	optical admittance
$\mathcal{Y}$	input optical admittance
$\mathscr{Y}$	optical admittance of free space

1. Introduction

The optical thin film design for different technical applications has become increasingly important for these days optics. With different materials and careful optimization one can make either highly reflective (HR) or completely anti-reflective (AR) films with different amounts of transmission and absorption of light, either for a specific wavelength or a wider wavelength range. The applications of optical thin films vary from laser mirrors to AR coatings for solar cells and lenses and can be found almost in every optical device. [1] To fabricate the film with wanted properties one have to choose proper refractive indices, layer thicknesses and number of layers. [2] This requires characterization of available materials and optimized design of the layer structure.

As applications for thin films span over a large number of technological devices one specifically important section is different surface structures from omniphobic layers [3, 4] to anti-reflective coatings [5–8]. The latter is especially significant for solar cells, that are stepping up in the green energy production faster than any other renewable energy source at the moment. In solely the year 2014 the added capacity was 50 GW, that corresponded to about 25 % increase in the total global capacity of solar power. In ten years (2005–2015) the global photovoltaic power production capacity has increased from 5.1 GW to 227 GW. Together all the renewables covered 785 GW of the global power capacity at the end of 2015. It was estimated that the solar generated power would be 1.2 % of the amount of the total electricity produced in 2015 worldwide. [9] Most of this photovoltaic (PV) power is produced with conventional silicon solar cells, but other technologies are constantly being studied for different circumstances and as competitors for silicon PV. These technologies include other semiconductor cells, thin film cells, organic cells, perovskite cells, dye cells and lastly the multi-junction solar cells (MJSC), that combine different subcells to convert as large portion of sunlight as possible. Most efficient of these all are the MJSCs by far, as their record efficiencies extend to 30–46 %. [10] They are also quite expensive solar cells to manufacture, which limits their usage to concentrated photovoltaics and space applications. [11] There, however, their performance is excellent and the prospects appear to be even better, as calculated theoretical efficiencies for MJSCs with concentrators reach up to 60 % with four or more junctions. [12] To

do so the MJSCs in question have to have properly designed AR coatings, as an uncoated semiconductor surface roughly reflects about 30 % of the incoming light.

The structure of a typical MJSC has the subcells connected in series, so the subcell producing the lowest current limits the current of the other subcells, thus reducing the total efficiency of the MJSC. In designing an optimal AR coating for MJSC the goal is to maximize the current generated by the limiting subcell. The challenge in this is to calculate the modeled reflectance, as this requires finding out the optical constants of the used dielectrics and semiconductors. [5] For design purposes one can rely either on libraries of material data or characterize the wanted coating materials itself. The latter would be preferable, as the manufacturing processes affect the properties of thin films and the most reliable data is gained from characterization of similarly deposited materials that are supposed to be used in the actual coating. Overall requirements for AR coatings include

- Broadband design, covering the solar spectrum from 200 to 2000 nm, with materials that have only very low or zero absorbance
- Wide angular range, so that as much light as possible is directed to the cell
- Durability of 20 to 30 years under long UV exposure, temperature changes and humidity
- Affordability, so that the coating does not significantly add the total costs of the solar cell,

which all have to be taken into account when designing a coating. [13] For well current matched MJSCs the requirement for a suitable AR coating is that its reflectance is as low and flat as possible across the spectral range of interest, as long as the current matching is maintained. [5] These are the frames for the focus of this thesis and give the directions, what has to be done.

The goal of this thesis is to study relatively easy and cheap to manufacture AR coatings for multi-junction solar cells and to find out if these candidates could have use in real applications. The work is conducted at Tampere University of Technology (TUT) at Optoelectronics Research Center (ORC). Optoelectronics is an an area of technology that uses both semiconductor electronics and optical components to achieve functional devices that are not attainable with electronics alone. The most notable example of optoelectronics is the solid state laser and its applications in laser disc systems among other devices. [14] The study included material characterization for AR coating design, designing the coatings and fabricating and comparing the actual AR coatings.

The thesis is divided in four chapters after this introduction. The second chapter introduces some of the optical theories behind light and matter and presents some

insight considering anti-reflective coatings and semiconductor solar cells. The third chapter includes the manufacturing and characterization methods used in this study and presents some background for the measurement systems and manufacturing devices. The fourth chapter is divided up sections that show the results for the studied coatings and their characterizations. In the fifth chapter I present the conclusions and summarize this work and possible headings for future research.

2. Optical Thin Films and Applications

To understand and study phenomena based on interaction of solids and light it is necessary to introduce some basics considering these two. In this chapter I present some physics related to optics and shortly represent the principles of optical thin films and semiconductor solar cells. As this thesis studies anti-reflective coatings for multi-junction solar cells the emphasis is on these. More general and thorough presentations of these subjects can be found for example from the sources used in this thesis such as Hecht's Optics [15], Macleod's Optical Thin Film Filters [1] and several handbooks [14, 16–18]. The field of study is vast, but with available literature one can get a rather good perspective of its major phenomena. The emphasis of the used approach in this thesis is to keep the examination of the phenomena as conceptual as possible, but some formulas and mathematics are necessary to thoroughly handle the subject. All the values of the used constants can be found in appendix C in table C.1.

2.1 Theory of Light and Matter Interaction

According to our current knowledge light can be stated to be electromagnetic waves as well as massless particles called photons. This intriguing nature of light is called wave-particle dualism and it has had a great impact on the development of modern physics, most notably due to the photoelectric effect explained by Einstein in 1905 [19]. Depending the phenomenon and our interests we usually examine either of light's nature at a time although both must be noted. Optics in general has been divided in four different approaches with their own postulates and approximations. The different levels from the simpliest to the most detailed are ray optics, wave optics, electromagnetic optics and quantum optics. [20] Each of these has suitabilities for different kind of situations and problems. In this thesis the different approaches are not further distinguished, but only applied the ones most fitting for the phenomenon under inspection. In fig. 2.1 there is a representation of the

electromagnetic spectrum.

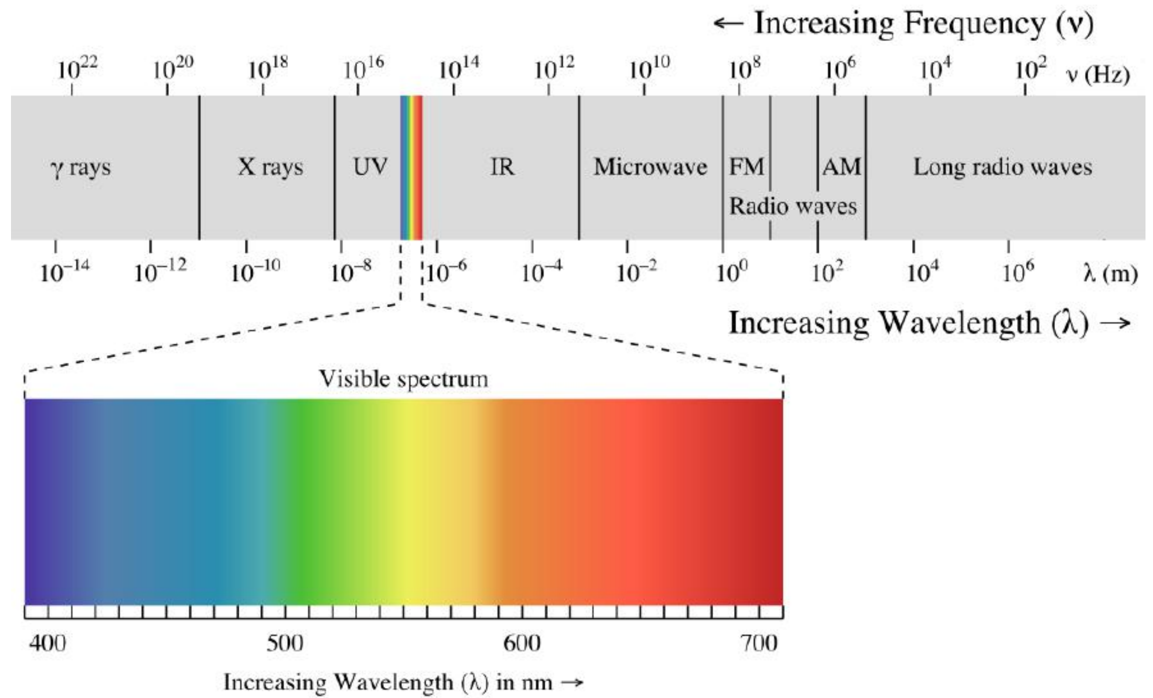

Figure 2.1 *The electromagnetic spectrum from gamma rays to long radio waves [21].*

The spectrum is divided in different sections according to their wavelength or frequency such as X-rays, ultraviolet (UV) light, visible light, infrared (IR) light and microwaves. The borders between the sections are not strictly defined, but usually when we are speaking of light it means the radiation in the wavelength range from 0.01 μm to 1 mm. [16] This covers the spectrum from UV to IR. When we are describing light as an electromagnetic wave it has two distinct parts to be considered. The other one is the magnetic field and the other is the electronic field. They both are oscillating orthogonally of the direction of propagation and each others. The simplified model is presented in figure 2.2 and the z axis is usually denoted as the direction of propagation.

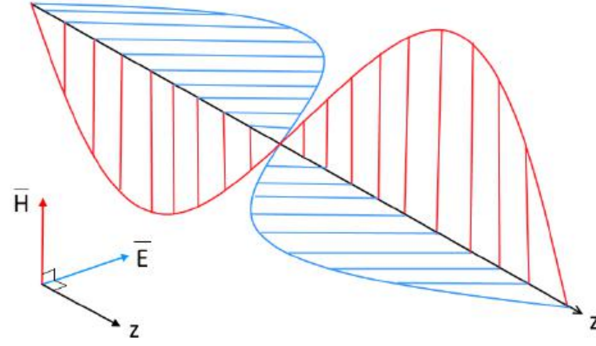

Figure 2.2 *Propagating light illustrated as an electromagnetic wave.*

This electromagnetic wave is most often presented with two equations, that are:

$$\mathbf{E} = \mathcal{E} \exp[i\omega(t - z/v + \phi)] \tag{2.1}$$

$$\mathbf{H} = \mathcal{H} \exp[i\omega(t - z/v + \phi)], \tag{2.2}$$

where **E** describes the electric field and **H** the magnetic field of the wave propagating along the z-axis. Here i is the imaginary unit, $\mathcal{E}$ and $\mathcal{H}$ field amplitudes, ω presents angular frequency, t is time, v velocity and lastly ϕ means the phase of the wave. This form of the equations 2.1 and 2.2 applies to linearly polarized plane harmonic wave. [1]

In order to describe matter light interaction we also need three other vector quantities that are the electric displacement **D**, the magnetic induction **B** and the electric current density **j**. With these five basic quantities one can present material behavior under electromagnetic field. The relations combining the different quantities are called material equations:

$$\mathbf{j} = \sigma\mathbf{E} \tag{2.3}$$

$$\mathbf{D} = \epsilon\mathbf{E} \tag{2.4}$$

$$\mathbf{B} = \mu\mathbf{H}. \tag{2.5}$$

The σ, ϵ and μ are known as spesific conductivity, dielectric constant and magnetic permeability respectively. The two latter material quantities are also defined as:

$$\epsilon = \epsilon_r\epsilon_0 \tag{2.6}$$

$$\mu = \mu_r\mu_0 \tag{2.7}$$

and they are connected according to an equation:

$$c = \frac{1}{\sqrt{\epsilon_0 \mu_0}}, \tag{2.8}$$

where c is the speed of light in vacuum. Values ϵ_0 and μ_0 are constants of free space and ϵ_r and μ_r are relative characteristics of materials. [1] With the material charasteristics σ, ϵ and μ different substances can be divided in several material groups, that differ in their physical properties. Materials for which $\sigma \neq 0$ are called conductors and main group of conductors is metals. Conductivity, however, is a temperature related magnitude and in metals the conductivity decreases when temperature increases. In the other important group of conductors this is vice versa and these materials are called semiconductors. The substances with negligibly small σ are called either insulators or dielectrics. Their response to the electromagnetic field is therefore completely determined by ϵ and μ. With other than magnetic materials μ closes to unity and ϵ governs the substance's optical properties. In this thesis we focus on dielectrics as thin film materials and touch on semiconductors as solar cell components. [22]

The next two sections handle the light interacting with dielectric media and some overall properties of light when it faces and propagates into a new material.

2.1.1 Dielectric Medium and Light

As the light consists two electromagnetic fields, that are represented with two vectors 2.1 and 2.2 and materials are characterized through equations 2.3, 2.4 and 2.5, we need a way to describe interactions between light and matter. For this purpose I present here the Maxwell's equations for anisotropic media, that hold for linearly polarized plane wave

$$\nabla \times \mathbf{H} = \mathbf{j} + \frac{\partial \mathbf{D}}{\partial t} \tag{2.9}$$

$$\nabla \times \mathbf{E} = -\frac{\partial \mathbf{B}}{\partial t} \tag{2.10}$$

$$\nabla \cdot \mathbf{D} = \rho_d \tag{2.11}$$

$$\nabla \cdot \mathbf{B} = 0. \tag{2.12}$$

The ρ_d means here the charge density and should not be mixed up with the reflection amplitude coefficient ρ, that is introduced later on. Most handling of electromagnetic phenomena comes down to these four equations and thorough derivations and presentations of these are included in almost every book [1, 15, 20, 23] dealing with

optical or other electromagnetic properties of matter, but for a full and complete treatment of the subject I recommend the Principle of Optics by Born and Wolf [22].

Through equations 2.1, 2.4, 2.8 and 2.11 can be derived that the speed v of a linearly polarized plane harmonic wave in media is defined by a dimensionless parameter

$$\tilde{n} = \frac{c}{v} = n - ik, \tag{2.13}$$

that is called the complex refractive index. Its real part is n and complex part k is called the extinction coefficient. Often the n is called just *the refractive index* because for ideal dielectrics $\tilde{n} = n$. This is due to the fact that the extinction coefficient k is linked to the absorption of light and ideal dielectrics are completely transparent. For real dielectrics the k has some low values, but in theoretical examination it is approximated to be zero. The refractive indices for materials are always chosen to be positive as from physical point of view that is the most practical convention. The $\tilde{n}$ for air is nearly equal to one and all other natural materials are greater than that. [1] Recently there has been research on metamaterials with negative refractive indices [24–26], but they are not further considered here. The refractive index is related to the optical admittance y, that is also a material quantity, as

$$y = \mathscr{Y}\tilde{n}, \tag{2.14}$$

where $\mathscr{Y}$ is the optical admittance of free space as $\mathscr{Y} = (\epsilon_0/\mu_0)^{\frac{1}{2}}$. Other way to describe the optical admittance is to write

$$\eta = \frac{\mathcal{H}}{\mathcal{E}}. \tag{2.15}$$

The optical admittance basically is the relation between electric and magnetic field amplitudes, $\mathcal{E}$ and $\mathcal{H}$ respectively, and it provides a good tool for analytical approaches of reflection and transmission. The reason why the eq. 2.14 uses y and eq. 2.15 uses η is that $\eta = y$ only at the normal incidence angle and in other cases the polarization of light and the incidence angle θ_i must be taken into account.

Now when we consider the equation 2.1 with equation 2.13 and presume that the starting phase ϕ is 0, we can write

$$\mathbf{E} = \mathcal{E}\exp[i\omega t - (2\pi\tilde{n}/\lambda)z)] \tag{2.16}$$

which gives us the wavelength in free space as $\lambda = 2\pi c/\omega$. When the expression $n - ik$ is inserted in place of $\tilde{n}$, it yields

$$\mathbf{E} = \mathcal{E}\exp[-(2\pi k/\lambda)z)]\exp[i\omega t - (2\pi n/\lambda)z)], \tag{2.17}$$

where the physical meaning of k is realized as its existence exponentially decreases the propagating amplitude. This means that part of the light is absorbed in the medium and the relation between $\tilde{n}$ and absorption comes with k as

$$\alpha = \frac{4\pi k}{\lambda}, \tag{2.18}$$

where α is the absorption coefficient. The absorption coefficient relates to the loss of intensity according to the Beer-Lambert's law

$$I_{int} = I_{int_0} \exp(\alpha l), \tag{2.19}$$

where I_{int_0} is the intensity of the incident beam of light and l is the distance traveled within the medium. [22] Because the main target of our theoretical approach is to derive sufficient background for dielectric AR coating designs, the media is further considered lossless and there's no k in $\tilde{n}$. This yields the ideal dielectric characteristics and therefore the refractive index is referred only as n.

When light meets an interface there are several important phenomena taking place and they are firmly linked to the refractive indices of the facing media. The light can either be reflected from the surface to the angle of θ_r or be transmitted into the next medium in the angle of θ_t. An illustration of these events is presented in fig. 2.3. It is stated by the law of reflection that $\theta_i = \theta_r$, where θ_i is the incident angle. [15]

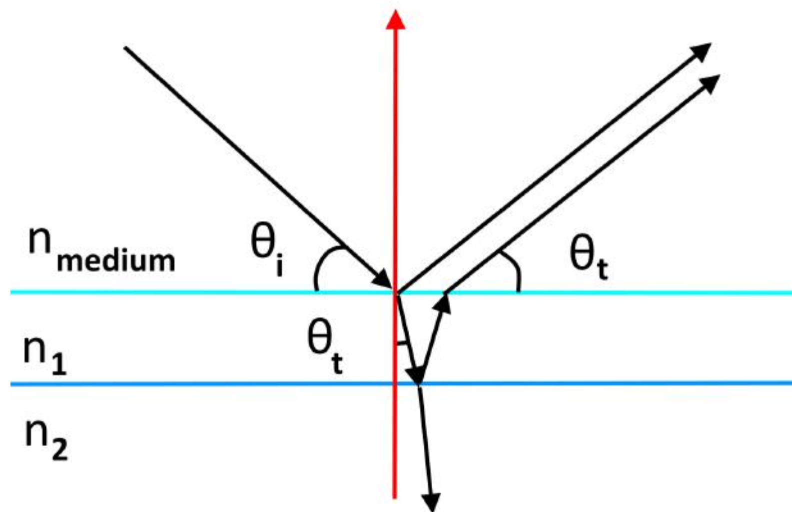

Figure 2.3 *Light beam arriving to an interface of three mediums.*

The reflection and transmission angles are dependent of the beam's angle of incidence θ_i and the refractive indices n_i and n_j of the mediums, where i and j are

indexing numbers for the mediums. This dependence can be formalized to an equation:

$$\frac{\sin\theta_i}{\sin\theta_j} = \frac{n_j}{n_i} \tag{2.20}$$

that is known as the law of refraction or the Snell's law and it applies most of the time when light reaches a two medium interface. [15] Exception of this are birefringent materials that divide the incident beam into two separate beams called the ordinary beam, that follows the Snell's law and propagates to the direction of θ_t, and extraordinary beam that propagates to a different direction of θ_e. [20] The birefrigence, however, is beyond the scope of this thesis and we presume the behavior of ordinary beams as we inspect light propagating in a medium.

Most materials have a characteristics called dispersion. This means that the refractive index n of that medium is dependent on the frequency ν of the entering light. As the speed of light in a medium can be stated to be $v = \nu\lambda$ and it relates to the refractive index accordingly $v = c/n$, this results the refractive index also to be a function of the light's wavelength, as $n(\lambda) = c/\nu\lambda$. Because of different n for each wavelength λ polychromatic light distributes to different angles of θ_t as stated by the Snell's law 2.3. This leads to various optical paths for different beams of light and due to this the visible light can be distributed with a prism as illustrated in the fig. 2.4. Another relatively important phenomenon caused by dispersion is the pulse broadening in optical fibers. [20]

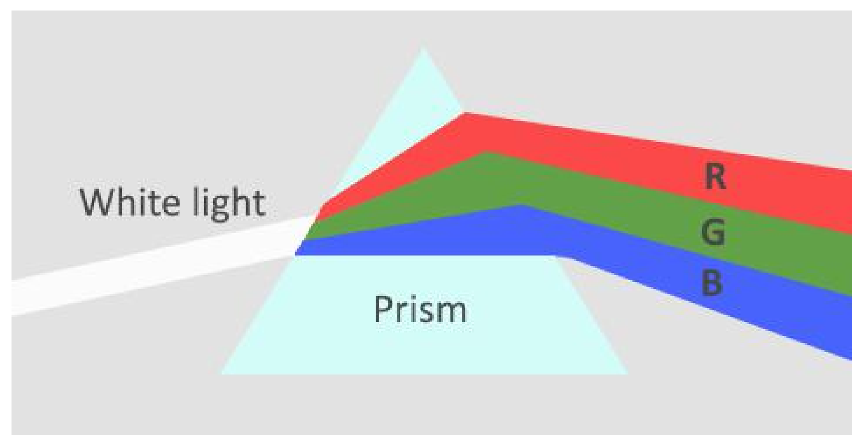

Figure 2.4 *As white light enters dispersive medium it refracts according to the dispersion distribution $n(\lambda)$. A good example of this is a prism and visible light.*

Practically every material has some amount of dispersion and typically dielectrics have a higher refractive index at the UV range that decreases when moved towards the IR range. This is due to the fact, that despite the approximated zero absorbance for theoretical examination, the dielectrics have some absorptance at the UV bandwidth (around 100 nm) and that raises the n. Dispersion and absorption

are intimately related as dispersive media has to be absorptive. The equations that relate the absorption coefficient to the refractive index are called Kramers-Kronig relations, but more thorough presentation can be found elsewhere [22]. For us the fact that dielectrics have dispersion means that to effectively design an AR coating, we must find out the dispersion behavior of our materials. [20]

2.1.2 Polarization of Light and Reflectivity

Polarization can be stated to mean the oscillation path of the electric field amplitude $\mathcal{E}$ as the electromagnetic wave propagates in a medium. The most general polarization type of the monochromatic light is the elliptical polarization. Other types are circular polarization and linear polarization. [16] In fig. 2.5 there is the elliptical polarization chart on the left and on the right the rest three main polarization types as *b)* the circular polarization, that can be either right or left handed depending on the direction of rotation, *c)* as the parallel polarization or the transverse electric (TE) and *d)* as the perpendicular polarization or the transverse magnetic (TM). The last two are also known as p-polarization and s-polarization, respectively.

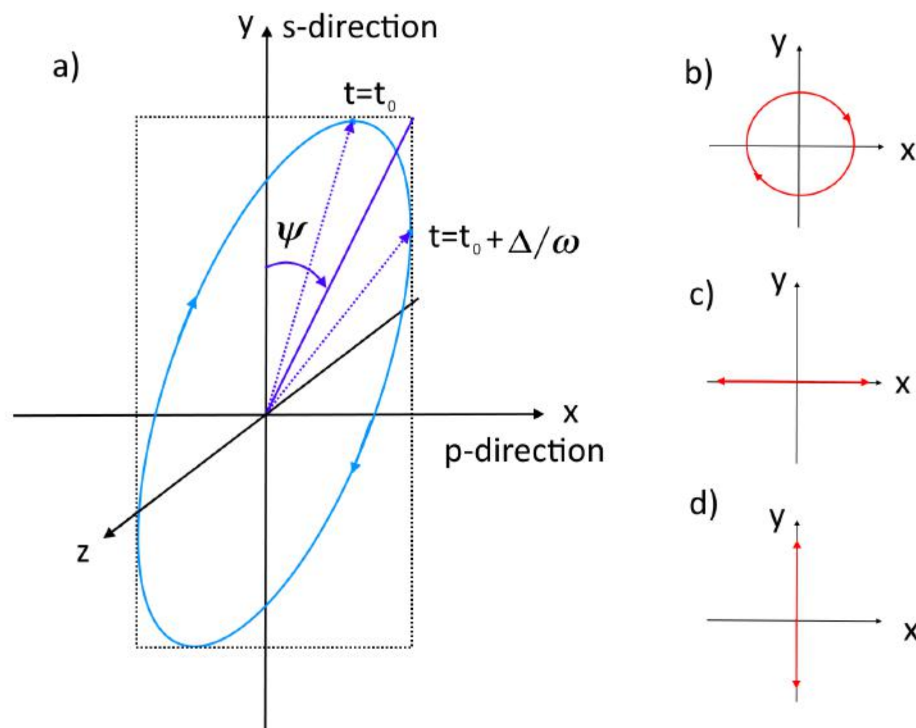

Figure 2.5 *Elliptical polarization, where the z-axis is the direction of propagation and three other main types of polarization.*

The parameters Δ and Ψ presented at the left in the fig. 2.5 are related to ellipsometric measurements, in which measured changes of the light's polarization

after reflection from the sample can yield many physical values, such as refractive index and film thickness. Ψ is the angle corresponding to the relative amplitude change and Δ corresponds to the phase difference between the field maximums of s- and p-polarization components. They are related to section 3.1.1, where is presented the ellipsometric measurement setup for the refractive index determination of our thin films.

To examine the reflections at a two media interface we need to divide the phenomenon to three different cases according to the incident angle and the polarization of the arriving light. First there is the incident wave coming along the surface normal and secondly there are two cases from oblique incidence angles that depend on the polarization. For consistent examination we need to set up convention that defines the positive direction of **E** always to be to the direction of x-axis. This way the direction of the magnetic field vector **H** is along the y-axis for incident and transmitted wave, but for the reflected wave it turns to the negative direction of y-axis, as its direction comes from the right-hand rule. This way we gain the boundary conditions for the field amplitudes

$$\mathcal{E}_{\mathbf{r}} + \mathcal{E}_{\mathbf{i}} = \mathcal{E}_{\mathbf{t}} \tag{2.21}$$

$$\mathcal{H}_{\mathbf{i}} - \mathcal{H}_{\mathbf{r}} = \mathcal{H}_{\mathbf{t}}. \tag{2.22}$$

Now because we have set the conventions and defined the boundary conditions, we can focus only on the field amplitudes $\mathcal{E}$ and $\mathcal{H}$. [1]

Let us begin with the normal incidence angle of a simple boundary of non-absorbing media. We are interested in the amounts of the reflected and the transmitted light, which are given by the ratio of the electric and magnetic field amplitudes of the incident light and either the reflected or transmitted light depending on which is under inspection. Using the equations 2.14, 2.15 and 2.22 we can write for reflection

$$\rho = \frac{\mathcal{E}_{\mathbf{r}}}{\mathcal{E}_{\mathbf{i}}} = \frac{y_0 - y_1}{y_0 + y_1} = \frac{n_0 - n_1}{n_0 + n_1}, \tag{2.23}$$

where ρ is the amplitude reflection coefficient. The suffixes 0 and 1 now correspond to the incident medium and the first film respectively. Similarly we can write for transmission

$$\tau = \frac{\mathcal{E}_{\mathbf{t}}}{\mathcal{E}_{\mathbf{i}}} = \frac{2y_0}{y_0 + y_1} = \frac{2n_0}{n_0 + n_1}, \tag{2.24}$$

where τ is the amplitude transmission coefficient. With the help of these coefficients one can describe the amount of reflected light R and the transmitted light T_{tr} as

$$R = \rho^2 = \left(\frac{y_0 - y_1}{y_0 + y_1}\right)^2 = \left(\frac{n_0 - n_1}{n_0 + n_1}\right)^2 \tag{2.25}$$

$$T_{tr} = \frac{y_1}{y_0}\tau^2 = \frac{4y_0y_1}{(y_0 + y_1)^2} = \frac{4n_0n_1}{(n_0 + n_1)^2}. \tag{2.26}$$

For the normal incidence angle it is therefore quite straightforward to calculate the reflectance and transmittance, once the optical constant n is known. [1]

For oblique angles the boundary conditions set before this examination quickly lead into complicated expressions for the vector amplitudes of the reflected and transmitted waves. Luckily for us there are two cases that reveal rather simple solutions, which are when the electrical amplitude is aligned with the plane of incidence (p-polarized light) and when the electrical amplitude is aligned normal to the plane of incidence (s-polarized light). Any incident wave with arbitrary polarization can be divided into two components according to these polarizations and which can be used to calculate the results of each polarization type for reflection and transmission, after which one can combine them to get the overall resultant. In order to deal only with vector amplitudes we must make some more conventions for the directions of the reference vectors that are used for phase difference calculations. The conventions used in Macleod's Optical Thin Film Filters [1] is presented in fig. 2.6 and we stick with them along this thesis.

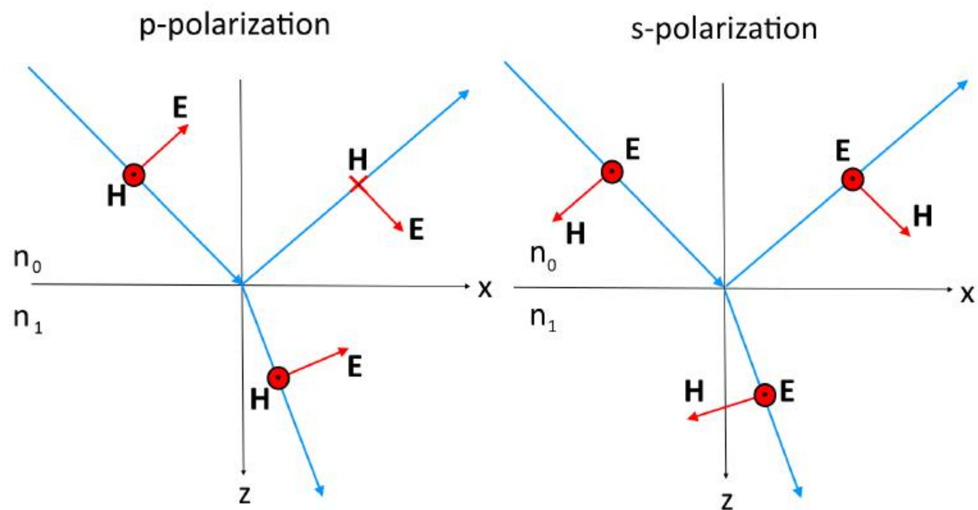

Figure 2.6 *An illustration of the field amplitude vectors at the film boundary in respect of their polarization type.*

For the polarized light facing thin film we use the components of $\mathbf{E}$ and $\mathbf{H}$ that are parallel to the surface boundary. This gives us the tangential components of amplitude coefficients ρ and τ, but they are not further distinguished from the regular amplitude coefficients. In other than thin film optics it is customary to use the components of irradiance in reflectance and transmittance, that are called Fresnel coefficients. The thin film coefficients *are not* Fresnel coefficients, although

only the transmission coefficient for p-polarization truly differs in value. [1]

Now using the tangential components of the field amplitudes and the set up conventions, we can write for p-polarization

$$\rho_p = \frac{\mathcal{E}_\mathbf{r} \cos\theta_0}{\mathcal{E}_\mathbf{i} \cos\theta_0} = \left(\frac{y_0/\cos\theta_0 - y_1/\cos\theta_1}{y_0/\cos\theta_0 + y_1/\cos\theta_1} \right) \tag{2.27}$$

$$\tau_p = \frac{\mathcal{E}_\mathbf{t} \cos\theta_1}{\mathcal{E}_\mathbf{i} \cos\theta_0} = \left(\frac{2y_0}{\cos\theta_0} \right) / \left(\frac{y_0}{\cos\theta_0} + \frac{y_1}{\cos\theta_1} \right) \tag{2.28}$$

$$R_p = \left[\frac{y_0/\cos\theta_0 - y_1/\cos\theta_1}{y_0/\cos\theta_0 + y_1/\cos\theta_1} \right]^2 \tag{2.29}$$

$$T_{tr-p} = \left(\frac{4y_0 y_1}{\cos\theta_0 \cos\theta_1} \right) / \left(\frac{y_0}{\cos\theta_0} + \frac{y_1}{\cos\theta_1} \right)^2, \tag{2.30}$$

where the values of θs are calculated in correspondence of the Snell's law 2.3. As this tangential convention was made to retain the rule $R + T = 1$, it is quite easy to give the equation some real values and check if this holds. In this case it does hold and we can continue to the s-polarization. With the similar approach than p-polarization we can now write the coefficients for the s-polarization as

$$\rho_s = \frac{\mathcal{E}_\mathbf{r}}{\mathcal{E}_\mathbf{i}} = (y_0 \cos\theta_0 - y_1 \cos\theta 1) / (y_0 \cos\theta_0 + y_1 \cos\theta 1) \tag{2.31}$$

$$\tau_s = \frac{\mathcal{E}_\mathbf{t}}{\mathcal{E}_\mathbf{i}} = (2y_0 \cos\theta_0) / (y_0 \cos\theta_0 + y_1 \cos\theta_1) \tag{2.32}$$

$$R_s = \left[\frac{\mathcal{E}_\mathbf{r}}{\mathcal{E}_\mathbf{i}} = (y_0 \cos\theta_0 - y_1 \cos\theta 1) / (y_0 \cos\theta_0 + y_1 \cos\theta 1) \right]^2 \tag{2.33}$$

$$T_{tr-s} = (4y_0 \cos\theta_0 y_1 \cos\theta_1) / (y_0 \cos\theta_0 + y_1 \cos\theta_1)^2 . \tag{2.34}$$

Similarly the s-polarization coefficients hold the rule $R + T = 1$. In all the equations 2.27–2.34 the y corresponds the optical admittance introduced in eq. 2.14. Now we'd like to shorten this expression of tilted admittance according to its polarization. As at the normal incidence the $\eta = y$, we can now write similarly for s- and p-polarization

$$\eta_p = \frac{y}{\cos\theta} = \frac{n\mathscr{Y}}{\cos\theta} \tag{2.35}$$

$$\eta_s = y \cos\theta = n\mathscr{Y} \cos\theta. \tag{2.36}$$

This enables us to write for all cases

$$\rho = \left(\frac{\eta_0 - \eta_1}{\eta_0 + \eta_1} \right) \qquad \tau = \left(\frac{2\eta_0}{\eta_0 + \eta_1} \right) \tag{2.37}$$

$$R = \left(\frac{\eta_0 - \eta_1}{\eta_0 + \eta_1}\right)^2 \qquad T_{tr} = \frac{4\eta_0\eta_1}{(\eta_0 + \eta_1)^2}, \tag{2.38}$$

which simplifies and unifies the presentation between the different cases as we continue to film design. These expressions 2.37 and 2.38 can be used to calculate reflectance and transmittance of a single boundary in various situations. One particularly interesting case arises with p-polarization as there is an angle after which all p-polarization is transmitted in the medium. This angle is called the Brewster angle and basically it polarizes the incoming light as only s-polarized light can reflect from it. With the optical admittance 2.35 and the Snell's law 2.3 the Brewster angle can be defined as

$$tan\theta_0 = n_1/n_0. \tag{2.39}$$

When trying to reach as low reflectance as possible over a wide range of wavelength it's important at least to recognize the existence of the Brewster's angle.

In fig. 2.7 I have presented the film system under consideration. There we have a plane wave arriving in the incident medium n_0 to a thin film, which have the physical thickness d and the refractive index n_1. Their boundary is the boundary a. Under the thin film lies the substrate which has the refractive index n_2 and its interface with the film is the boundary b. Both the incident medium and the substrate are supposedly infinite.

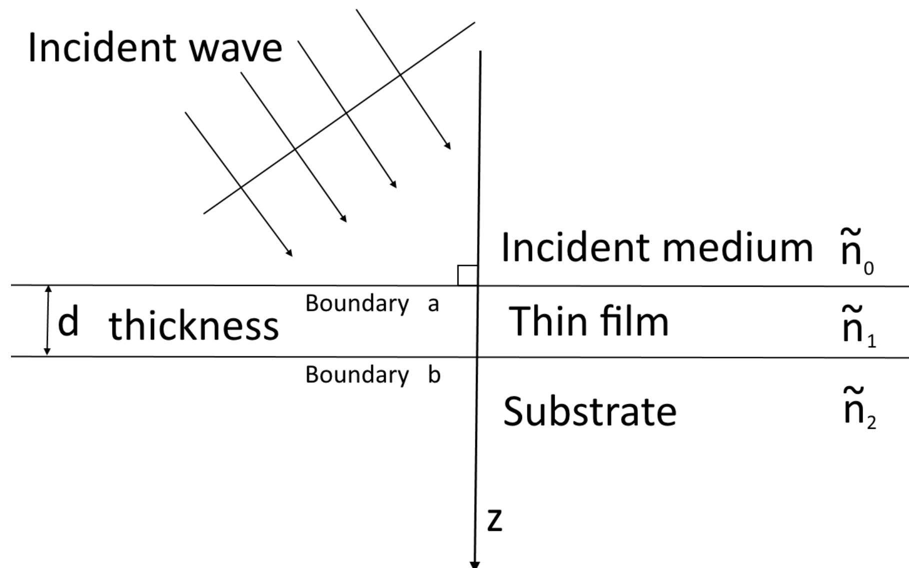

Figure 2.7 *A plane wave arriving to a film system, with two boundaries, defined film thickness d and known refractive indices n of the incident medium, thin film and the substrate.*

For consistent examination we set up the sign convention in which case the waves propagating in the direction of the incident wave are positive (+) and the waves

going to the opposite direction are negative $(-)$. The interfaces a and b can both be treated as a single boundary as was done before. Again we focus on the tangential components of $\mathcal{E}$ and $\mathcal{H}$ and mark them as $\mathscr{E}$ and $\mathscr{H}$ respectively. For the interface b there are no negative going waves in the substrate which leads into one positive going wave and one negative going wave reflected from the boundary. Then we can write for the tangential components

$$\mathscr{E}_b = \mathscr{E}_{1b}^{+} + \mathscr{E}_{1b}^{-} \tag{2.40}$$

$$\mathscr{H}_b = \eta_1 \mathscr{E}_{1b}^{+} - \eta_1 \mathscr{E}_{1b}^{-}, \tag{2.41}$$

where the common phase factors are neglected. From these we can further clarify the tangential components of the field amplitudes going into the positive and negative directions as

$$\mathscr{E}_{1b}^{+} = \frac{1}{2}\left(\mathscr{H}_b/\eta_1 + \mathscr{E}_b\right) \tag{2.42}$$

$$\mathscr{E}_{1b}^{-} = \frac{1}{2}\left(-\mathscr{H}_b/\eta_1 + \mathscr{E}_b\right) \tag{2.43}$$

$$\mathscr{H}_{1b}^{+} = \eta_1 \mathscr{E}_{1b}^{+} = \frac{1}{2}\left(\mathscr{H}_b + \eta_1 \mathscr{E}_b\right) \tag{2.44}$$

$$\mathscr{H}_{1b}^{-} = -\eta_1 \mathscr{E}_{1b}^{-} = \frac{1}{2}\left(\mathscr{H}_b - \eta_1 \mathscr{E}_b\right). \tag{2.45}$$

For the other interface a at a point with identical x and y coordinates, the field amplitudes can be determined by altering the phase factors of the waves. This can be done by multiplying the positive going wave with $\exp(i\delta)$ and the negative going wave with $\exp(-i\delta)$, where

$$\delta = \frac{2\pi \tilde{n}_1 d \cos\theta_1}{\lambda}. \tag{2.46}$$

With the phase changes we'll get for the a boundary a

$$\mathscr{E}_{1a}^{+} = \mathscr{E}_{1b}^{+} e^{i\delta} = \frac{1}{2}\left(\mathscr{H}_b/\eta_1 + \mathscr{E}_b\right) e^{i\delta} \tag{2.47}$$

$$\mathscr{E}_{1a}^{-} = \mathscr{E}_{1b}^{-} e^{-i\delta} = \frac{1}{2}\left(-\mathscr{H}_b/\eta_1 + \mathscr{E}_b\right) e^{-i\delta} \tag{2.48}$$

and similarly for the $\mathscr{H}_{1a}^{+}$ and $\mathscr{H}_{1a}^{-}$. By summing these positive and negative going field amplitudes one can write

$$\mathscr{E}_a = \mathscr{E}_b \cos\delta + \mathscr{H}_b \frac{i\sin\delta}{\eta_1} \tag{2.49}$$

$$\mathscr{H}_a = \mathscr{E}_b i\eta_1 \sin\delta + \mathscr{H}_b \cos\delta, \tag{2.50}$$

which now gives the field amplitudes for boundary a. Writing these two simultaneous

equations into matrix form one gets

$$\begin{bmatrix} \mathscr{E}_a \\ \mathscr{H}_a \end{bmatrix} = \begin{bmatrix} \cos\delta & (i\sin\delta)/\eta_1 \\ i\eta_1\sin\delta & \cos\delta \end{bmatrix} \begin{bmatrix} \mathscr{E}_b \\ \mathscr{H}_b \end{bmatrix}. \tag{2.51}$$

This matrix form now combines the incident tangential components of $\mathcal{E}$ and $\mathcal{H}$ to the components transmitted through the final interface. The 2×2 matrix in the eq. 2.51 is called the characteristics matrix of the thin film. Next we introduce the input optical admittance

$$\mathcal{Y} = \frac{\mathscr{H}_a}{\mathscr{E}_a} \tag{2.52}$$

which is the optical admittance entering the boundary a. This reduces the problem to finding of single boundary reflectance for the interface of incident medium with admittance η_0 and film system with admittance $\mathcal{Y}$

$$\rho = \frac{\eta_0 - \mathcal{Y}}{\eta_0 + \mathcal{Y}} \tag{2.53}$$

$$R = \left(\frac{\eta_0 - \mathcal{Y}}{\eta_0 + \mathcal{Y}}\right)\left(\frac{\eta_0 - \mathcal{Y}}{\eta_0 + \mathcal{Y}}\right)^*. \tag{2.54}$$

If we normalize the eq. 2.51, we get

$$\begin{bmatrix} \mathscr{E}_a/\mathscr{E}_b \\ \mathscr{H}_a/\mathscr{E}_b \end{bmatrix} = \begin{bmatrix} B \\ C \end{bmatrix} = \begin{bmatrix} \cos\delta & (i\sin\delta)/\eta_1 \\ i\eta_1\sin\delta & \cos\delta \end{bmatrix} \begin{bmatrix} 1 \\ \eta_2 \end{bmatrix}, \tag{2.55}$$

where B and C are the normalized electric and magnetic fields at the front interface and the $\begin{bmatrix} B \\ C \end{bmatrix}$ is known as the characteristics matrix of the assembly. With eq. 2.52 and 2.55 we can write

$$\mathcal{Y} = \frac{\mathscr{H}_a}{\mathscr{E}_a} = \frac{C}{B} = \frac{\eta_2\cos\delta + i\eta_1\sin\delta}{\cos\delta + i(\eta_2/\eta_1)\sin\delta} \tag{2.56}$$

which gives us an expression we can place in eq. 2.54 and calculate the system's reflectance. The way we calculated the front surface field values by starting from the nearest boundary of the substrate and calculating the positive and negative going tangential amplitudes for the boundaries b and then a does not restrict us from continuing to the next boundary if we have one. This means that in this method we can just add new layers and then calculate the admittance $\mathcal{Y}$ to get the overall reflectance. For more than just one film the characteristics matrix of the assembly can then be calculated as a product of individual characteristic thin film matrices

corresponding to to the layers as in eq. 2.55

$$\begin{bmatrix} B \\ C \end{bmatrix} = \left\{ \prod_{r=1}^{q} \begin{bmatrix} \cos\delta_r & (i\sin\delta_r)/\eta_r \\ i\eta_r\sin\delta_r & \cos\delta_r \end{bmatrix} \right\} \begin{bmatrix} 1 \\ \eta_m \end{bmatrix}, \tag{2.57}$$

where

$$\delta_r = \frac{2\pi\tilde{n}_r d_r \cos\theta_r}{\lambda}. \tag{2.58}$$

The suffixes r and m mean the corresponding layer number and the substrate respectively. With matrices it's utterly important to calculate the product in correct order as the matrix corresponding to the nearest boundary of the substrate has to be next to the normalized substrate matrix $\begin{bmatrix} 1 \\ \eta_m \end{bmatrix}$ and so on. This equation 2.57 is the basis of all thin film calculations and the prime tool for thin film design. With it and the eq. 2.54 even complicated thin film designs can be evaluated with the aid of computers and computational programs. [1]

Now we have the overall background theory governing the phenomena concerning light and matter regarding optical thin films. Next I'll introduce more precisely the anti-reflective coatings and the design used in this thesis.

2.2 Anti-reflective Coatings

As discussed before when light arrives to an interface or propagates through different mediums there are several important phenomena taking place. These are reflection, transmission, refraction, absorption, luminescence and scattering [23]. A simple illustration of the two most important for an AR coating, the reflection and absorption, is presented in fig. 2.8.

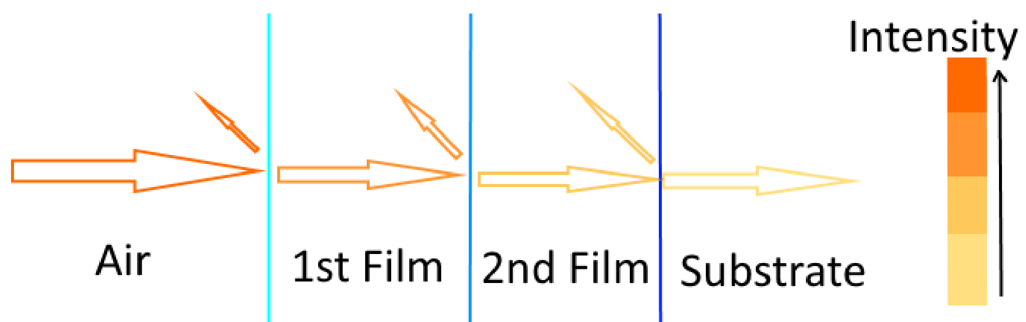

Figure 2.8 *Light facing different mediums is partially reflected and absorbed as it propagates through them.*

A proper AR coating for solar cells should decrease the amount of reflected light ideally to zero and yet be non-absorbing in the spectrum of the sun. In reality we

are optimizing the reflectivity and transmittivity of the coating by exploiting the characteristics of the used materials and defining the optimal structure for the layers of the coating. In addition to these optical properties the AR coating must also be mechanically and chemically endurable as it most often is the outermost layer in many structures. In the next section I present an overview of optical thin films in general and after that I will go through a theory of designing an AR coating.

2.2.1 Background of Optical Thin Films

The history of optical thin films can be seen started with manufacturing the predecessor of AR coatings. First anti-reflective surfaces were done by etching glass. The method based on roughening the surface to get a layer with an intermediate n between the intact glass and air. Since then the variety and numbers of different optical thin films have grown significantly and one of the most widely used thin film filter in addition to AR coatings is the Fabry-Perot interferometer, that is a multiple-beam interferometer and is mainly used for fine structure examination of spectral lines. [27] Other types of thin film filters include HR mirrors, beam splitters, edge filters and band-pass filters. [1] The applications for AR coatings alone are numerous and include such targets as surface emitting lasers [28], optical data storages [29], camera lenses [30], eye-glasses [31] and flat panel displays [32]. Thus it is only reasonable to state that optical thin films and specifically AR coatings are a very important field of technology and material science.

To find optimal solutions for different kind of thin film systems one have to find materials with proper qualities to fulfill the task in hand. For example to reduce reflection between air (n_{air}=1.003) and glass ($n_{glass} \approx 1.5$) with a single film, one should find material with refractive index close to $n = \sqrt{n_{air}n_{glass}} \approx 1.225$ [1]. This requires a good background check for the available materials and for this case no conventional dielectric material exists to completely fulfill the condition for refractive index. However, material research continues to find new methods to manipulate refractive index due porosity [33–37] and other structural parameters [38–40] and also the coating SC510K tested in this thesis reaches an index as low as 1.25 at some wavelength range. For dielectric thin film materials it is essential that they have very low absorption ($\alpha < 10^3 cm^{-1}$), good transparency at the wanted wavelength range and suitable refractive indices for the task at hand. [2] The table 2.1 lists some common dielectric materials and their thin film properties.

Table 2.1 *Few selected thin film materials and their characteristics.*

Material	Deposition technique	Refractive index	Region of transparency [μm]	References
Al_2O_3	E-Beam	1.54–1.63 at 550 nm (T_s=40–300 °C)	0.2– 7	[2]
ZnS	E-Beam	2.6 at 550 nm 2.2 at 10 μm	0.4 – >14	[41]
MgF_2	Thermal evaporation, E-Beam	1.32–1.40 at 550 nm depends on T_s and whether it's measured in air/vacuum	0.23– 10	[41] [2]
SiO_2	Thermal evaporation, E-Beam	1.44 at 546 nm	0.2– 9	[41] [2]
CaF_2	E-Beam, Thermal evaporation	1.23–1.46 at 550 nm relates to packing density 1.32 at 10 μm	0.15 – 12	[42], [41] [2]
ZrO_2	E-Beam	2.192 at 600 nm 2.05 at 10 μm	0.6 – >10	[42]
Ta_2O_5	E-Beam	2.25 at 550 nm 1.95 at 10 μm	0.35 – 10	[42] [2]
TiO_2	Thermal evaporation, E-Beam	1.9–2.55 at 550 nm depending on T_s	0.4–3	[41] [2]
Si	Thermal evaporation, E-Beam	3.5 at 546 nm	1–9	[41] [2]
Ge	Thermal evaporation, E-Beam	4.4 at 2 μm	2–23	[2]

Usually thin films have different optical properties than bulk materials. Their transparency is slightly worse because of absorption caused by small stoichiometric deviations and contaminations and because of scattering caused by imperfections in surface and volume structures. In short the thin films are more prone to structural errors. Also the refractive indices differ between bulk and thin film materials. The thinner the film the lower the refractive index and as the thickness grows it approaches the bulk value. For thin films the refractive index depends on the deposition method, as its structure is affected by process parameters, developing microstructures and chemical composition. The growth temperature T_s has the greatest impact as often the films are partly amorphous at room temperature (RT) deposition and start to crystallize as the T_s grows. Also the packing density increases as the T_s rises. *Ex-situ* annealing has similar effects as the growth temperature. Addition to the

optical properties the physical attributes as adhesion, stress and chemical endurance differ between the bulk and the thin film. Thin films require good adhesion to the substrate surface and must not be too stressed. Stresses arise from incompleteness of structural ordering and differences of expansion coefficients between layers and the substrate. The stress can be either tensile or compressive as shown in fig. 2.9. Balancing layers with opposite type of stress makes the structure more durable. [2]

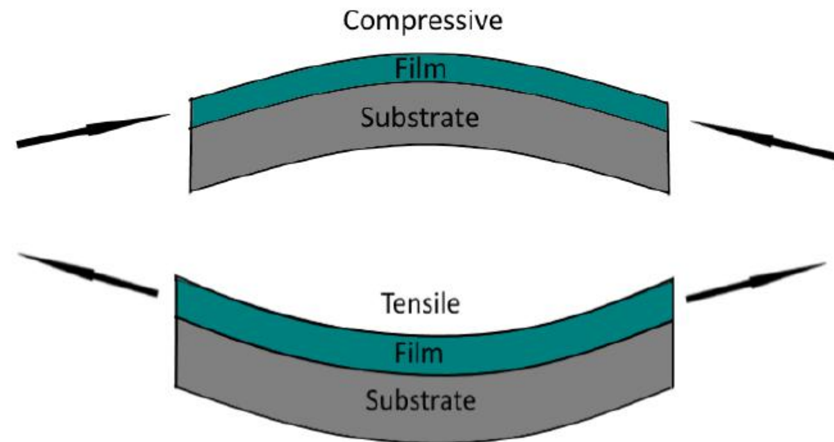

Figure 2.9 *The stress types between a thin film and a substrate.*

If there's too much stress in the layer structure, the film most likely cracks which lowers adhesion and in the worst case the coating peels off. The films should also be resistant to water vapor sorption and be non-soluble to water and acids formed in atmosphere from water and gases such as SO_2 and H_2S. [2]

As explained in section 2.1.1 most dielectrics have some extent of dispersion that affects their optical behavior. To design an AR coating it is crucial to know the refractive index profiles of the used materials. For example here are presented the dispersion curves of the currently available dielectrics at ORC in fig. 2.10. The curves are from literature as TiO_2 [43], Ta_2O_5 [44], SiN [45], Al_2O_3 [46], SiO_2 [47] and MgF_2 [48]. In reality these curves are also dependent on the deposition methods and parameters. This is why, for accurate design, one should define the dispersion profiles of the materials that are similarly deposited as the supposed design components.

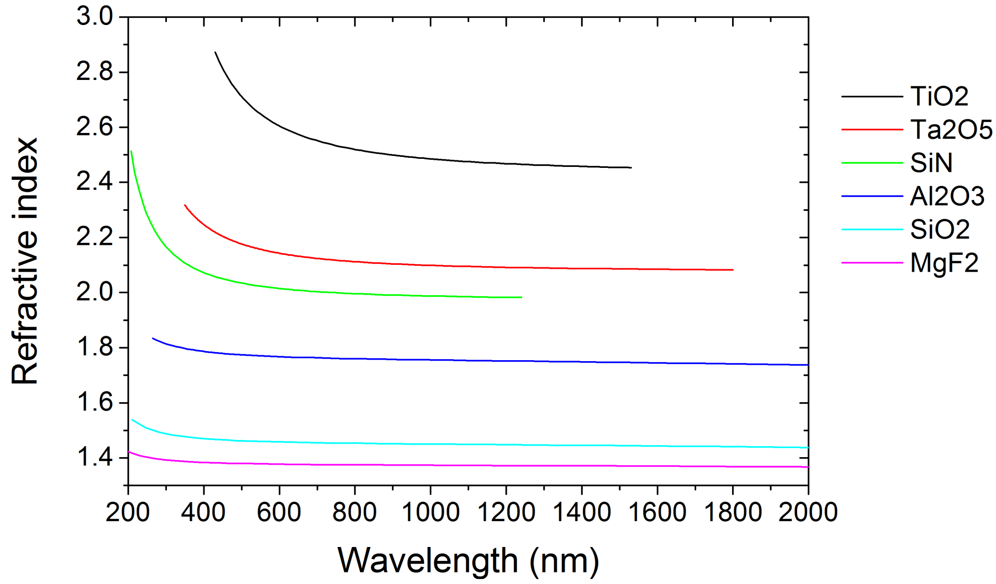

Figure 2.10 *The refractive index profiles of some commonly used dielectrics [43–48].*

Next I have gathered a short overview of some of the most commonly used dielectrics for thin films and focused on those that are used in this thesis, which are MgF_2, TiO_2, Al_2O_3 and SiO_2. With the latter I focus on thin films fabricated with plasma-enhanced chemical vapor deposition (PECVD) and with the rest by electron-beam evaporation (EBE) deposited films. In addition I'll shortly present the commercial SC510K and SC800i spinnable siloxanes. A thin film's visible color depends on its substrate, it is deposited on, and on its thickness as different optical thicknesses produce different interference causing the color changes. An example of this is presented in fig. 2.11, where some samples of this study are shown and as comparison one of the AR coatings on a solar cell without front-contacts.

Magnesium fluoride MgF_2 is a widely used thin film material due to its low refractive index and good mechanical durability. [49–51] Its deposition methods range from electron beam evaporation [49, 50, 52], thermal evaporation [53–55] and ion-beam assisted deposition (IAD) [52, 56, 57] to special sputtering methods [58, 59], as in regular sputtering it tends to lose fluorine, which raises the refractive index n and absorption α [60, 61]. Even atomic layer deposition (ALD) has proven to be an option [62]. MgF_2 is partially amorphous at room temperature (RT) and crystallizes as the deposition temperature T_s rises. [63–65] Its main downside is the columnar microstructure, which creates voids that can be filled with moisture in atmospheric conditions. Addition of water vapor affects the optical behavior of the film, but has also been shown to lower the stress of the film structure. [50, 55, 66] The phenomenon is linked to the material's packing density and several studies have proven that higher deposition temperature leads to denser structure. [50, 66, 67] In room

temperature deposited MgF_2 the packing density is about 0.72, but when deposition temperature is raised over 250 °C the density reaches 1. Negatively this also increases stress and roughens the surface. [50, 51, 63, 68] In this thesis I will study EBE deposited MgF_2 for anti-reflective coatings and for thin films in general. Focus is on AR coating design for MJSC, where MgF_2 would form the low index layer.

Titanium oxide TiO_2 is one of the most studied dielectrics, due to its many applicative properties, such as being a photocatalyte and a high index material in dielectric thin film filters. [1,69] There are even few books solely handling properties and usage of TiO_2. [69, 70] It has many deposition methods such as EBE [71–74], PECVD [75], reactive evaporation [76] and sputtering [77, 78]. Its refractive index vary from 2.06 to 2.4 [71], it has good abrasion resistance [71] and it is amorphous when deposited under temperature of 250 °C [76]. With EBE it can be produced from TiO, Ti_2O_3, Ti_3O_5, TiO_2 and Ti and these all require additional oxygen, as TiO_2's refractive index and transparency are highly sensitive to the oxygen count. [71] In this thesis TiO_2 is used as a high index material for all the AR coatings that are being fabricated. As a starting substance we use TiO_2 for the EBE, which unfortunately produces the lowest refractive index TiO_2 films from all the mentioned starting substances. [71] With increasing deposition temperature also the refractive index rises, but the better starting substance for EBE would be either Ti_2O_3 or Ti_3O_5 as they produce better quality TiO_2 films. [71]

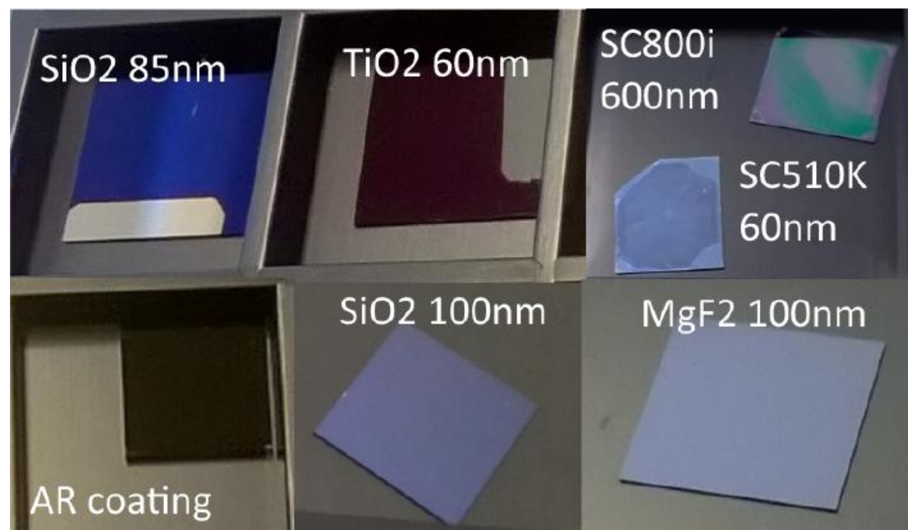

Figure 2.11 *Thin films fabricated for this thesis. The thicknesses are suggestive to give a clue how thickness affects to the color of a thin film. This difference can be clearly seen with the two SiO_2 films.*

Aluminum oxide Al_2O_3 has refractive index values from 1.55 to 1.72 depending on the deposition conditions. [79] This makes it more or less intermediate index material, that would be suitable for step-graded AR coating, as a layer between

high and low index materials. Its deposition methods include EBE [80], CVD [81], spray pyrolysis [82] and IAD [83]. Addition to being profiled as a medium index material, Al_2O_3 has high chemical stability and high radiation resistance [82] and it's transparent down to 250 nm [80]. These properties make Al_2O_3 an excellent material for AR coating's medium index layer, especially when space environment is taken into consideration, as in space the coating structure is exposed to greater amount of radiation than in terrestrial applications. In this thesis Al_2O_3 is used as an intermediate layer between MgF_2 and TiO_2 and all three are deposited with EBE.

PECVD deposited silicon dioxide SiO_2 is widely used in micro-electronics as a passivation oxide and it's applicable in industrial scale. [17] This method for SiO_2 deposition has long been known and it's usual to have SiN as another PECVD dielectric, which can act as a high index material in contrast for the low index of SiO_2. [84,85] Other popular option is to combine SiO_2 with TiO_2, which also can be deposited with PECVD. [75] Good film quality of PECVD deposited SiO_2 requires a low deposition rate [86], which is a downside compared to physical vapor deposition methods. As SiO_2 has many other deposition methods, such as sol-gel deposition [37], electron beam evaporation [87] and ion-beam sputtering [87], the PECVD is not necessarily the most convenient choice. With other deposition methods the refractive index of SiO_2 has succesfully been lowered via porosity [33, 36, 37, 85, 88] or other parameters [39]. As there is not widely known porosity tests done with PECVD for SiO_2, this thesis tries to find optimal parameters to enhance porosity and apply the low index SiO_2 to an AR coating.

The commercial siloxane solutions SC510K [89] and SC800i [90] for spin-coating are products of the Pibond corporation [91]. The basic unit of a siloxane polymer is shown in fig. 2.12.

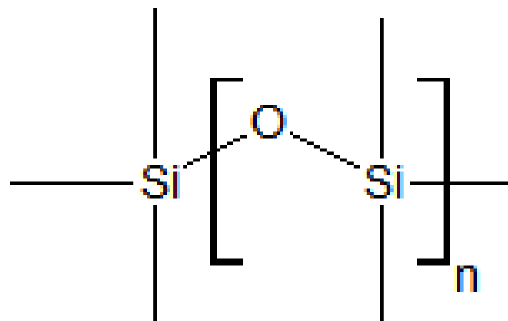

Figure 2.12 *The siloxane is a polymer constructed from silicon, oxygen and hydrocarbon chains. In the picture is presented the basic unit of a siloxane, illustrated with ChemSketch [92].*

Here is a short presentation of relevant information from the manufacturer's pro-

cess guides to give a suitable background for their characterizations. The SC510K is designed as an anti-reflective coating on its own for microlenses and other optics. It's promised to have very low refractive index (1.25) and full transparency in visible spectrum of light. It has good adhesion properties and it remains stable up to 850 °C. The siloxane is deposited with spin-coating and cured with heating the coating at 200 °C for five minutes. The SC800i has similar properties than SC510K, but the main difference is additional TiO_2 nanoparticles that are used to raise the refractive index. The refractive index of the SC800i is promised to be 1.84 and as the SC510K the coating is transparent at the visible range of light. Otherwise the coating processes of the siloxanes are pretty similar. Both coatings were characterized and deposited on silicon test wafers and the SC510K was used as an lower index material in AR coating.

2.2.2 Designing an Anti-reflective Coating

There are several different techniques to design AR coatings with multilayer structures such as vector method, matching optical admittance [1] or optimizing it numerically [93] and graphical methods such as Smith's chart and Kard's calculator [41], but here we focus on the matrix method and lean on the notations used by H. A. Macleod [1]. In the actual optimization for the AR coatings of this thesis I used the design software Essential Macleod developed by him and his group, which is briefly described in the section 3.1.4.

Optical thin film theory leans heavily on the Maxwell's macroscopic theory of electromagnetic waves (eq. 2.9–2.12) applied to propagating light in layered structures. For theoretical approach we make few assumptions:

1. Thin film is an optically isotropic medium, that is defined by its refractive index n.
2. At the interface of two different media the n changes instantly when the boundary is crossed.
3. Layers are considered to be parallel planes, that have infinite lateral dimensions and which are determined by perpendicular thickness d.
4. Incident wave is plane, monochromatic and linearly polarized in either p or s direction.

In this theoretical examination scattering, absorption and effects of film inhomogeneous are neglected. [27] In addition we consider optical film to be thin when it produces full interference effects in the reflected or transmitted light. This kind of film is called coherent. The opposite kind of films that do not have interference

effects or they are incomplete are called incoherent and they are considered to be thick films. In the AR design case we usually consider all the layers on the substrate to be thin and the substrate to behave as thick film. [1] With these assumptions in mind and the theoretical background presented in section 2.1, we can now proceed to principles of AR design.

The simplified ground rule for AR design is to have as small refractive index difference between adjacent layers as possible. The more you have layers the better you can choose materials next to each others that have little difference in their refractive indices. A very powerful AR structure is continuously varying refractive index material, that would grade the index difference between incident medium and the substrate. This kind of structure is called graded index (GRIN) material and such layers have been used as an AR coating. [39,94] An illustration of different AR designs and their refractive indices is pictured in fig. 2.13.

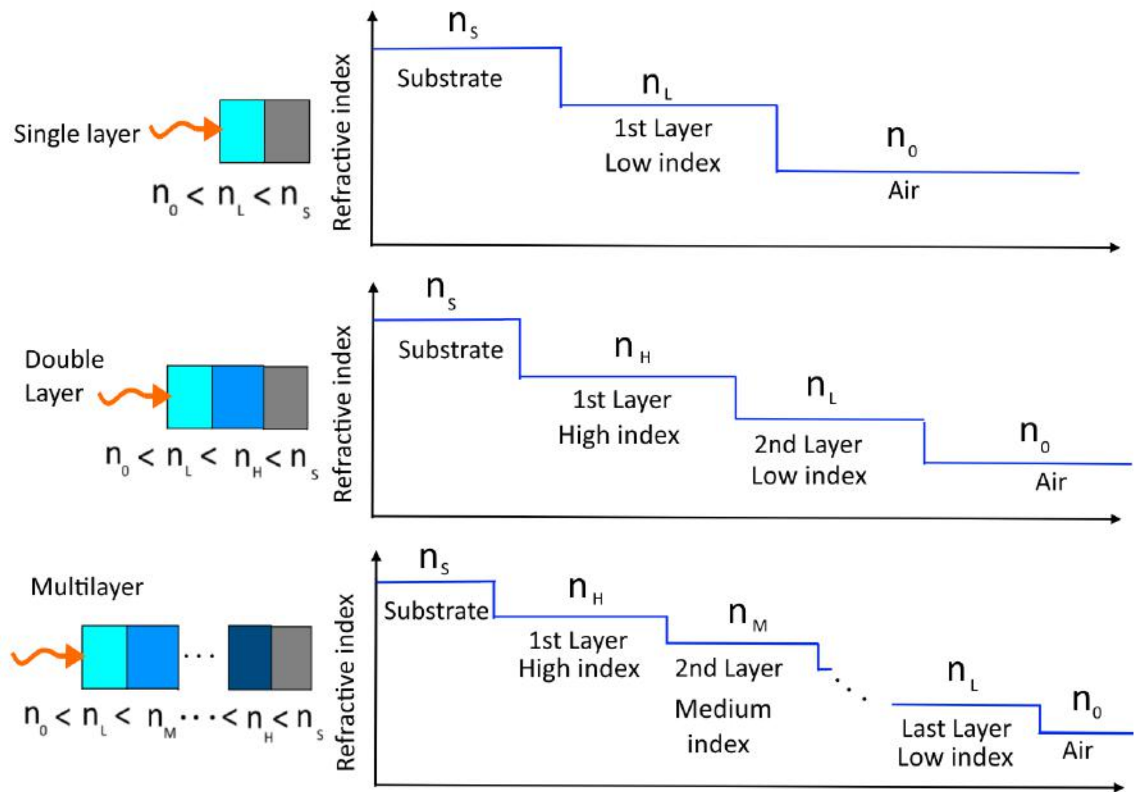

Figure 2.13 *The refractive index requirements for different AR coating designs.*

In addition to refractive indices also layer thickness affects, as the thickness defines the phase change of the propagating light and thus has a great impact on the interference that should preferably cancel itself at the top surface. It all comes down to modeling and calculating the optimal design with the help of section's 2.1.2 theory. Next I'll present some calculations behind the AR coating designs of this

thesis.

Designing AR coating is not straightforward as the most AR coating designs are made with trial and error assisted with approximate techniques and powerful computational tools. Many good designs can be further improved with computer refinement and a reasonable starting design is a good start for finding the optimum one. In the calculations the matrix method presented in section 2.1.2 is the main way of computational evaluation. The most common AR design is a single layer coating. A good start is to take a quarter-wave optical thickness layer and fix the wanted wavelength center. The admittance of such layer is

$$\mathcal{Y} = y_1^2/y_m, \tag{2.59}$$

which gives us the reflectance according to the eq. 2.54

$$R = \left(\frac{y_0 - \mathcal{Y}}{y_0 + \mathcal{Y}}\right)^2 = \left(\frac{y_0 - y_1^2/y_m}{y_0 + y_1^2/y_m}\right)^2. \tag{2.60}$$

This however was just for the normal incidence angle and in our case that's not sufficient. Therefore we use the tilted admittances 2.35, 2.36 and the characteristics assembly matrix 2.57 to yield the reflectance of a single layer AR coating

$$R = \frac{(\eta_0 - \eta_m)^2 \cos^2\delta_1 + [(\eta_0\eta_m/\eta_1) - \eta_1]^2 \sin^2\delta_1}{(\eta_0 - \eta_m)^2 \cos^2\delta_1 + [(\eta_0\eta_m/\eta_1) + \eta_1]^2 \sin^2\delta_1}. \tag{2.61}$$

For single layer coating the expression for R is still quite reasonable to calculate even with paper and pencil, but when more layers are added the formula quickly becomes tedious. The great side of a single layer coating is its simplicity, but it can reduce the reflectance to zero only at one wavelength, if the circumstances are optimal, and its reflectance minimum is not broad enough for MJSC AR coating applications. [1]

Next step to improve the design is to add a layer. The double layer AR coating has more variables to it and it can have either one minimum (V-shape) or double minimum with local maximum (W-shape). To reach the zero reflectance the optical admittance $\mathcal{Y}$ has to equal y_0. Solving this equality from the assembly characteristics matrix 2.57 leads us to conditions

$$\tan^2\delta_1 = \frac{(y_m - y_0)(y_2^2 - y_0 y_m) y_1^2}{(y_1^2 y_m - y_0 y_2^2)(y_0 y_m - y_1^2)} \tag{2.62}$$

$$\tan^2\delta_2 = \frac{(y_m - y_0)(y_0 y_m - y_1^2) y_2^2}{(y_1^2 y_m - y_0 y_2^2)(y_2^2 - y_0 y_m)}, \tag{2.63}$$

where the results as δ_1 and δ_2 has to be real. This means that the right hand side

of the equations 2.62 and 2.63 have to be positive. This leaves us with terms

$$\left(y_2^2 - y_0 y_m\right) \tag{2.64}$$

$$\left(y_1^2 y_m - y_0 y_2^2\right) \tag{2.65}$$

$$\left(y_0 y_m - y_1^2\right), \tag{2.66}$$

where all three have to be positive or two negatives and one positive. An effective coating can be reached by using two quarter-wave layers, which yields a reflectance

$$R = \left(\frac{y_0 - \left(y_1^2/y_2^2\right) y_m}{y_0 + \left(y_1^2/y_2^2\right) y_m}\right)^2 = \left(\frac{1 - \left(y_m/y_0\right)^{\frac{1}{3}}}{1 + \left(y_m/y_0\right)^{\frac{1}{3}}}\right)^2. \tag{2.67}$$

The result is rather simple, but the extensive equation handling to gain this formula can be found in Optical Thin Film Filters by H.A. Macleod [1]. The more layers are added the more complicated the calculations and derivation of boundary conditions become. A thumb rule, where to begin with, is to find suitable materials with high and low refractive indices and start the refining process near the optical quarter-wave thicknesses. Therefore in the design process of the AR coatings manufactured and studied in this thesis, the layers are refined with Essential Macleod design program, with reasonable starting designs to begin with. And, as mentioned before, the best AR coating designs are found through trial and error.

2.3 Multi-junction Solar Cells

Although the photovoltaic effect had been long known [95–99], it was not until 1954 that solar cells (SC) started to receive more interest, when Chapin *et. al* fabricated and studied single-crystal silicon cells [100] and Reynolds' team cadmium sulfide cells [101]. When the best efficiency thus far had closed only 1 % the Chapin's cells reached conversion efficiency of 6 %. Since then the progress has been huge and the SCs are under intensive research even nowadays. The universal goal for all SC research is to find more efficient and cheaper solutions for PV power production. [102]

The basic principle of solar cells is to convert sunlight to electricity. The range of different solar cell applications vary from bacteria powered solar panel [103] to combining quantum dots and organic molecules [104]. Common for these all is the goal to harvest as much energy from the sunlight as possible. In the fig. 2.14 there is presented three curves that portray the sun's irradiance in different situations. The black curve presents the extraterrestrial solar irradiance, the blue is the direct normal spectral irradiance and the red one shows the global total spectral irradiance on the 37 degrees tilted sun facing surface in atmospheric conditions. The sun's

radiation intensity at the average distance of the earth in free space is circa 1353 W/m ^{2} and it varies depending on the current location on the elliptical orbit around the sun. As the light propagates in atmosphere its intensity is reduced due to water-vapor absorption (IR), ozone absorption (UV) and scattering caused by aerosols and dust particles. [102] On average the irradiance from the sun is approximated to be roughly 1000 W/m ^{2} [10]. The amount of the sun's irradiance is quantified with air mass (AM) and a number corresponding to the atmospheric path lenght that light has to travel before reaching the surface. AM0 corresponds to the extraterrestrial circumstances and AM1.5 to an energy-weighted average for terrestrial conditions. [102] The standard test conditions for solar cells are cell temperature of 25 °C, the solar irradiance spectrum of AM1.5 and total irradiance set to 1000 W/m ^{2}. Its deviation from the real conditions, however, has lead to the usage of a modified spectrum of AM1.5 [105]. The difference is marked as AM1.5D for the conventional standard and AM1.5G for the new one. Both standards appear in literature, which requires precision from reader, if any reliable comparison is to be done. [11]

The proportion of the radiative energy that a solar cell can convert to electric power is related to the materials used in the solar cell. For example a planar conventional silicon solar cell can convert only about 10 to 20 % of the whole irradiance to electric energy [10, 106, 107]. The most influential parameter is the material band gap E_g that basically defines which photons have the right amount of energy to be absorbed. If the photon's energy is too low it cannot excite any electrons and the light just passes the structure and if the energy is too high the photons excite the electrons to higher energy levels and due to relaxation processes most of the energy is wasted as thermal heat. [12]

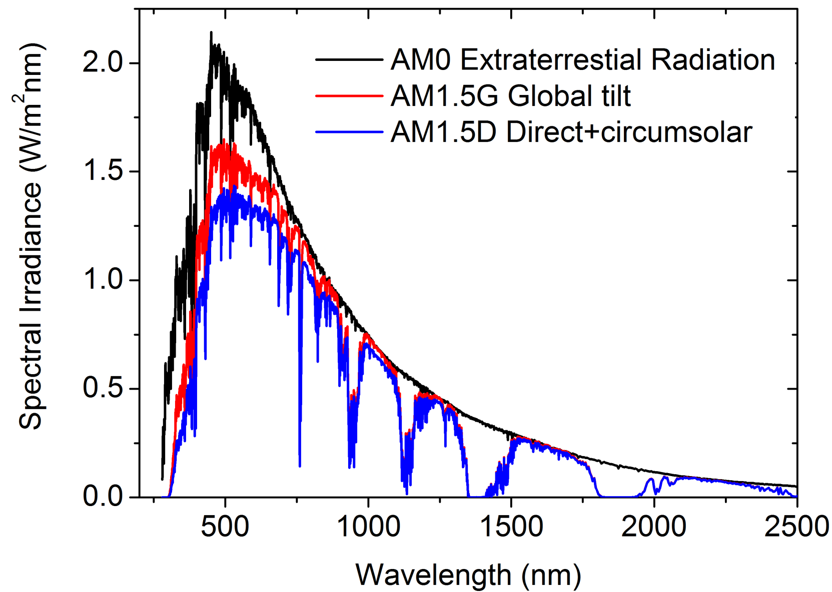

Figure 2.14 *The ASTM G173-03 reference spectra for the solar spectral irradiance. The data for the plot was acquired from [108].*

Multijunction solar cells are devices that combine solar cells that are optimized for different bandwidth range of solar spectrum, so that when joined together they can exploit greater proportion of the incoming light than a single-junction cell. [12] Under one sun illumination the best MJSCs can reach even 37.9 % efficiency and when encapsulated within a concentrator unit that focuses larger amount of sunlight to the cell, even 46 % efficiency has been reached. [10] So when compared to the conventional silicon solar cells, we are talking a considerable improvement. The target for MJSCs lies in concentrated photovoltaics (CPV) and space applications, due to their high efficiency and relatively small required surface area per cell. [11,12] As regular solar cells, also the MJSCs require AR coatings to reduce the amount of reflected light to increase the total efficiency. The next sections describe some relative theory behind solar cells and MJSCs and consider the requirements for MJSC AR coatings.

2.3.1 Principle of Operation and General Structure

Semiconductor solar cells are included in the class of photodetectors. Their principle of operation is mainly based on three processes:

1. Carrier generation by incident light.
2. Carrier transport and/or multiplication by current-gain mechanism if present.

3. Extraction of carriers as terminal current to provide an output signal.

Other types of photodetectors are for example photodiodes, photoconductors and phototransistors. [102] All these devises are based on the photoelectric effect that is caused by the incoming photon. The energy transition ΔE from the photon to the device is therefore related to the photon's energy and it can be stated to be dependent on the photon's wavelength λ:

$$\Delta E = h\nu = \frac{hc}{\lambda}, \tag{2.68}$$

where h is Planck's constant, ν the photon's frequency, λ wavelength of the incoming photon and c the speed of light. The energy of the photons transmits to the electrons of the semiconductor and induce a current that is specifically called photocurrent I_{ph}. For every photodetector it is important to maximize the photocurrent to optimize their performance. The physical magnitude that corresponds to this is the external quantum efficiency $EQE(\lambda)$ which basically means the number of charge carriers produced per photons of a certain wavelength λ, as

$$EQE(\lambda) = \frac{I_{ph}(\lambda)}{q\Theta} = \frac{I_{ph}}{q}\Big(\frac{h\nu}{P_{opt}(\lambda)}\Big). \tag{2.69}$$

The q is charge of an electron, the Θ is the photon flux as $\frac{P_{opt}(\lambda)}{h\nu}$ and $P_{opt}(\lambda)$ is the optical power. In an ideal case, where every arriving photon creates an electron-hole pair, the quantum efficiency is equal to one. This is reduced due the fact that not every photon has a proper amount of energy for charge carrier creation and due losses in cell caused by carrier recombination, incomplete absorption, reflection and so on. [102] In addition to EQE a solar cell's quantum efficiency can be described by the photons that really reach the cell structure, so photons that are reflected do not count. This version of quantum efficiency is called the internal quantum efficiency IQE and the main difference to EQE is the treatment of the reflected photons. When the internal quantum efficiency is known, we can derive the total photocurrent as

$$I_{ph} = \int_{\lambda} \Theta(\lambda)\left\{1 - R(\lambda)\right\} IQE(\lambda) d\lambda, \tag{2.70}$$

where we integrate over the wavelength range of the incoming light and $R(\lambda)$ denotes the reflectance of the top surface. Both IQE and EQE are used to evaluate the solar cell's performance. [12]

To understand the working principle of a solar cell, it's essential to know some physics of the semiconductors. A semiconductor is a material, that excites electrons from valence band to conduction band, when it's exposed to heat. This thermal excitation creates an electron-hole pair, where both are free carriers and can move

randomly within the lattice structure. In intrinsic (undoped) material the number of free electrons and holes is equal and quite low. The small carrier concentration leads to low conductivity and so a regular semiconductor in room temperature is not a very good conductor. By adding atoms with a different number of valence electrons here and there in the lattice structure, one can increase the number of free charge carriers. This technique is called doping and its main purpose is to increase the conductivity of the semiconductor. When the added atoms have an extra electron compared to the host semiconductor atoms the doping type is referred as n-type doping. Similarly when there is a one electron less in the valence band, the doping type is p and effectively this means one hole more in the structure. As the dopant materials still have both electrons and holes, but now the number is heavily leaned to the dopant type, the carriers are singled out as majority carriers, the type of doping, and as minority carriers, the opposite type to the doping. In heavily doped materials the ratio of majority carriers to minority carriers can be billions to one. Thus majority carriers suppress the number of minority carriers and as the name suggest the conductivity is due to the majority carriers. In solar cells the photo-generated majority carriers do not significantly alter the majority carrier concentration, but the scarce number of minority carriers is heavily increased. [102] The most simple solar cell type is a single-junction pn solar cell, where differently doped layers of the same semiconductor material are combined. The theory presented here focuses on pn-type solar cell, as the principles are very similar to the other SC types that include p-i-n cells, amorphous cells and compound semiconductor cells. [12]

In fig. 2.15 is presented a single-junction GaAs pn solar cell and the process where the incoming photon excites an electron from valence band to conduction band and thus creates an electron-hole pair. The electron is then driven to the negative terminal and the hole to the positive terminal of the cell by the structure of the device and this causes electrical power. [12]

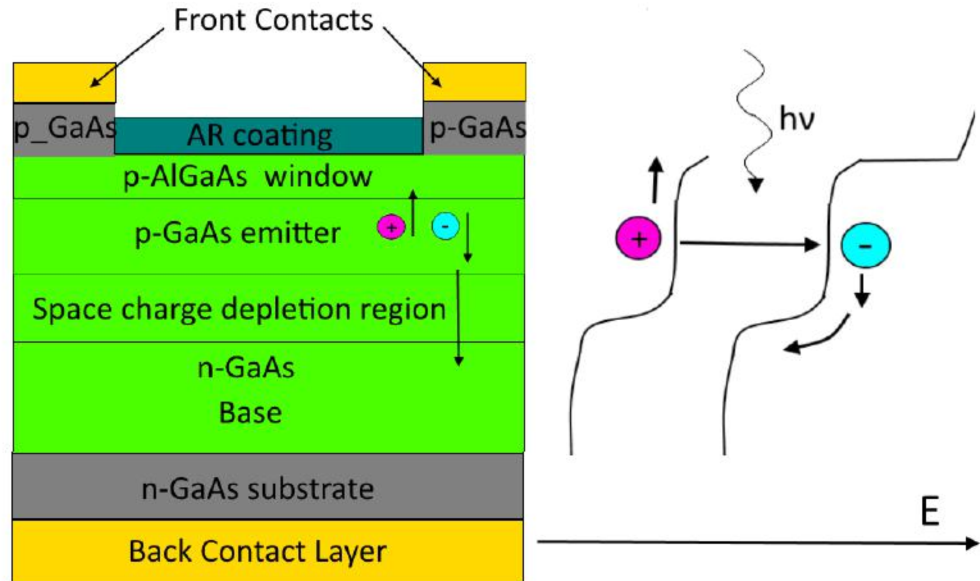

Figure 2.15 *An example of A simple single-junction GaAs pn solar cell and the excitation principle. The figure is adapted from [12].*

An ideal solar cell is in principle a current source parallel connected to a rectifying diode. Its current-voltage (I-V) characteristics can be presented with Shockley's solar cell equation

$$I = I_{ph} - I_0 \left(e^{\frac{qV}{k_B T}} - 1 \right), \tag{2.71}$$

where I_0 is the saturation current, k_B is the Boltzmann's constant, V is voltage of the cell and T is the absolute temperature in kelvins. In practice, without illumination, a solar cell is just a semiconductor current rectifier, or a diode. The similarity can be seen in fig. 2.16, where both diode's and solar cell's I-V characteristics are illustrated. If the SC is ideal the diode's I-V curve represents the solar cell's I-V behavior in dark. In practice, when solar cell's I-V characteristics are under inspection, the current axis is turned over to ease the interpretation. This causes change of signs for the current terms in eq. 2.71, that must be taken into account in calculations. [12]

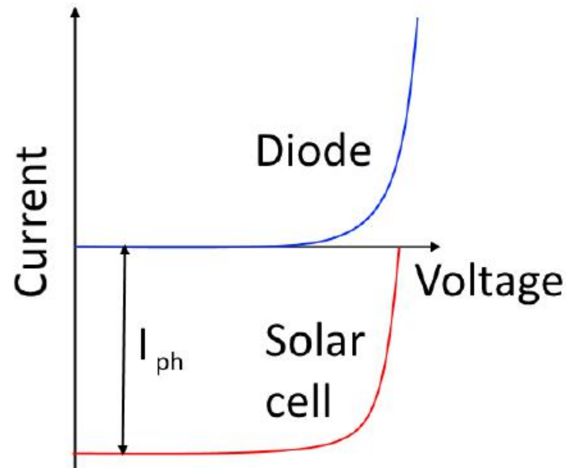

Figure 2.16 *I-V characteristics of a diode and a solar cell. The figure is a re-illustration from source [12].*

For an ideal cell the short-circuit current I_{sc} is equal to the photocurrent I_{ph}. The short-circuit current represents the maximum current the SC can produce, meaning a situation where back and front contacts are connected with a lossless wire. Instead of the short-circuit current it is often more practical to use the current density, as short-circuit current density J_{sc}, because the amount of current produced by a solar cell is proportional to its surface area. This way, by using the J_{sc}, we can compare the current producing quality of different sized cells.

An opposite case to short-circuit current is the open-circuit voltage V_{oc} that can be written

$$V_{oc} = \frac{k_B T}{q} \ln \left(1 + \frac{I_{ph}}{I_0} \right) . \tag{2.72}$$

Similarly the open-circuit voltage is the largest possible voltage between the cell's terminals and this occurs when the terminals are not connected at all and the photogenerated carriers build up the voltage by charge diffusion. It is important to realize that neither the short-circuit current nor open-circuit voltage can alone produce power. The solar cell circuit requires additional load, a resistor, that balances the current flow and the voltage build-up. Without produced power the cell is just a diode presented in fig. 2.16. This is why a convenience way to characterize different cells is to examine their power producing capacity $P = IV$. In fig. 2.17 is presented an I-V curve of an ideal solar cell with blue line and the power corresponding to it with red line. Note the reversed current axis that now differs from fig. 2.16. [12]

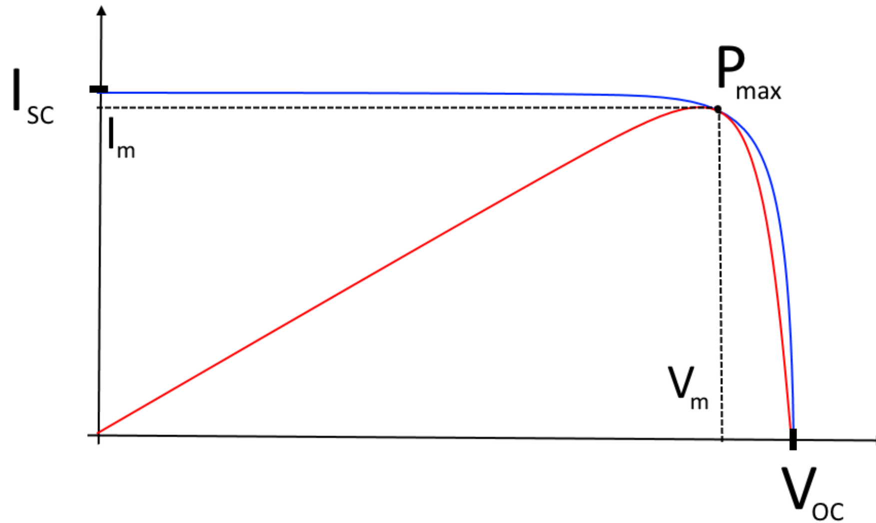

Figure 2.17 *I-V characteristics of an ideal solar cell and the power generating curve corresponding to that. The figure is adapted from source [12].*

The maximum power generated by a cell is illustrated with a rectangle $I_m \times V_m$ and the area of the rectangle is comparable to the total area under the I-V curve. This comparison gives us yet another useful parameter for examining the functionality of the solar cell. The parameter is called the fill factor FF and is calculated as

$$FF = \frac{I_m V_m}{I_{sc} V_{oc}} = \frac{P_{max}}{I_{sc} V_{oc}}. \tag{2.73}$$

The closer the FF is to 1 the better the cell. The more there are loss mechanisms and imperfections affecting the cell, the lower the FF will be. [12] Good usual fill factors can be considered to be values from 0.70 to 0.90, but that is also a cell dependable property and not straightforwardly comparable between different types of solar cells. Usually the fill factor is presented in %, which is just the value of eq. 2.73 multiplied with a hundred. [10] The maximum power of the cell relates its capability to transfer incoming light to electrical energy. The quantity describing this is called the ideal conversion efficiency and it is given by the ratio of the cell's maximum power to the power of the incident light

$$\eta_{eff} = \frac{P_m ax}{P_{opt}} = \frac{I_m V_m}{P_{opt}} = \frac{FF I_{sc} V_{oc}}{P_{opt}}. \tag{2.74}$$

The conversion efficiency is tied to the material's bandgap, which affect both the current and voltage produced by the cell. [102]

This far we have considered only ideal behavior, but in reality the I-V characteristics of the cell have more factors that must be noted. The characteristics of a real

solar cell is usually described with a two-diode model, where additional terms are added to the Shockley's equation 2.71

$$I = I_{ph} - I_{01}\left\{\exp\left(\frac{V+IR_s}{k_BT}\right)\right\} - I_{02}\left\{\exp\left(\frac{V+IR_s}{2k_BT}\right) - 1\right\} - \frac{V+IR_s}{R_p}. \tag{2.75}$$

The non-ideal terms are mainly caused by the series resistance R_s and parallel (shunt) resistance R_p. A circuit describing the operation of a real solar cell is illustrated in fig. 2.18. The photocurrent I_{ph} in the eq. 2.75 might also in some instances be dependent on voltage. [12]

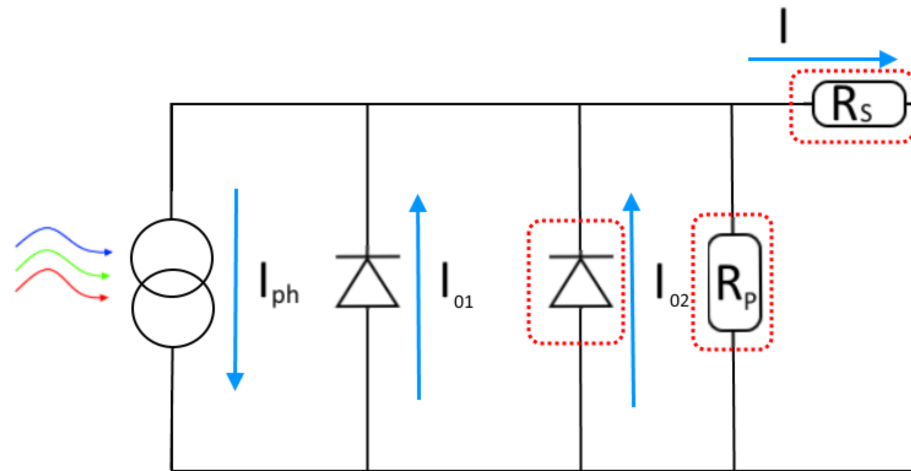

Figure 2.18 *An illustration of the operation principle of the circuit for real solar cell. Non-ideal components are marked with red dotted lines. The figure is modified from the source [12].*

The parallel and series resistance affect the shape of the I-V characteristics and distances it from the ideal curve pictured in fig. 2.17. The two most important sources of the non-ideal behavior are recombination in depletion region and the series resistance. The recombination gives rise to an additional dark current that corresponds to the second diode in fig. 2.18 and in the eq. 2.75. The series resistance is caused by several components that are

1. Cell resistance from emitter and base regions.

2. Contact resistance from front and back contacts.

3. Inner resistance of the front fingers and the bus bar.

The non-ideal behavior affects also the fill factor of the cell. The effect can be written as

$$FF = FF_0(1 - r_s), \tag{2.76}$$

where FF_0 is the fill factor of an ideal cell and the series resistance term is interpreted as $r_s = R_s I_{sc}/V_{oc}$. [12]

To summarize the functions and structure of a single-junction pn solar cell I'll go through the main parts of the cell and their operation. All the parts noted here are illustrated in fig. 2.15. The actual cell is constructed from three components. There are the emitter, the space charge region, also called the junction region, and the base. The emitter and the base absorb the main part of the light and transport the photogenerated minority carriers to the junction region. The strong electric field and the fixed space charge of the junction separates the collected minority carriers. This charge difference creates a potential across the cell and the produced electrical power can be collected with the front and back contacts. Other parts of the cell include the substrate that is similarly doped than the base and the contact semiconductors under the front fingers that are doped as the emitter region. These two parts are for majority charge carrier diffusion to the metal contacts. Addition to these there is also the window layer that is a semiconductor with the doping type of the emitter and its function is to prevent minority carriers from the emitter (opposite to the emitter's doping) to reach the surface and recombine. In the same time the window has to be effectively transparent and transmit the incoming light to the cell structure. And lastly there is the main focus of this thesis, namely the anti-reflective coating, that is supposed to prevent surface reflections and direct the incoming light to the cell. [12]

2.3.2 Properties of Multi-junction Solar Cells

In principle multi-junction solar cells are just single-junction cells that are stacked together. In practice there's much more to it. Mere stacking of single-junction structures on each others would lead to p-on-n diodes and block the current flow. This is why the structure requires additional interconnector layer with a low electrical resistivity and a high optical transmissivity. Widely used solution for this is a tunnel junction that is a thin highly doped p-on-n diode between the subcells. Due to the high doping and a small positive voltage applied to the junction, charge carriers can now tunnel through the barrier, which enables high current density flows at low voltages. In fig. 2.19 is presented the structure of a triple-junction solar cell, that was used for AR coating characterizations. [12]

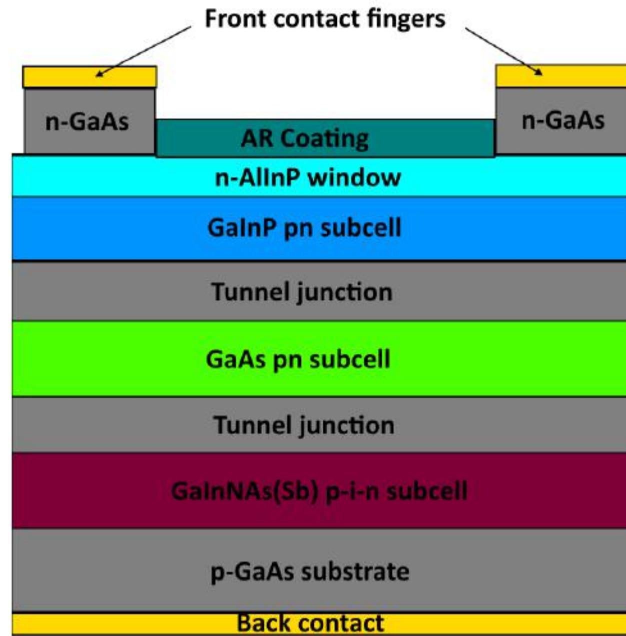

Figure 2.19 *An illustration of a triple-junction solar cell used in this thesis.*

Other thing to consider with MJSCs is the band-gap energies of the subcells, which affect straight what bandwidth range a subcell is able to use from solar spectrum. The trick is to maximize the usage of the incident light and to maintain current balance between the subcells in the same time. Ideally the subcells should produce nearly same current densities, as the least efficient subcell limits the currents in the other subcells and produced additional energy is mostly wasted as heat. Also the stacking mechanisms count when the optimal designs are refined as each semiconductor has their own lattice constant and too great difference between lattice constants of different junctions result in dislocations that cause recombination and other losses. This is why lattice matched designs are preferred to lattice mismatched as there's no need for buffer structures that compensate the lattice mismatch and the design stays simpler. These two methods grow the solar cell as a monolithic item, but in a third option the separately grown subcells can be stacked mechanically on top of each others. This way the subcells do not have to be lattice matched and the MJSCs reach good efficiencies, but the overall costs are much higher than with the monolithic options. [12] The fig. 2.20 presents the solar spectrum distribution for the triple-junction cell used in this thesis. Other ways to combine subcells, than the already mentioned MJSC stacking, include spectrum-splitting via external optics and a polyhedral specular reflector, where the light is distributed with mirror guided reflected beams. [109] The practicality, however, still favors the lattice matched stacking in our case.

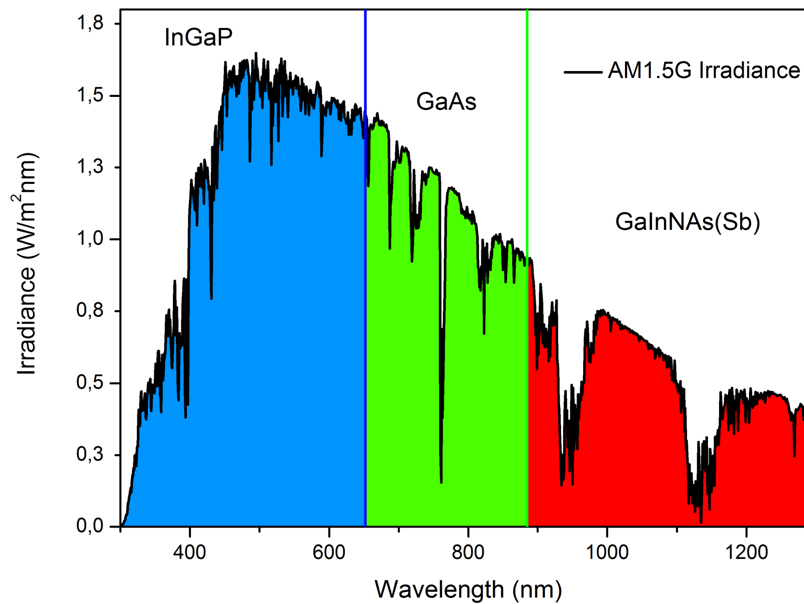

Figure 2.20 *A sketch of the wavelength distribution for the subcells of the triple-junction solar cell studied in this thesis.*

Different MJSCs structures that can be manufactured are for example a lattice-matched SC, a quantum well SC and a SC fabricated with metamorphic growth. [12] The triple-junction cells used for the AR characterizations in this thesis are lattice-matched and fabricated with molecular beam epitaxy (MBE). After the semiconductor layer structure is manufactured, the wafer is processed to add the needed contacts and AR coating. The SCs in this thesis were processed with simple test process for AR coating testing and proper fabrication processes are presented elsewhere. [110, 111]

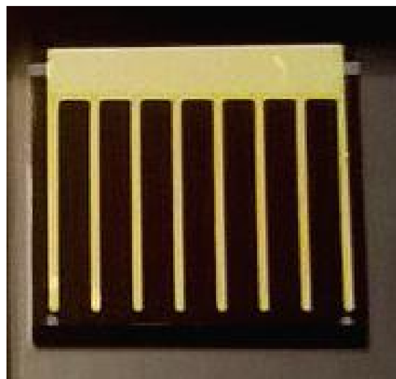

Figure 2.21 *A test process solar cell with the reference AR coating* SiO_2/TiO_2.

The main concern in designing an AR coating for this triple-junction cell is to minimize the reflectance between wavelengths 300 to 1300 nanometers, as can be seen in fig. 2.20. From past experiments we know that the top InGaP subcell is the limiting one for the MJSC in question, so to maximize the produced current, we want the reflectance minimum to lie in the UV range, with the condition that the GaAs subcell does not become the limiting cell. When considering space applicability the range must be widened to 200 nm and if we consider to add a fourth junction the upper limit shifts to 2000 nm. With simple double or triple layer AR coating designs mainly the minimum's location matters, so basically these designs are straightforwardly applicable to the wider bandwidth ranges. When the MJSC is applied within a concentrator unit, the external optics usually guide the light to the cell near the normal incident angle, as can be seen in fig. 2.22.

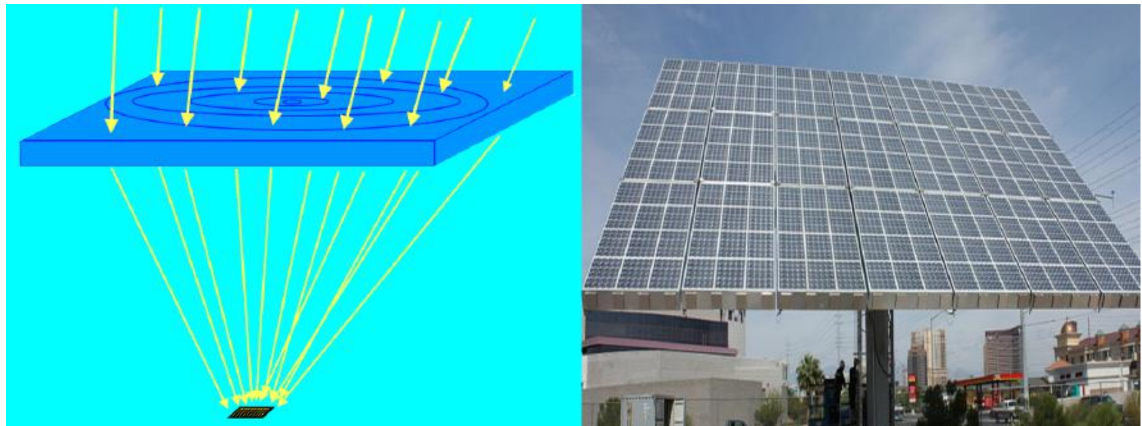

Figure 2.22 *The principle of CPV is to concentrate sunlight to the solar cell by using optics like Fresnel lens. On the right is a terrestrial CPV unit, that is constructed from thousands of concentrator units pictured on the left [112].*

Because of the optical light guidance by the lens, the incident angle considerations are not as crucial for CPV MJSC, as they are for planar systems.

3. Manufacturing and Characterization Methods

The manufacturing and characterizations of the AR films were mainly done at Optoeletric Research Center at Tampere University of Technology. Most of the sample handling and measurements were done in the cleanroom lab at TUT. The ellipsometric measurements of refractive indices as a function of wavelength were done at the University of Eastern Finland by Ph.D Pertti Pääkkönen and the spinnable AR coatings SC510K [89] and SC800i [90] were provided by Pibond corporation [91]. In this chapter are presented the principles behind the used methods and devices and some parametric information about the processes.

3.1 Fabrication of Anti-reflective Coatings

Manufacturing of thin films and anti-reflective coatings includes numerous methods such as sol-gel process, ion-beam sputtering (IBS), thermal evaporation, texturing with nanoimprinting lithography (NIL), ion assisted deposition, electron beam evaporation, plasma enhanced chemical vapor deposition and spin coating. Three latter are used to fabricate the thin films and AR coatings studied in this thesis. Their basic principles of operation and thesis related properties are covered in the next sections and add to that the simulation procedure for AR coating design is presented. All the films used in characterization were grown on test graded 2 inch wide, round and one side polished silicon wafers, meaning that they could have any type of doping, resistivity, orientation and flats. The used growth parameters are tabled in the appendix A.

3.1.1 Electron Beam Evaporation

EBE is a physical vapor deposition (PVD) method and thus belongs in the same category with thermal evaporation, sputtering and IAD. In PVD the thin film growth is based on physical process of particles adsorbing to the sample surface, where they form a layer structure. The Instrumentti Mattila Electron beam evaporator, that

has been built for ORC as a custom design, was used in evaporation of MgF_2, TiO_2 and Al_2O_3. Other currently available dielectric materials to that system include Ta_2O_5 and SiO_2. The EBE system contains two separate vacuum chambers, the sample chamber and the material chamber, with integrated pumping systems, a crucible holder where the evaporated materials are held and an electron beam linear. Add to these there are a rotatable sample holder, shutters between the chambers, a lamp for sample heating and three windows for which two are for observing the crucibles during the evaporations and one for sample monitoring. The electron beam is directed with a magnetic field and an acceleration voltage and the beam current can be controlled remotely. In the figure 3.1 there is presented the actual EBE system and a schematic of it's working principle.

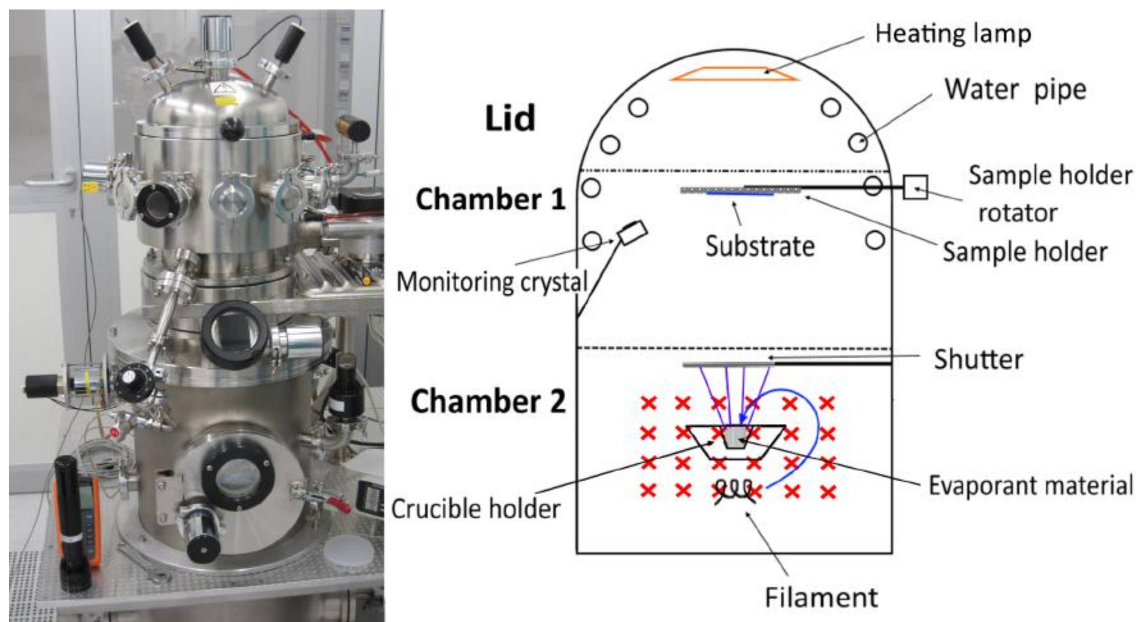

Figure 3.1 *The electron beam evaporator in cleanroom at TUT and a schematic view of its function.*

As the evaporator is divided in two separated chambers it is possible to insert the substrate without the need of breaking the vacuum in the material chamber. The chamber 2 can be sealed during the changing procedure and the chamber 1 is then purged with N_2 gas and heated with hot water to prevent any contaminants from air from attaching to the chamber walls. When the sample is in place the chamber 1 is sealed with the lid and the vacuum pumping starts. As the vacuum reaches low enough pressure the seal between chambers open and evaporation can be started when the required pressure level for the evaporated material is reached. Some of the materials, like TiO_2, require additional oxygen to stabilize the refractive index, as they tend to degas during the evaporation. This extra oxygen is added through separate line and the flow is controlled with a needle valve.

Usually a commercial EBE systems include moving or planetary rotating substrate holders so that the produced film would have as uniform structure as possible since the evaporated material distributes as a spherical source from the crucible, thus leading a slight thickness variation over planar surface. [17] Since the sizes of our samples are rather small and the MJSC size is even smaller the stationary holder included in the used EBE can be considered sufficient. Although the two inches wide silicon substrates had uneven film thickness distribution about the scale of ± 2 nm, the variation is negligible as our evaporation thickness cannot be controlled more precisely than that, as it depends on a mix of manually regulated parameters.

In the table A.1 is presented some evaporation parameters used in this thesis for EBE coating as there are several important factors such as growth rate, substrate temperature, pressure, current and voltage that all affect the quality of the deposited films. In addition to these one have to calibrate the actual growth rate with respect to the rate measured by the monitoring crystal. This is done by calculating a tooling factor (T_F) for the used material and parameters. The T_F is defined by the equation:

$$T_F = T_{approx} \times \frac{d_f}{d_{quartz}}, \tag{3.1}$$

where T_{approx} is T_F value, that is used in the calibration evaporation, d_f is the film thickness measured by ellipsometer and d_{quartz} is the thickness value given by the quartz crystal. [113] The calibration of tooling factor therefore requires an evaporation with an approximated value for the T_F and then comparison with the actual parameters measured after the calibration evaporation. Tooling factor is dependent on the evaporation conditions such as pressure and temperature and the material that is evaporated. The previously done evaporations usually give a good approximation for the T_{approx} of the material, that can be used in the calibration procedure. The T_F is also dependent on the placement of the quartz crystal so it is a device spesific parameter, so it must always be calibrated for the given setup. [113]

In this study EBE was used to fabricate MgF_2 thin films for characterization and to manufacture AR coatings MgF_2/TiO_2 and $MgF_2/TiO_2/Al_2O_3$. In addition to this the reference coating SiO_2/TiO_2 was made with EBE and for the AR coatings with nanoporous SiO_2 and siloxane SC510K, the high index layer of TiO_2 was also deposited with EBE. The main parameters for AR coating depositions can be found in table A.4.

3.1.2 Plasma Enhanced Chemical Vapor Deposition

In chemical vapor deposition the thin film is grown by introducing precursor gases to the reactor chamber, where they react together and form a layer of wanted material

on the substrate. The precursors are in the vapor phase and are moved to the chamber by carrier gas or they can be gaseous themselves. The reaction is activated by plasma pulsing, which allows cooler substrate temperature and forms more densely packed and uniform thin films. [17] This plasma controlled method is called plasma enhanced chemical vapor deposition and is nowadays the main type of CVD processing. The reaction induced by plasma activation can be divided in three categories that are reactions with electrons, reactions between heavy species such as ions and heterogeneous interactions with surface. The sub-reactions are numerous and this is why detailed modelling of PECVD reactions is complicated. To maintain process repeatability the process parameters must be well known and kept as constant as possible for wanted outcome. Such parameters are chamber pressure p, gas flows, discharge excitation frequency f, power P, table temperature T_s and the electrical potentials. [114]

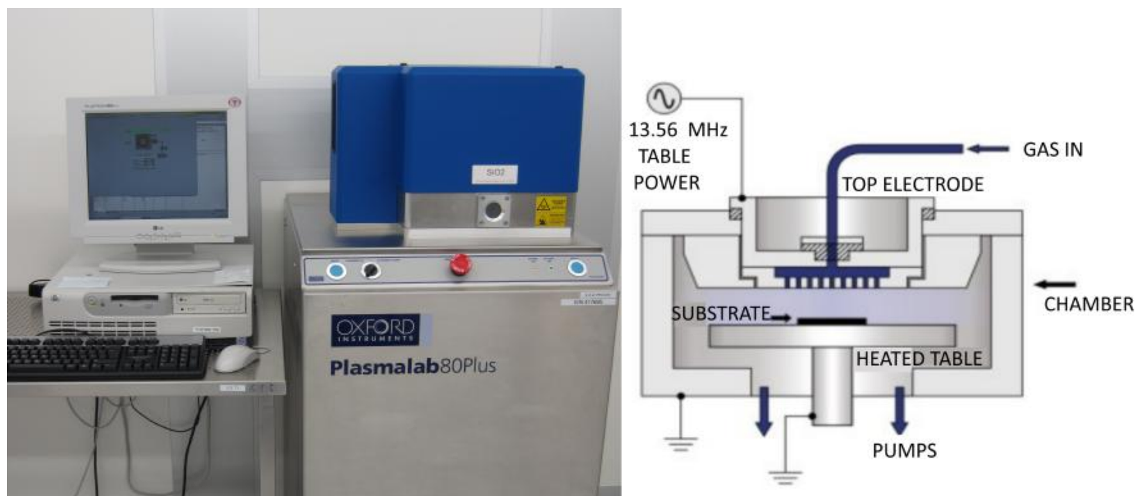

Figure 3.2 *At left the plasma enhanced chemical vapor deposition system in the cleanroom at TUT and at the right the illustration of the used PECVD system applied from [115].*

In this thesis a commercial Oxford Instruments PlasmaPro 80 PECVD system was used. It is a parallel plate plasma reactor that operates with radio-frequency (RF) system that is illustrated in fig. 3.2. The system at ORC has reaction precursors both for SiN_x and SiO_2 deposition, but only the latter was fabricated. The stoichiometric equation for SiO_2 states:

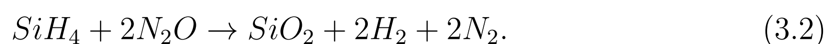

$$SiH_4 + 2N_2O \rightarrow SiO_2 + 2H_2 + 2N_2. \tag{3.2}$$

Here the precursor gas for SiH_4 was 2% dilution of SiH_4 with an inert carrier gas N_2. The PECVD was used to produce nanoporous SiO_2 by altering the table temperature T_s and flow ration of N_2O:SiH_4 as the device manufacturer states that by

lowering temperature and growing the mentioned flow ratio the refractive index of SiO_2 reduces [116]. This would mean higher oxygen content in SiO_2 and probably porosity as pores filled with air are an effective way to lower the refractive index. The parametric info for different depositions are tabled in table A.2. The temperature range was from 400 °C to room temperature and the 2%SiH_4/N_2 flow rate was lowered from the conventional 425 sccm to as low as 25 sccm. These are basically the physical limits of the device as the temperature range is given by the manufacturer and the flow rate could not be further lowered as the system had already troubles of stabilizing the pressure during the process, as the actual flow fluctuated between 14 to 20 sccm.

3.1.3 Spinning Method for Thin Film Manufacture

Spinning is a method where a solution of a solvent and the coating material is dispensed on the wanted substrate, that is mounted on a spinning plate, and then the uniform layer is formed by spinning the plate. During the spinning most of the solvent evaporates and after spinning the coatings are usually dried and tempered to finalize the structure. The method provides an easy way to produce uniform films, but downsides include difficulty to produce multicomponent compositions or multilayer structures as between different coatings the layers have to be baked. Spinning is widely used to deposit different kinds of photoresists for microelectronics production. [117] In fig. 3.3 is presented the schematic principle of how the spinning process for siloxanes SC510K and SC800i was done.

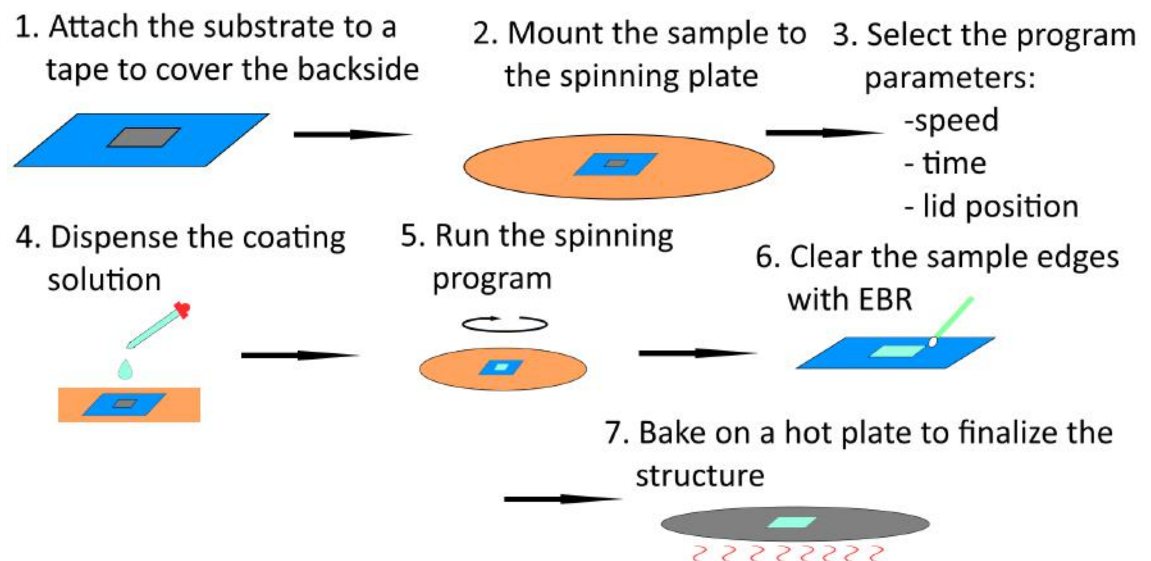

Figure 3.3 *Simplified illustration of the spinning procedure.*

Firstly the substrate is attached to a tape, so that the backside of the substrate

is covered from the spinnable coating. Any residual coating that would have got to the backside of a solar cell, could possibly decrease conductivity and increase series resistance. After this the sample is mounted to the spinning plate, where the vacuum holes suck the sample firmly to the platform. Next the user has to choose appropriate program for the coating or create a new one, suitable for the coating in question. Adjustable parameters include the round speed of the spinning rpm, spinning time t and whether the lid stays open or closes during the spinning. The programs have several steps, which numbers can be altered as well. When the right program is ready for the run, it is time to evenly dispense the coating solution on the sample. And then the program is started. As the spinning stops and the vacuum is released, the edges of the sample should be cleaned with edge bead remover (EBR), that suitably should be chemically similar to the solutions solvent if not the same. If there's any altering to be done to the coating, such as cleaning the solar cell's bus bar, it has to be done at this point, as after the curing the structure has great mechanical and chemical durability and the removal of unnecessary coating parts would be difficult. Finally the coating is cured in 200 °C for five minutes. This gives the structure its final form and makes it more durable.

In this work the Pibond corporation's commercial AR coatings SC510K and SC800i were deposited with spinning on the wanted surface structures. The spinning was done with OPTIcoat ST23+ spinner and the used parameters are tabled in the table A.3. The method itself is rather simple as described before. The solutions were dispensed manually and the variable parameters included the spinning speed, time and whether the spinner plate's cover was open or closed during the spinning. All the samples were baked on a hot plate in 200 °C for 5 minutes after the spinning.

3.1.4 Simulation and Optimization of the Anti-reflective Coatings

The AR coating structures were simulated and optimized with Essential Macleod Optical Coating Design Program to find the best possible structural parameters for the used material layers. The program uses material databases, where the optical constants for different materials are filed. The material file of a certain substance includes refractive index and extinction coefficient values for different wavelengths. As a part of this thesis I created some new material files for AR coating simulations for differently deposited MgF_2, SiO_2 and SC510K, as the optical properties are somewhat dependent on the deposition conditions. These files were used for the AR coating optimization for the MJSCs. The design window for structure editing is presented in fig. 3.4 with the refined design of MgF_2/TiO_2 double layer AR.

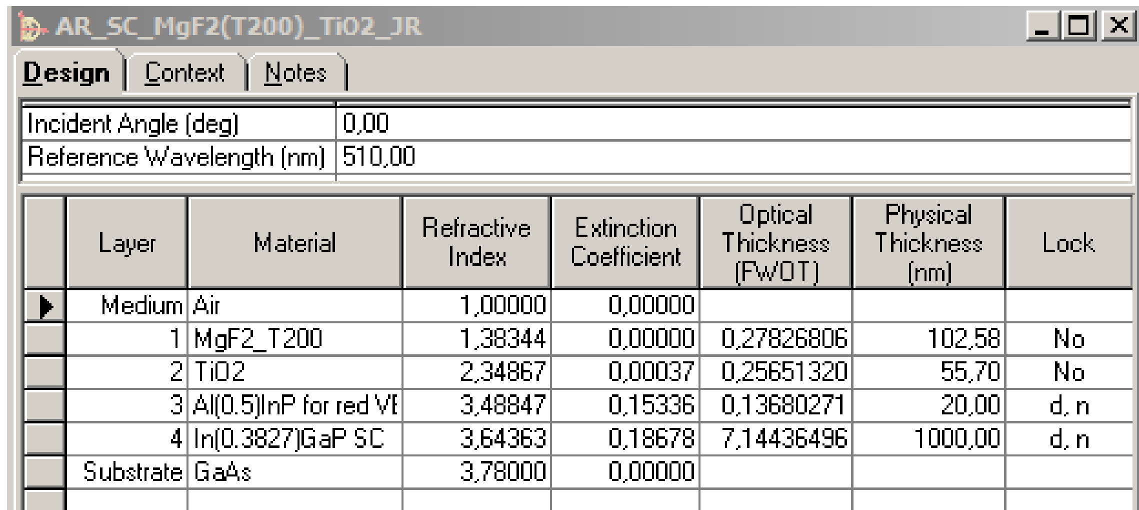

Layer	Material	Refractive Index	Extinction Coefficient	Optical Thickness (FWOT)	Physical Thickness (nm)	Lock
Medium	Air	1,00000	0,00000			
1	MgF2_T200	1,38344	0,00000	0,27826806	102,58	No
2	TiO2	2,34867	0,00037	0,25651320	55,70	No
3	Al(0.5)InP for red VE	3,48847	0,15336	0,13680271	20,00	d, n
4	In(0.3827)GaP SC	3,64363	0,18678	7,14436496	1000,00	d, n
Substrate	GaAs	3,78000	0,00000			

Figure 3.4 *The design window for an anti-reflective coating. This window includes all the parameters given to the program for structure optimization.*

This window is the most important tool in Essential Macleod as it includes all the information that the program needs for layer optimization. First at the upper side of the window the user has to define the wanted incident angle θ_i and the reference wavelength λ_0 for which the program optimizes the layer structure. In our case the incident angle was set to 0 degrees and the reference wavelength was chosen to be 510 nm, that corresponds to the peak of solar irradiance presented in fig. 2.14. The parameters required for the start of optimization process are the wanted layers from incident medium through thin films to the substrate. For each layer the wanted material is chosen from the material database and the program uploads the correspondent optical constants n and k. In addition to the layer composition the user has to choose the optical or the physical thicknesses for the layers. When either is input the program automatically calculates the other. Our starting point for thicknesses was a quarter-wave optical thickness as 0,25 full wave optical thickness (FWOT). As the optimization process refines the layer structures it is useful to lock layer parameters of some layers that are not actually part of the layer design. In this case the layers corresponding to the window material and the first SC junction are not variables and are therefore locked from optimization. To simplify the required data for optimization only the window layer and the topmost cell of MJSC are simulated on top of a GaAs substrate. This is due to the assumption that the rest of the light, that is not reflected from these layers, is absorbed by the MJSC stucture and no significant back reflections from these layers occur. This is not actually true, but it's close enough for structure optimization. The approximated layer structure for simulation and optimization is presented in fig. 3.5. The appropriate material files for AlInP window and GaInP junction were obtained from ORC's material

database.

Figure 3.5 *The layer structure that simulates the MJSC's configuration.*

Essential Macleod includes automatic refinement and synthesis options, which improve a starting design and construct additional elements, when needed. In this case the total layer number is limited for each AR coating starting design, so we focus on refinement. The designs produced by the refinement are evaluated by a figure of merit, which converges to the optimum design. The Simplex refinement finds the nearest merit function minimum for the given starting design. Only input it requires are starting design and whether it refines layer thicknesses, refractive indices or both. After this the program iterates possible designs to find the optimum. Another useful process process is the Optimac refinement and synthesis, which can also be used to refinement only. The Optimac has more input choices and greater chance of adjusting the refinement parameters as merit function limits and number of iterations for example. The results of refinement can be given as reflectance or transmittance graph and the structure corresponding to this result. In fig. 3.6 is presented the reflectance of optimized MgF_2/TiO_2 AR coating in accordance to the incident angle of the incoming light. [118] As it can be seen in fig. 3.6 the incident angle does not crucially change the AR coating's reflectance within a reasonable angle range (0–60 °). It has also been stated that in CPV systems the optimum layer thicknesses for wide-angle MJSC AR coatings are very near to the optimal values for 0 ° incident angle. [119] This is why in this thesis we focus to examine only the normal incident angles and further broad-angle considerations are neglected.

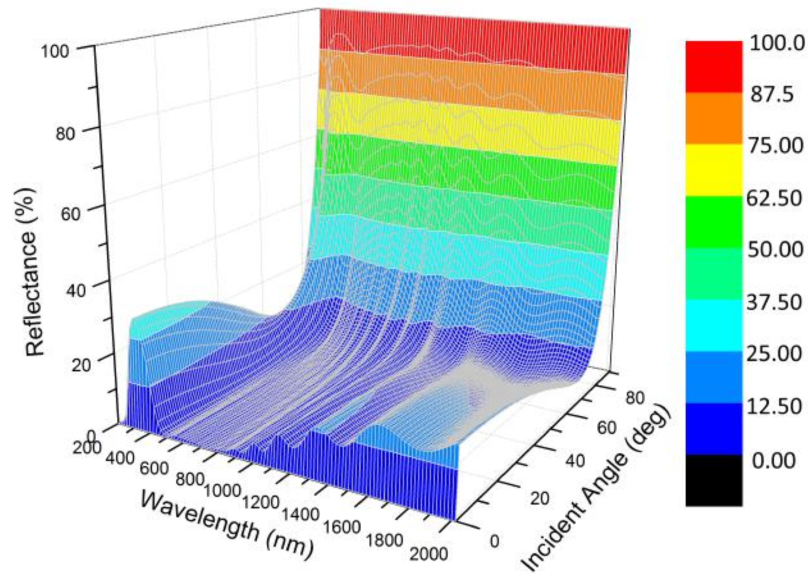

Figure 3.6 *The program is also able to model the reflectance behavior in various angles, which is important to overall evaluation, when the incident angles are a key question.*

With the help of Essential Macleod three double-layer AR coatings and one triple-layer coating were constructed and refined. These coatings were constructed as MgF_2/TiO_2, nanoporous SiO_2 with TiO_2, SC510K/TiO_2 and $MgF_2/Al_2O_3/TiO_2$. In the chapter 4 each of these designs have their own section, where their functionality is examined.

3.2 Characterization Methods of Thin Films and Solar Cells with Anti-reflective Coatings

After the films and AR coatings were manufactured their properties were evaluated with different methods to characterize their functionality and optical behavior. Next sections briefly cover spectroscopic ellipsometry, spectrophotometry, atomic force microscopy (AFM), scanning electron microscopy (SEM) and I-V measurements for the SCs in the scale they are used in this thesis.

3.2.1 Ellipsometric Measurements and Spectrophotometry

Ellipsometric measurements were used to find out the optical constant n and the thickness d of the fabricated thin films. A monochromatic nulling ellipsometer was utilized to quick quality analysis of the films after deposition and variable angle

spectroscopic ellipsometer (VASE) was used to measure the dispersion curves of the MgF_2, SiO_2 and siloxane coatings. In addition to this the reflectances of the films and AR coatings were acquired with spectrophotometer and photoluminescence (PL) mapper. In this section the measurement sets are briefly described and some insights pointed out in relation to the measured samples.

The ellipsometric measurements of thin films are based on the polarization changes in light when it reflects from a surface. The optical constants n and k can be directly calculated from the measured Ψ and Δ, where Ψ is the relative amplitude change and Δ is the phase difference between p- and s-directions of the complex Fresnel reflection coefficients, with the given wavelength and angle of incident. [16, 120] In the measurements of the film thickness and refractive index of the deposited thin films a monochromatic ellipsometer Rudolph Auto EL III Ellipsometer was used. The device used is presented in fig. 3.7. The ellipsometer operates with a Helium-Neon-laser of 632.8 nm wavelength and the angle of incidence of the beam is $70\,^\circ \pm 0.02\,^\circ$. [121]

Figure 3.7 *The Rudolph Auto EL III Ellipsometer that was used in ellipsometric measurements.*

A monochromatic ellipsometer has its uses as a quick characterization method for film thickness and refractive index at one wavelength, but as was explained in section 2.1.1 most of the materials have some amount of dispersion, meaning that the refractive index differs according to the wavelength of the incident light. To measure the dispersion behavior of a thin film requires a broadband light source, adjustable monochromator and rotating analyzer ellipsometer (RAE). The comparison between

monochromatic ellipsometer, which in this case is a null ellipsometer, and RAE is presented in fig. 3.8. [16]

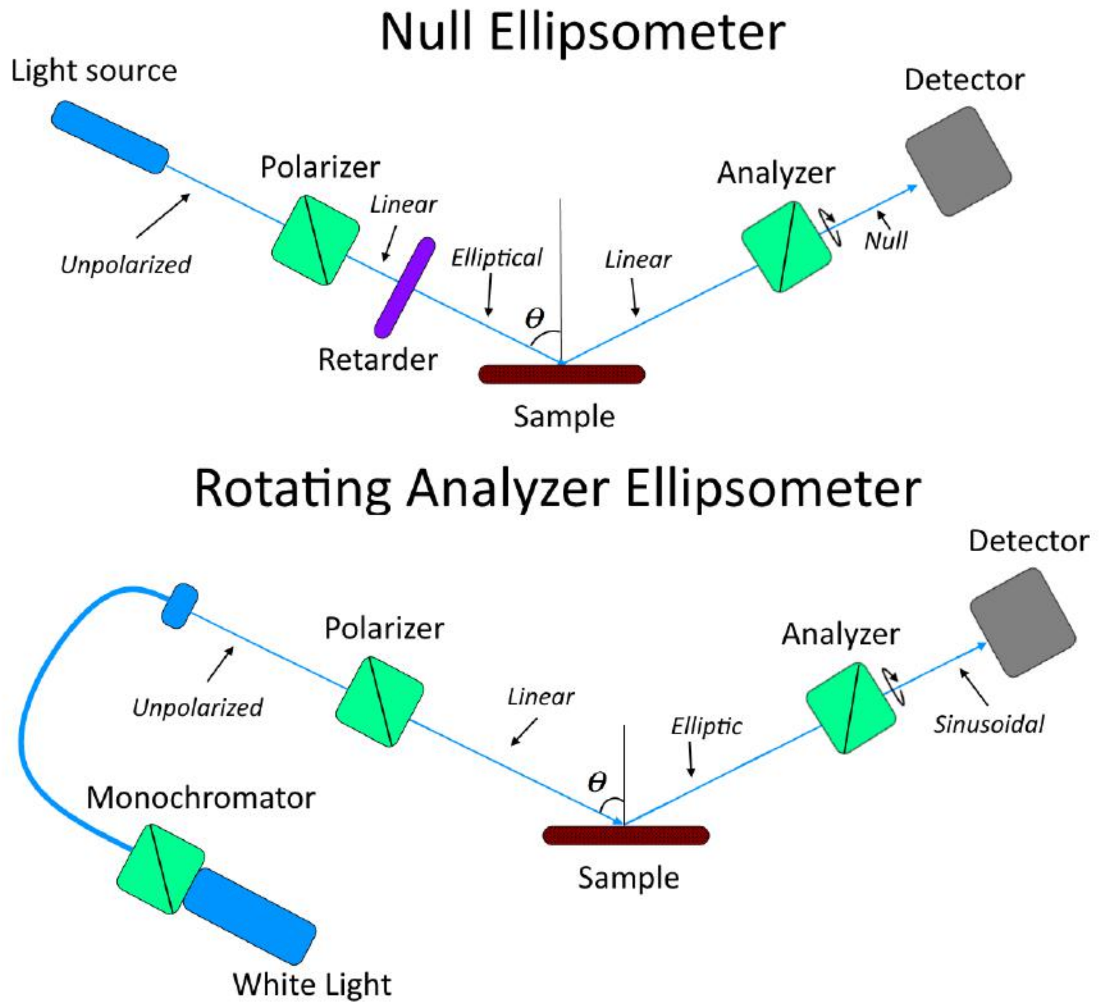

Figure 3.8 *The working principles of null ellipsometer and RAE. The figure is based on the reference [16].*

The null ellipsometer works with the principle, that it finds the intensity minimum by rotating the polarizer and analyzer. After this it calculates from their azimuthal angles and the angle of incidence θ, the needed ellipsometric parameters Δ and Ψ. From these parameters can be interpreted the wanted d and n. RAE is different in the way that the polarizer is set to the angle of $45\,^\circ$ and instead of finding the minimum, the rotating analyzers creates sinusoidal signal that it uses to calculate Δ and Ψ. Ellipsometric calculations presume that upon reflection from samples no depolarization occurs. In real measurements, however, the samples can depolarize the incident light beam and sometimes this raises issues. It is also notable that the film thickness is given by a periodic function and thus the film thickness may as well

be the given value plus the product of the periodic term

$$\tilde{d} = \frac{\lambda}{2\sqrt{n_1^2 - (n_0 \sin\theta)^2}}. \tag{3.3}$$

When a possibility to change incident angles is added to multiple wavelength RAE, the name becomes variable angle spectroscopic ellipsometer (VASE). [16] A VASE was used in the measurements to figure out the dispersion curves for the characterized thin films.

In addition to the measurement systems, the ellipsometry requires usage of models for optical properties of solids. The three most important are

1. The classical Lorentz oscillator model for semiconductors and dielectrics.

2. The classical Drude model for metals.

3. Generalized quantum mechanical models for amorphous and microcrystallized semiconductors.

The measurement data must also be fitted to a model and evaluated with a figure of merit, such as mean squared error or the goodness of fit. When the sample does not directly fall to any of the above mentioned categories one can try to fit it into an effective medium approximation (EMA). They usually construct some distribution between the host material and the minor participant and calculate the optical constants n, d and k according to that assumption. [16]

Good features of spectroscopic ellipsometry are that it is non-invasive, non-destructive, non-contact, and that it allows determination of several film properties such as refractive index n, extinction coefficient k and thickness d simultaneously. No special sample preparation is needed, as long as the surface is not contaminated, and the measurement is relatively fast. The method is also precise, reproducible, covers a wide thickness range of thin films from sub-nanometers to tens of microns, and it has a wide spectral range from around 200-2000 nm. [16]

In the reflectance measurements a commercial PerkinElmer 1050 UV/VIS/NIR spectrophotometer was used with two different accessory unit. With the universal reflectance accessory (URA) the reflectance is measured straightforwardly as the sample is illuminated with monochromated light and only the intensity of the light that is directly reflected back to the detector is taken into account. This method neglects the scattered light and only straight reflectance is measured. Using URA is a practical way to gain relevant reflectance data from similar sample series and the given results deviate only little from the actual total reflectance, if the sample surface can be considered smooth and non-scattering. The other accessory, integrating sphere, is more precise and guides also the scattered light to the detector. This

way we can reliably measure the total reflectance of our samples. The basis of the measurement is essentially the same than with URA, but the sample and the detector are placed within a white sphere, that reflects all the light from its walls and directs it to the detector. This way all the incident light reflected from the sample reaches the detector. In fig. 3.9 is an illustration of the mechanisms, how the spectrophotometer functions.

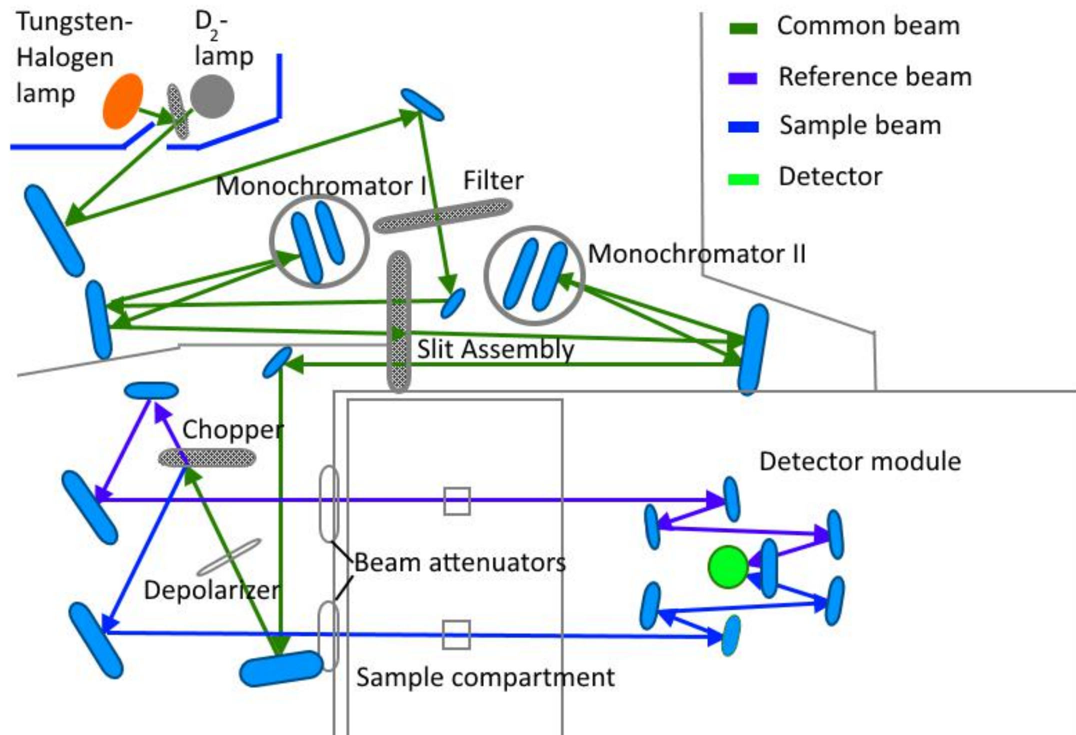

Figure 3.9 *An illustration of the working principle of a spectrophotometer. The figure is modified from source [122].*

Both accessories require a baseline calibration, that measures the actual intensity that is given from the lamps. This value is then used to determine the amount of reflected light. The accessory modules work with a plug-and-play principle, so any crucial mirrors and filters are not affected by the change of the module. With the initial measurement setup one can adjust the range of wavelengths that are being measured and the interval of the measurements. In this study the range varied from 200 to 1200 nm for thin films and from 200 to 2000 nm for AR coatings. The measuring interval was either every 5 nm or 10 nm depending on the measurement. The measurements begin from the larger wavelength end and continue downwards the scale. This wide measurement range requires a change of detector at the 890 nm from InGaAs to PMT and a change of light source from tungsten to D_2 lamp at the wavelength of 320 nm. The spectrophotometer does these changes automatically,

but at the detector change, there is a slight discontinuity between the curves. In the plots of AR coating reflectances the discontinuity spike was interpolated out off the graphs, as it has no real physical meaning and relates only to the measurement system.

The URA module was used to measure the thin film reflectances and the integrating sphere was used for the actual AR coatings. As ellipsometry is an effective way to find out the optical constants of the thin films also photometric measurements of reflectivity and transmittance can yield rather good values, when fitted into a right model. In fig. 3.10 there is some comparison between approximate refractive index profiles modeled only with reflectance data and then also the curve from ellipsometric measurements. The curves are labeled according to the measuring system and the applied model. Also three reference curves for MgF_2 are included as Dodge [48], Li [123] and Sopra database [124].

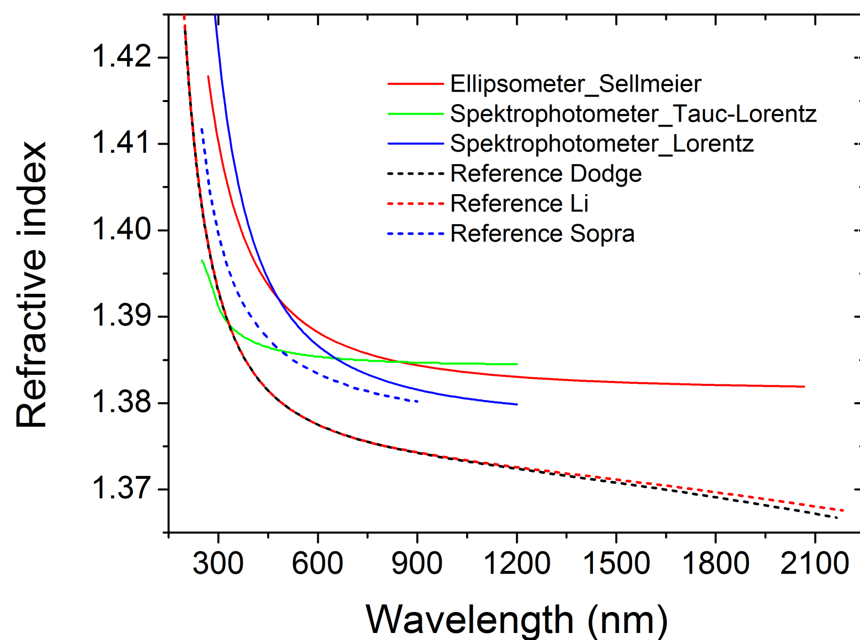

Figure 3.10 *The refractive index profiles for MgF_2 sample acquired with different measurement methods and models.*

The values gained from reflectance modeling would really require also transmittance measurements, that were not included at the time. Despite this lack of data the models give a rather good guess of the film's dispersion

In addition to spectrophotometer measurements a photoluminescence mapper was used to determine the reflectances of the AR coatings to get comparable measurement data. The main difference compared to the spectrophotometer is that

PL mapper requires reference mirror measurements to gain the actual scale of the reflected light from the measured signal. This is done by comparing the measured mirror signal to a known reflectance spectrum of the mirror. The reference spectra for the PL mapper measurements were obtained from Filmetrics Reflectance Calculator [125]. In these measurements a commercial PL Mapper Accent RPM2000 was used and mirrors made of silver and gold were used for the reference measurements. The silver mirror had also a thin Al_2O_3 overlayer of 20 nm thick, but that was taken into account with the reference spectrum.

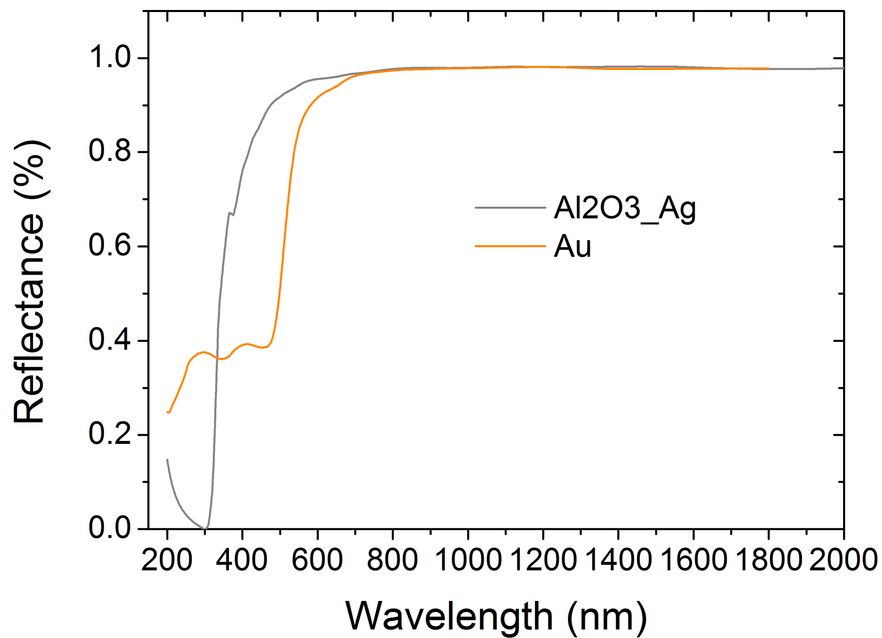

Figure 3.11 *The reference mirror reflectances used to calibrate the PL Mapper Accent RPM2000 for AR reflectance measurements.*

As the slit widths, gratings, photosensors and mapping speed had to be changed for different bandwidth ranges to cover the whole bandwidth utilized by MJSCs, several calibration measurements were made. Each of these bandwidth parts required different parameters to maximize the signal produced by the photodetector and same time to ensure that the detector will not saturate through too large illumination. Too low signal creates larger background noise and makes the measurement less accurate. The signals of the calibration measurements are shown in fig. 3.12.

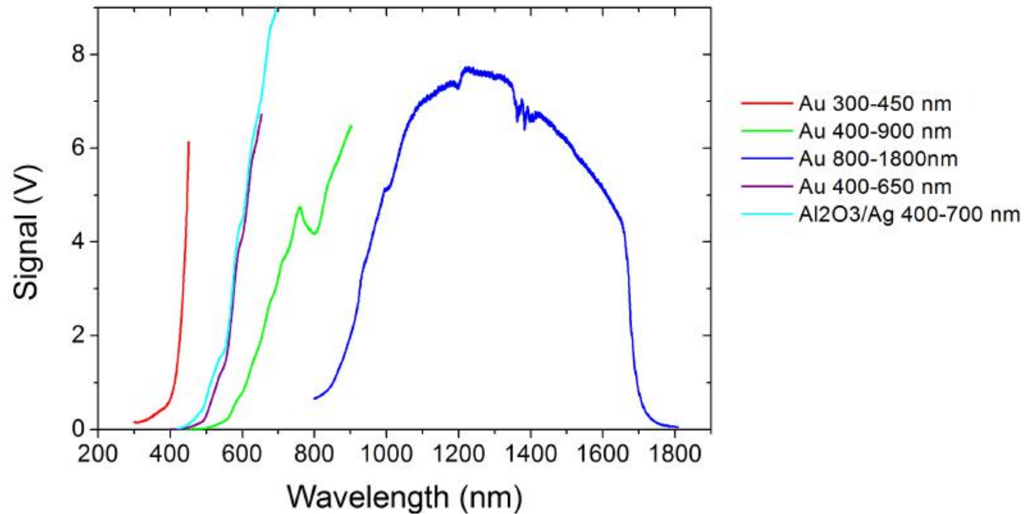

Figure 3.12 *Calibration signals of PL mapper measurements for AR reflectances.*

The range from 400 to 500 nm was especially difficult to measure due to the reference mirrors steep change of reflectivity at that bandwidth range that can be seen in fig. 3.11. The steepness of the reference spectra results steep calibration signal as well, where the lower wavelength region has nearly insufficient signal, which can be seen in fig. 3.12. However, when combining these overlapping measurement regions a suitable reflectance over the bandwidth range from 400 to 1700 nm is acquired. It is notable that the PL mapper cannot accurately measure the reflectance below 400 nm because of the reference mirrors' varying and vanishing signals that can be seen in fig. 3.11.

3.2.2 Atomic Force Microscope

Atomic force microscope is a scanning probe microscope (SPM) that differs greatly from optical microscopes. It does not require sample illumination by light nor lenses for image forming. Instead of optical input AFM uses atomic level forces to obtain information from the sample surface. This is done by measuring the force interactions between the scanning tip, that is attached to a plate spring called cantilever, and the surface atoms. As the tip is moved across the surface the strain to the cantilever depends on the topography of the atoms the tip is passing. As the interaction forces create deflections of the cantilever, a laser beam collimated to reflect from the cantilever's head has changes in its reflection angle. These changes are observed by a photodiode and the distance changes between the tip and sample surface can be calculated. The measurement setup can be seen on the left side of the fig. 3.13. The overall topographical picture of the sample surface is then obtained by scanning line per line the wanted surface area and combining these to one complete surface map.

The right side of fig. 3.13 illustrates the tips movement across the surface. [126]

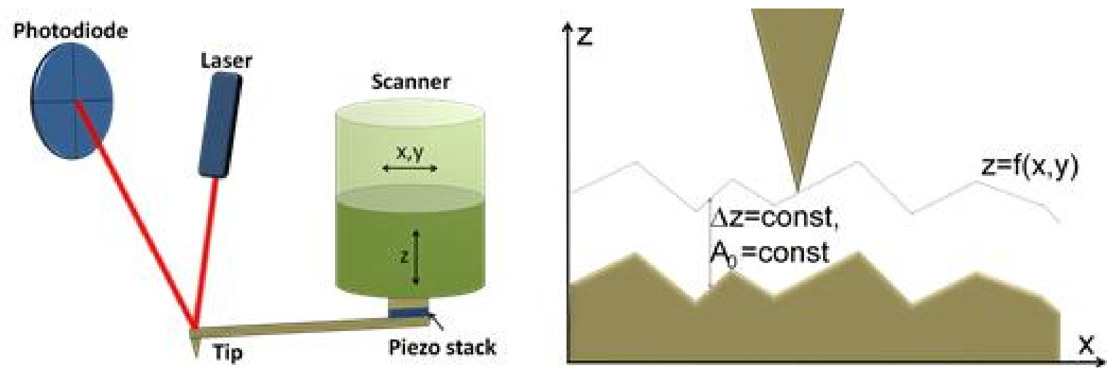

Figure 3.13 An illustration of the working method of AFM. The figure is modified from the source [127].

In the actual measurements the dielectric nature of MgF_2 caused challenges as the silicon tip seemed to charge up fast during the measurements and the data's quality degraded at the same time. The linearly degrading sample image is presented on the left side of fig. 3.14 and as a reference the surface structure of MgF2 deposited in 50 °C and covered with thin gold film can be seen on the right. The imaging in both of the measurements was started from the top of the frame continuing downwards the image. As it can be seen from the left side of the fig. 3.14 the picture becomes more and more blurred as it closes down the frame and in the end some stamping effect is also noticeable. Further evidence of charging was the fact that measurements with the same tip and different sample after a reasonable time showed no sign of degradation and a good image data could be retrieved. This would indicate that a tip contamination by the surface rubble was unlikely.

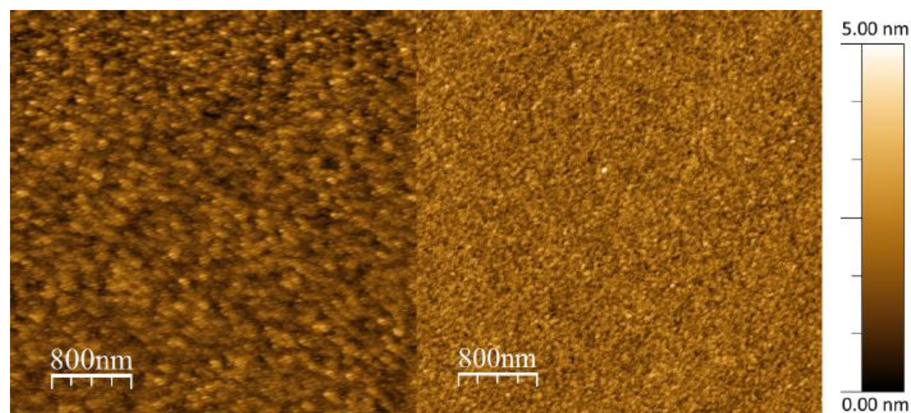

Figure 3.14 On the right an AFM picture of MgF_2 covered with thin Au overlayer and on the left an example of the linear degradation of the image quality of the sample, when no additional metal layer was added. Both samples were deposited with 50 °C substrate temperature.

To overcome this degrading and to get some comparable data of the structure changes between the samples a thin gold overlayer was deposit on the samples. The approximate thickness of the Au overlayer was from 2 to 3 nm and the deposition was done with EBE. With the gold coverage no degrading was observed. It is presumable that some surface properties were lost due the gold coverage, but the overall roughness comparison between the samples holds true as the gold layer can be approximated to be uniformly distributed [128] over the sample surface and as the evaporation was done simultaneously to all samples the thickness variations of gold layers between the samples are negligible.

With AFM measurements we want to characterize the surface structure of our samples. AFM draws a surface map that shows the height variations of the sample and the shape of the molecular structure of the surface. The roughness analysis and imaging of the samples were done with WSxM 5.0 Develop 8.2 software [129]. Parameters that were examined were root mean square of roughness ($rmsr$), roughness average (ra), average height ($< a >$), surface skewness (S) and surface kurtosis (K). Most important parameters and widely used in engineering for characterization is root mean square of roughness $rmsr$ and roughness average ra and the other values are more or less additional statistical values. However the program gives a rather thorough analysis over the measured surface area and for interested reader the statistical values are tabled in the appendix B for different samples. In fig. 3.15 is presented the overall roughness analysis data for a single measurement.

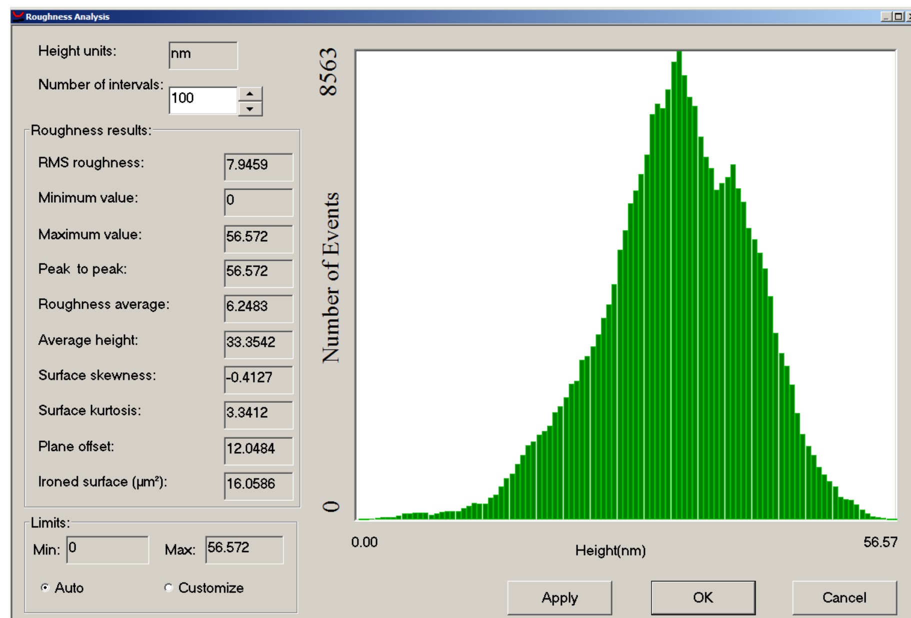

Figure 3.15 *The roughness analysis presentation in the WSxM program, where on the left the program have evaluated all the roughness parameters and on the right the program presents a histogram of the heights.*

As the scanning tip moves across the sample the deflections of the cantilever are registered as height differences of the surface. The measurement gives height distribution of the sample points as can be seen in fig. 3.15. The average height of all the points $< a >$ is calculated with expression

$$< a >= \frac{\sum_{ij} a_{ij}}{N}, \tag{3.4}$$

by summing the heights of all measurement points a_{ij} and dividing that with the number of total measurement points N. In surface characterizations for used dielectrics and siloxanes the roughness average ra is defined as

$$ra = \frac{\sum_{ij} |a_{ij} - < a > |}{N}. \tag{3.5}$$

The average gives a comparable figure for surface roughness between different samples. Another such number is root mean square roughness that is given by the expression

$$rmsr = \sqrt{\frac{\sum_{ij} (a_{ij} - < a >)^2}{N}}, \tag{3.6}$$

that is a weighted value of the surface roughness and gives a little larger values than ra. These three figures give a rather good picture of the surface roughness and are the main focus for AFM measurements in this thesis. In the appendix B. also the surface skewness S and kurtosis K are tabled, but they are left as additional info. [129]

The overall reason for surface roughness characterization lies in its impact on the surface scattering. The rougher the surface the more scattered light, which decreases the amount light entering the solar cell. This is why for proper AR coatings a smooth surface is an important feature, as it decreases the scattering effects. The top layers of each coating was measured and analyzed with AFM to give a good picture of their surface roughness.

3.2.3 Scanning Electron Microscope

In characterizing the porosity of the films and the overall film structures a scanning electron microscopewas used. The used SEM at ORC cleanroom is a field emission scanning electron microscope (FESEM). Difference to a regular SEM is the way that the electron beam is created. In regular SEM the beam is created by heating tungsten or LaB_6 filament and the electrons are exited merely by the thermal processes. In FESEM the filament is usually also made of tungsten, but its shape is more of a sharp tip and an electric field is set to drive the electrons to the tip's head, where

they exit the tip via tunneling effect. [130] The type of the device is a commercial ΣIGMA™ FESEM that is operated with SmartSEM® software, both products of Carl Zeiss NTS Ltd.

The working principle of a SEM is to sweep the imaged surface with a narrow electron beam and collect the emitted electrons from the surface with different kinds of detectors depending on the type of electrons that are monitored. From these sweep lines an image is formed and in these days this is most often done digitally. The signal from the surface is formed by several electron interactions with the surface. The electron beam from the gun is called the primary electrons (PE) and the rest are secondary electrons (SE) and back scattered electrons (BSE). The secondary electrons are divided in three classes depending on their birth mechanism:

- SE1: electron emission formed by the primary electrons hitting the sample.
- SE2: electron emission formed by the backscattered electrons within the sample.
- SE3: electron emission formed by the backscattered electrons in the sample chamber.

The difference between secondary electrons and back scattered ones is their kinetic energy as the electrons with less than 50 eV are secondary electrons and all over the 50 eV are back scattered electrons. The difference in energies between SE and BSE is due to their birth processes as the SE are produced by inelastic scattering processes and BSE are just elastically scattered specimen. Mainly the SE1 and SE2 are used for imaging and the SE3 and BSE are then forming background noise for the measurement, but sometimes it's more convenient to examine the BSE due to the better contrast characteristics, enhanced topographical information and other qualification properties. The images taken with BSE, however, have worse overall resolution than SE. The electrons scattered from elsewhere than the sample (SE3) are always contributing as background noise. [130] In figure 3.16 is presented the ΣIGMA™ FESEM that was used in the measurements.

Figure 3.16 *A picture of the ΣIGMA™ FESEM. The image is adapted from [131].*

The main reason for using SEM rather than optical microscope is its superior precision. Where the resolving power of optical microscope is limited to 200 nm as its best a SEM can reach as low as 1 to 10 nm depending on the device and conditions. SEM also have a remarkable ability to picture 3D structures, which enables detailed characterization of surface morphology and textures. Imaging with SEM is also relatively fast and the only sample requirement is simply that at least the sample surface has to be conducting. [130]

Non-conducting samples, as all the dielectrics in this thesis, require a special attention to the sample preparation and measuring conditions, because they can be easily charged by the PE beam, which breaks the focus of incoming electrons. Most common way is to make the sample surface conducting by adding a conductive layer on top of it. This layer is usually a non-oxidizing metal deposited with sputtering, thermal evaporation or electron beam evaporation. In ideal case the conducting layer should be thin and uniform, so it would repeat the surface structure of the inspected sample. A good thickness of a conductive layer is about 10 nm before it starts to cover surface structures, but if this does not make the system conductive enough thicker layers must be grown. When adding a conducting overlayer is not an option, it is possible to examine the non-conducting samples with careful parametrization. Increasing the sweeping speed and lowering the acceleration voltage are effective ways to prevent sample charging. However the parametrization is a sample specific procedure and, in all, non-conducting samples are more challenging to picture than the conducting ones. [130]

In this thesis the samples were non-conductive dielectrics, so their imaging was

mainly done by coating them first with gold using EBE. The overlayer thicknesses varied from 10 to 100 nm as some samples were coated alongside other components. All the samples with same substances are covered with identical metal layer to minimize deviations between the samples of the same specimen class. Here is notable that imaging with SEM is similar to photography and the quality of the received images is greatly dependent on the operator. Thus the image quality comes hand in hand with experience in imaging and the writer humbly admits being a novice at that part.

3.2.4 Solar Cell Characterizations

Basis of the solar cell characterizations is to find out the cell's I-V behavior under sunlight illumination. As setting up the measurement tools and circuit connected solar cells outdoors and measuring them in variant conditions is rather unpractical and slow for quick characterizations many commercial and custom systems are built for this task. With a broadband light source and proper filters we can simulate the spectrum of the sun in different conditions (AM0, AM1.5D and AM1.5G). This illumination is usually normalized to 1000 W/m ^{2} irradiance and the temperature of the cell is maintained at 25 °C. In fig. 3.17 is illustrated the measurement circuit and presented the commercial Trisol™ Class AAA Standard Solar Simulator, that was used in I-V measurements of the test cells.

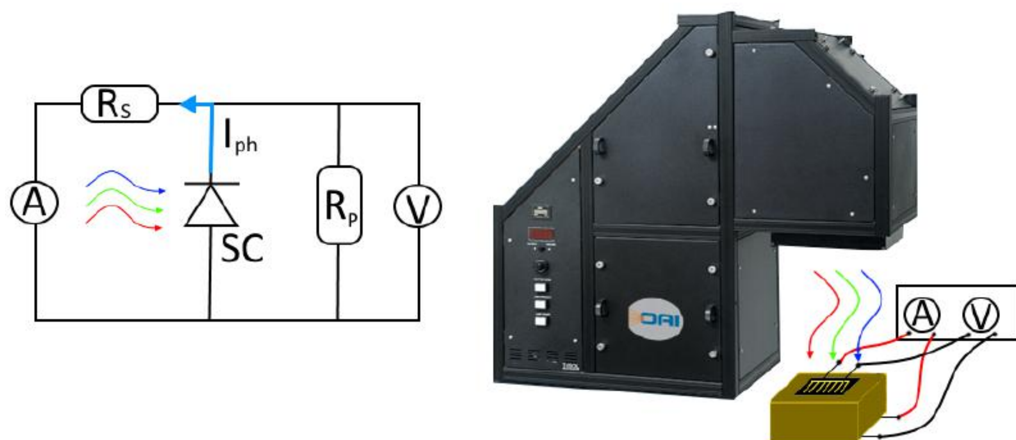

Figure 3.17 *Principle picture of solar cell IV-measurements. The figure is edited using references [12, 132].*

With this kind of solar simulator it's possible to measure the SC's efficiency η_{eff} eq. 2.74, open-circuit voltage V_{oc} eq. 2.72, short-circuit current I_{sc} eq. 2.75, short-circuit current density J_{sc}, fill factor FF eq. 2.73 and 2.76 and maximum power P_{max}. Along the EQE measurements it can be seen as the most important solar

cell characterization method. The gained I-V curve as in fig. 2.17 is usually more convenient to present as current density versus voltage curve, because this makes comparison between different sized cells possible. The I-V curve reveals if there are any additional loss mechanisms, such as current leakage, and gives a good tool for overall evaluation.

With I-V measurements it's also possible to find out the limiting current for each subcell of the MJSC structure. This is done by altering the illumination conditions. The used setup for this subcell current characterization was constructed by M.Sc Riku Isoaho and the principle of measurements and details of the setup are presented in his Master's thesis [133]. All the AR coated test cells were measured with this setup to find out how the coatings affected to the different bandwidths according to the subcells.

As the focus of this thesis is at the AR coatings and their overall functionalities, the solar cells' I-V behaviors were mainly inspected with the AM1.5D spectrum to get comparable data and to see whether the designs function at all. The triple-junction MJSCs of InGaP/GaAs/GaInNAsSb that were used as test cells are designed and optimized for space applications so the real potential of the cells will not be shown in the results, as this requires measurements with AM0 and AR optimization according to the subcell current matching. The I-V curves, however, give the differences between the cells with different AR coatings and the reflectance curves reveal the coatings' properties over the entire solar bandwidth.

4. Material Characteristics and Coating Analysis

The aim of this study is to characterize the optical and physical properties of electron beam evaporated MgF_2 thin films, SiO_2 nanoporous films manufactured with PECVD, and commercial products SC501K and SC800i prepared with spinning method as components of an AR coating. With the found material parameters we try to construct effective anti-reflective layers for MJSC in question by using MgF_2 and TiO_2 double layer, nanoporous SiO_2 with TiO_2, the spinnable thin film SC501K as a double layer structure with TiO_2 and lastly a triple layer coating consisting of MgF_2, Al_2O_3 and TiO_2. Mainly the characterized materials act as the low index layer of the coating and TiO_2 functions as the high index layer, whereas the Al_2O_3 is a medium index layer between these two.

4.1 Thin Film Characterizations

As the material study of EBE deposited MgF_2, PECVD manufactured SiO_2 and commercial spinnable siloxanes SC510K and SC800i aimed at their usage in AR coatings and finding promising deposition parameters for that purpose, a series of different characterization methods were used to evaluate the results. Next sections cover the results of the material and deposition studies of these thin films.

4.1.1 Characterization of MgF_2 Thin Films

In this study we evaporated MgF_2 with EBE on a silicon wafer. The silicon substrates were not specially prepared before the evaporation, but they had been stored in constant environment, where the room temperature and humidity are stabilized to the values of 22 °C and 44 %. The evaporation process is presented in section 3.1.1 The main interest for MgF_2 films focuses on its properties as an AR low refractive layer, so all the optical and physical properties are inspected from that point of view. The thickness for the MgF_2 films was aimed to be 100 nm after the deposition, but manual controllers of the current, temperature, voltage and partially pressure

The samples were identified with ID parameters, that are shown in table 4.1. They are divided in two main groups, where the first series include samples deposited in different substrate temperatures T_s and the second has the growth rate as the changing variable at the substrate temperature $T_s = 200\,°C$. More inclusive identification of the different samples are included in table A.1.

Table 4.1 *Th MgF_2 samples and their inspected growth related variable.*

Sample ID	Substance	Variable	Value
S1	MgF_2	Substrate Temperature ($°C$)	50
S2	MgF_2	Substrate Temperature ($°C$)	100
S3	MgF_2	Substrate Temperature ($°C$)	150
S4	MgF_2	Substrate Temperature ($°C$)	200
S5	MgF_2	Substrate Temperature ($°C$)	240
S6	MgF_2	Growth Rate (nm/s)	0.1
S4	MgF_2	Growth Rate (nm/s)	0.3
S7	MgF_2	Growth Rate (nm/s)	0.5

As we are interested in the optical and physical qualities of the prepared films the simplest and quickest way of getting relative information about the samples was to measure the refractive index and film thickness with monochromatic ellipsometer. The gathered data from several MgF_2 depositions are presented in fig. 4.1 and surprisingly the refractive index seems to lower as the substrate temperature grows. It would be presumable that with higher temperature the film density would grow and thus the refractive index would also rise. However a study made by Yu et al in 2007 [64] and other studies [63, 65] show that the MgF_2 crystallizes completely somewhere around 240-250 °C and before that its nature is partially amorphous. This leads indistinct grain boundaries and fewer interspaces, which means comparative compactness and thus higher refractive index. It explains why the refractive index decreases as the temperature increases until the MgF_2 is entirely crystallized. The reference studies [50, 64] also indicate that when deposited in higher temperatures than 250 °C the refractive index begins to grow as the packing density of the crystallized structure gets denser.

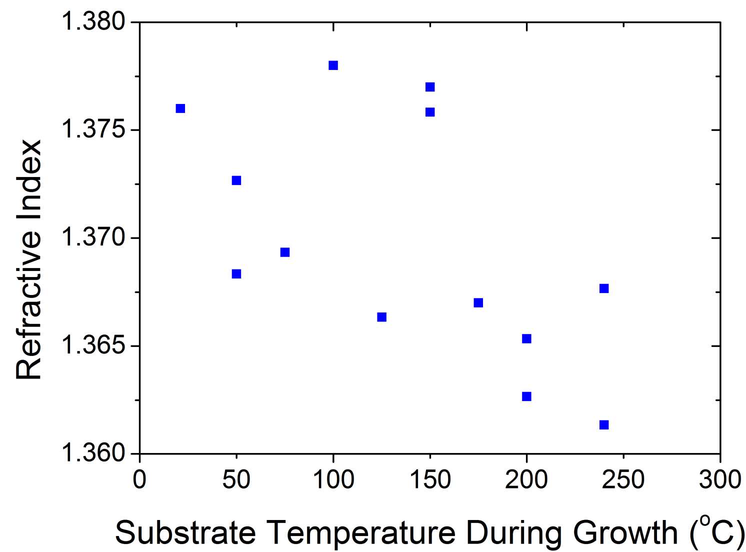

Figure 4.1 *The refractive indices of MgF_2 samples acquired in different depositions with different substrate temperatures.*

As the MgF_2 is known to be columnar and porous until it reaches packing density of 1, over $T_s = 250\,°C$ deposited films, it is presumable that being exposed to room air conditions raises the refractive indices of the films, as the structure absorbs water vapor. This effect was studied by comparing the measured refractive indices of the films right after deposition, after two weeks of exposion to room air and after resting the two weeks old films a 24 hours in water and measuring their refractive indices after they were taken out from the water. The results are shown in fig. 4.2, and the effects to the film thicknesses are presented in fig. 4.3.

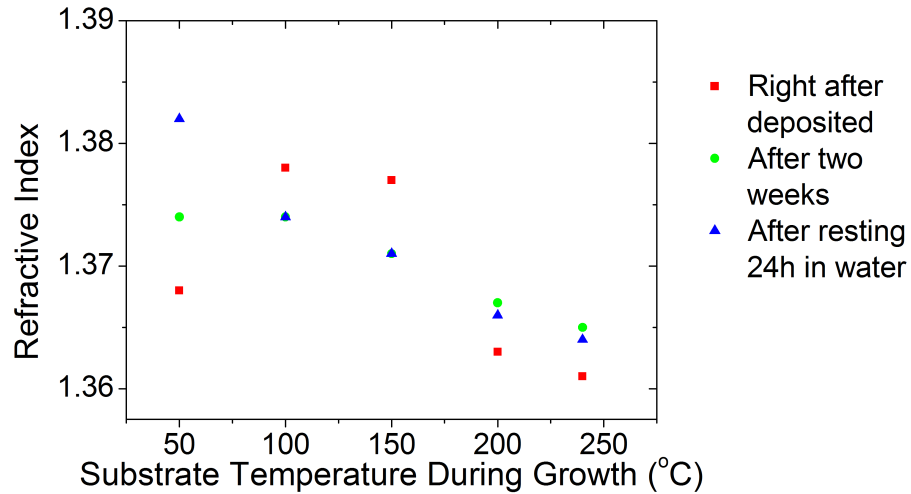

Figure 4.2 *Refractive indices of* MgF_2 *samples S1-S5 right after deposition and after aging in room air and water.*

It can clearly be seen that right after deposition measured values do not follow any clear trend, but after setting down for two weeks the indices are ordered in linearly decreasing trend. The water resting values do not significantly differ from the just aged samples, except for the lowest deposition temperature, for which the water clearly raises the refractive index, because its porosity most likely is larger than of the other films.

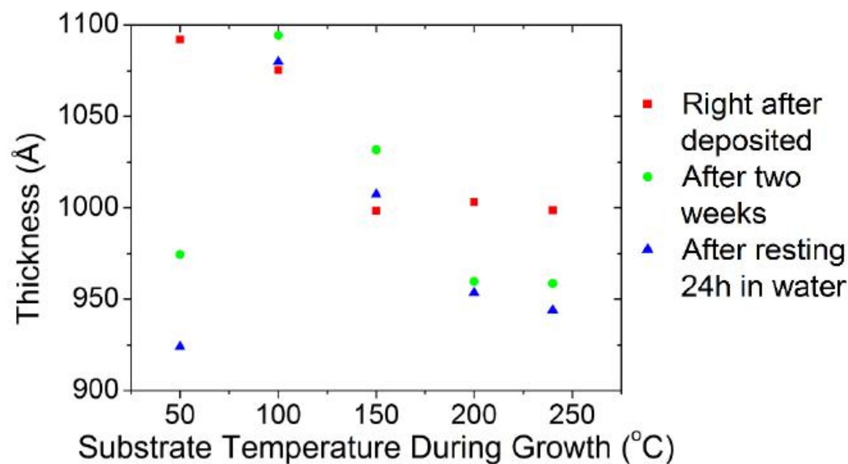

Figure 4.3 *Thicknesses of* MgF_2 *samples S1-S5 right after deposition and after aging in room air and water.*

For the samples S1, S4 and S5 the thicknesses decrease after time and water and for samples S2 and S3 the thickness has a slight increase. Likely explanation is that the S1 is so porous that the water gets well within the structure and pulls the film

more denser form. The samples S2 and S3 are presumably less porous than S1 and their structure is still mainly amorphous, thus the air and water cannot as much affect the film structure as for S1. For the more crystallized S4 and S5 the principle is same than for porous S1 but not as strongly affecting. For all the samples the water resting lowered the film thickness compared to the in air aged film's value. The comparison reveals, that for film design that is meant for atmospheric conditions, it is better to use values defined after two weeks of room air exposure. In the case of space environment design the right after deposition measured values are more reliable, as the water sorption is proven to be a reversible process [50].

Due to this trend of increasing packing density, crystallization and lowering refractive index it seems recommendable that MgF_2 is deposited at higher temperatures than the previously used AR coating of SiO_2/TiO_2 that is deposited in 100 °C. In this thesis the chosen value was 200 °C for T_s, as was recommended by the supplier of the MgF_2 grains [134]. As much clarity was not obtained with the deposition rate examination, as the results in fig. 4.4 are not so straightforwardly intrepretated.

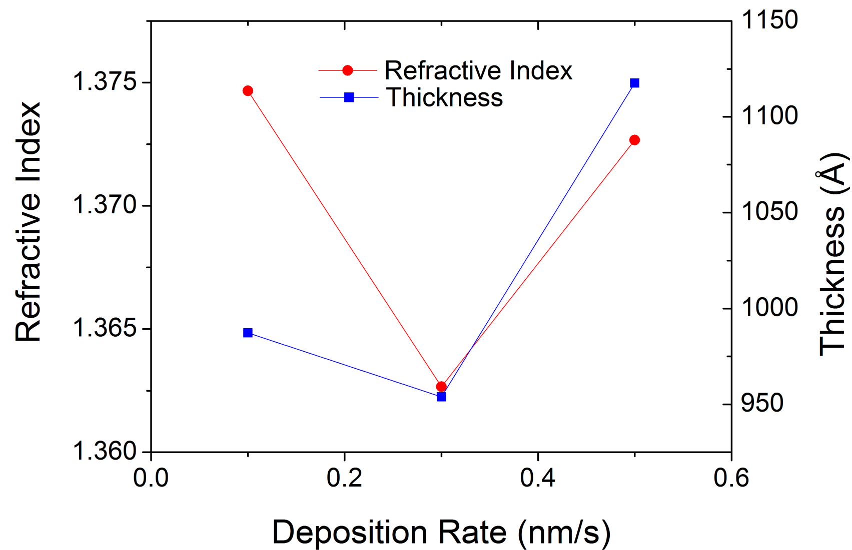

Figure 4.4 *Examination of the deposition rate's influence to the refractive index of MgF_2. The thickness variation of the samples is also presented.*

As the graph 4.4 shows, the effect of changing rate deposition to refractive index and film thickness values is not following any trend, it's hard to make any firm conclusions. As the temperature change series was done first, which includes the rate 0.3 nm/s inspected here, and after that the crucible for MgF_2 was refilled, the rate changes between 0.3 nm/s and the other two may have changes that are due to the refilling. According to the acquired values, however, the rate 0.3 nm/s showed the best performance, so we stack to that in the following depositions for the AR

coatings.

To define the surface roughness and structural layout we used AFM measurements. The AFM measurement draws a topographical surface map from each measurement and for S1–S5 these are presented in fig. B.1. The numerical data retrieved from the samples S1–S5 is presented in table B.1. The surface roughness affects to the scattering from the film surface, so for AR coating we want to have as low values for $rmsr$, ra and $< a >$ as possible. In fig. 4.5 all three are presented for the samples S1–S5.

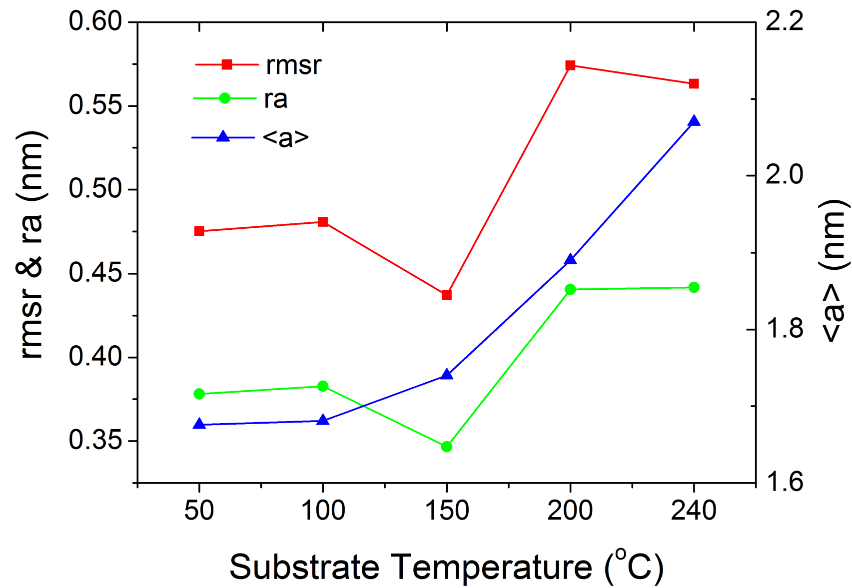

Figure 4.5 *The AFM results for the temperature series of* MgF_2.

The indicators for surface roughness are all very small for every film of the samples S1–S5. As the temperature increases the average height $< a >$ is steadily increasing as are the $rmsr$ and ra. Notable change can be seen for sample S3, as it has the lowest values for $rmsr$ and ra of all the samples. This would indicate that its surface has the smoothest structure and thus it scatters less light than the other films. For inclusive examination the surface topology maps for samples S1–S5 are presented in fig. B.1. Also the rate series samples roughness were measured, but since the trendless variation of values does not bring any further insight the topographical mappings are only left to the appendix B in fig. B.2 and the analysis results can be found in table B.2. The roughness difference should also be somewhat notable in the reflectance measurements of the films, although usage of the URA module lessens the measured scattering effects. This difference in surface roughness is partly in contravention of the refractive index and film structure results, so it's considerable whether it would be suffice to use deposition temperature of 150 °C instead of 200

°C. In this thesis, however, the chosen temperature for AR coatings is 200 °C.

The adhesion of a film and a substrate is defined as the force which these two are bound together. There are several different ways of measuring adherence of the film such as scotch-tape test, abrasion test, direct pull-off method, scratch test, X-ray diffraction test and capacity test. The different tests can be divided to mechanical and non-mechanical methods and also to qualitative and quantitative methods. [117] In this thesis only qualitative scotch-tape and scratch tests are used to compare the adhesion of different films.

The adhesion tests for the MgF_2 films prepared in different substrate temperatures were made with standardized scotch tape and metal tweezers were used to scratch the surfaces. Only little damage could be observed with bare eyes as can be seen in fig. 4.6, as only the scratch in S1 is clearly visible.

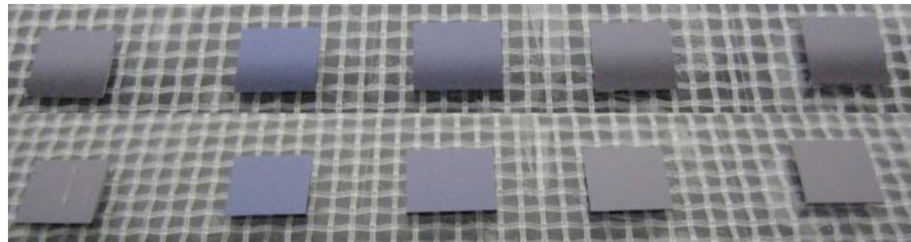

Figure 4.6 *A photo taken with normal digital camera of the adhesion test results. Upper row is before the tape test and scratching and lower after the tests were done. From left to right the samples are S1, S2, S3, S4 and S5.*

Some of the scotch tape results examined by optical microscope are shown in fig. 4.7. The damage to the surfaces after the scotch tape test was minimal and only some defects were noticed after microscopic evaluation. The sample S1 shows a clear rip off pattern caused by the tape as does the sample S3. The sample S5 however shows only some lost spots of coverage and in all samples none of the damage was visible to bare eyes. The white markings on the surfaces are glue from the tape.

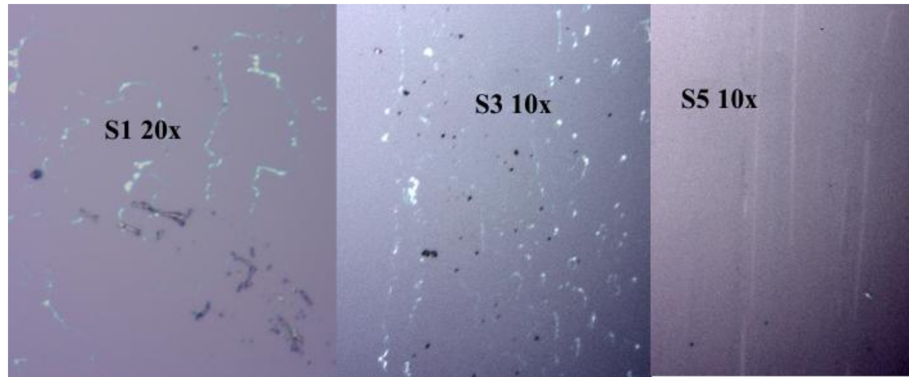

Figure 4.7 *The scotch tape test results for samples S1, S3 and S5. The magnification level is marked next to the sample IDs. The vertical lines in S5 are caused by the scratch test.*

In the scratch test the scratching was done with two different force impact in a manner where the lighter scratch was scraped first a bit afar from the wafers edge and the harder scratch more in the center. The scratch was done with several strokes. Notable result was that only the film that was prepared with 50 °C substrate temperature showed considerable damage after scratching. The scratches were seen also in other four MgF_2 films, but the depth of the scrapes decreased as the substrate temperature of evaporation rose. Some of the results gained with the optical microscope are given in fig. 4.8. All in all the mechanical durability of MgF_2 films deposited with EBE was proven to be excellent as many references suggest [49–51].

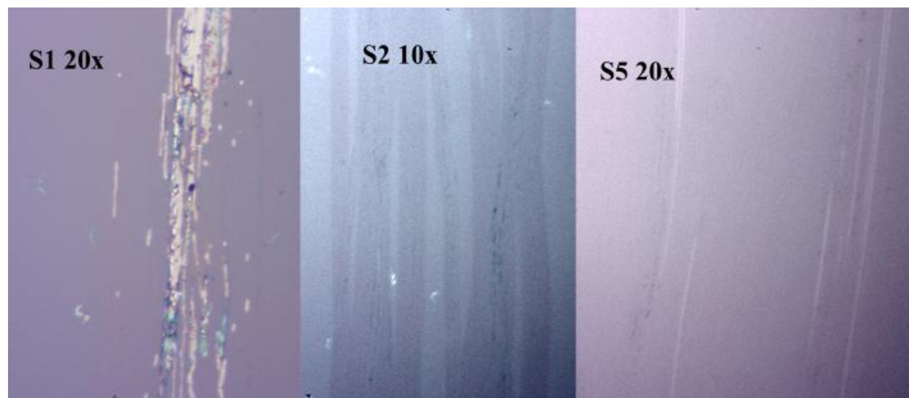

Figure 4.8 *Scratch test results for samples S1, S2 and S5.*

The adhesion tests showed that from the point of mechanical durability only the sample S1 was not suitable for realiable coating applications. This was due to its low adhesion and abrasion resistance, as its structure would most likely be affected by environmental changes, thus altering its designed properties and possibly damaging it beyond functionality.

To extent the study, the samples were annealed one minute in vacuum and the temperatures were changed in hundred celsius degrees intervals from 400 to 1000 °C.

The results are presented in fig. 4.9.

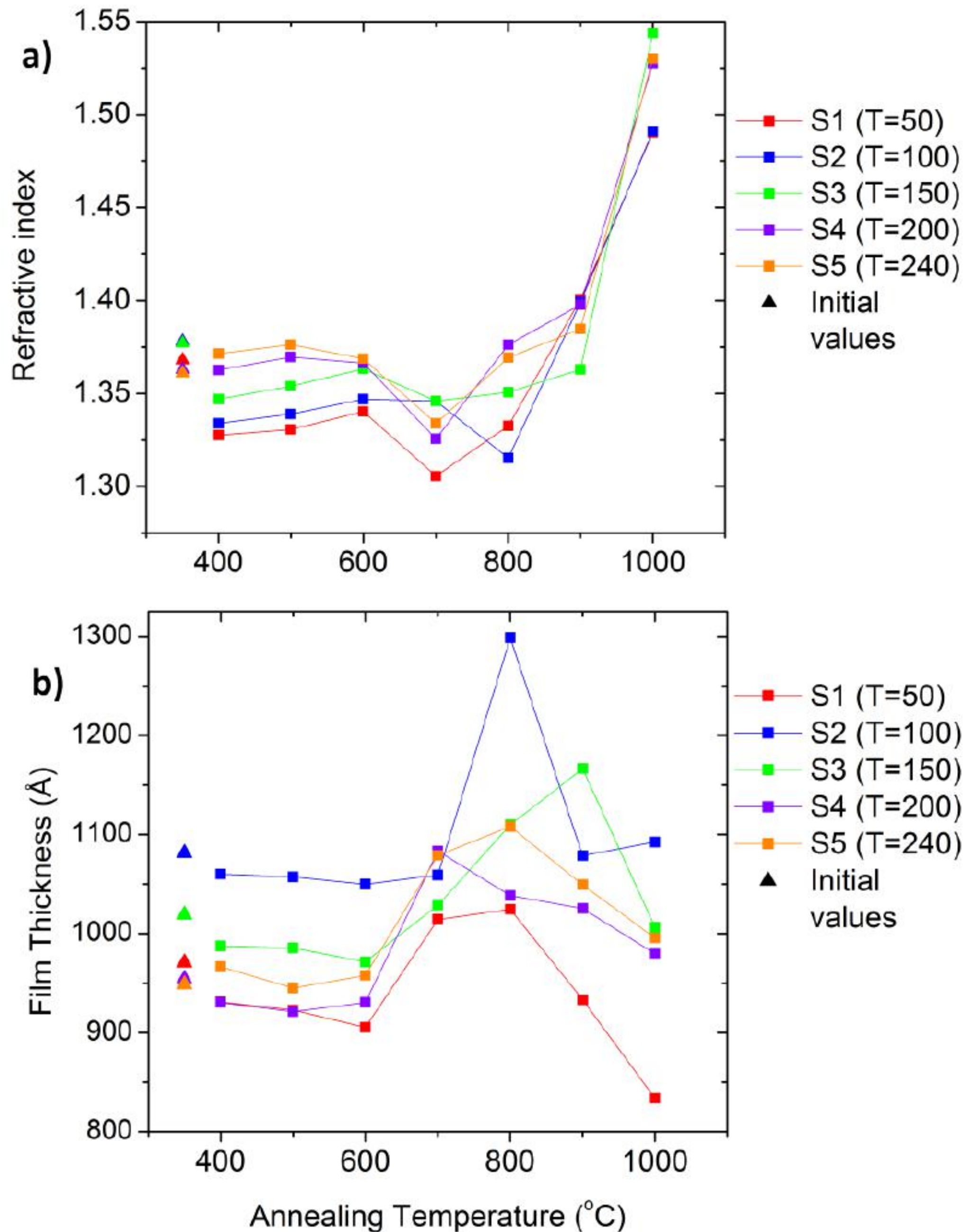

Figure 4.9 *Annealing effects of the MgF_2 films. The upper graph a) presents the refractive index variations after annealing and the graph b) shows similarly the thickness variations of the same samples. The initial values of refractive indices and thicknesses of the films are marked with triangles.*

The annealing seems to lower the refractive indices of the samples S1–S3 that where originally deposited at lower temperatures. With samples S4 and S5 there is not such impact and the refractive indices remain essentially the same. It can be

seen that at the temperature 700 °C there is a clear structural change, as the film thicknesses suddenly increases before decreasing rapidly after temperature of 800 °C. Also at this cross-point the refractive indices decrease considerably, before they start to grow substantially. It would seem that at the temperature 700 °C the lattice structure of the films change to denser form and after that temperature the trend is clear, as the rising refractive indices and lowering film thicknesses suggest that the packing density increases and thus the MgF_2 films become optically denser as well. One possibility is that at this annealing temperature, the partially amorphous films crystallize and this would lead to this structural evolution. Confirming this, however, would require X-ray diffractometry that is not included in this thesis. With the results at hand it would seem worthwhile to try annealing MgF_2 films at 700 °C to change their film properties, but for AR coatings this would require similar study for the high index material as well, which was not included here, and the actual solar cells would deteriorate in functionality at that high temperatures. For AFM measurements the annealed specimen of the sample S4 were chosen for closer examination, as S4 represents the conditions that will be used in the AR coating fabrications. A good overview of roughness changes can be seen in fig. 4.10.

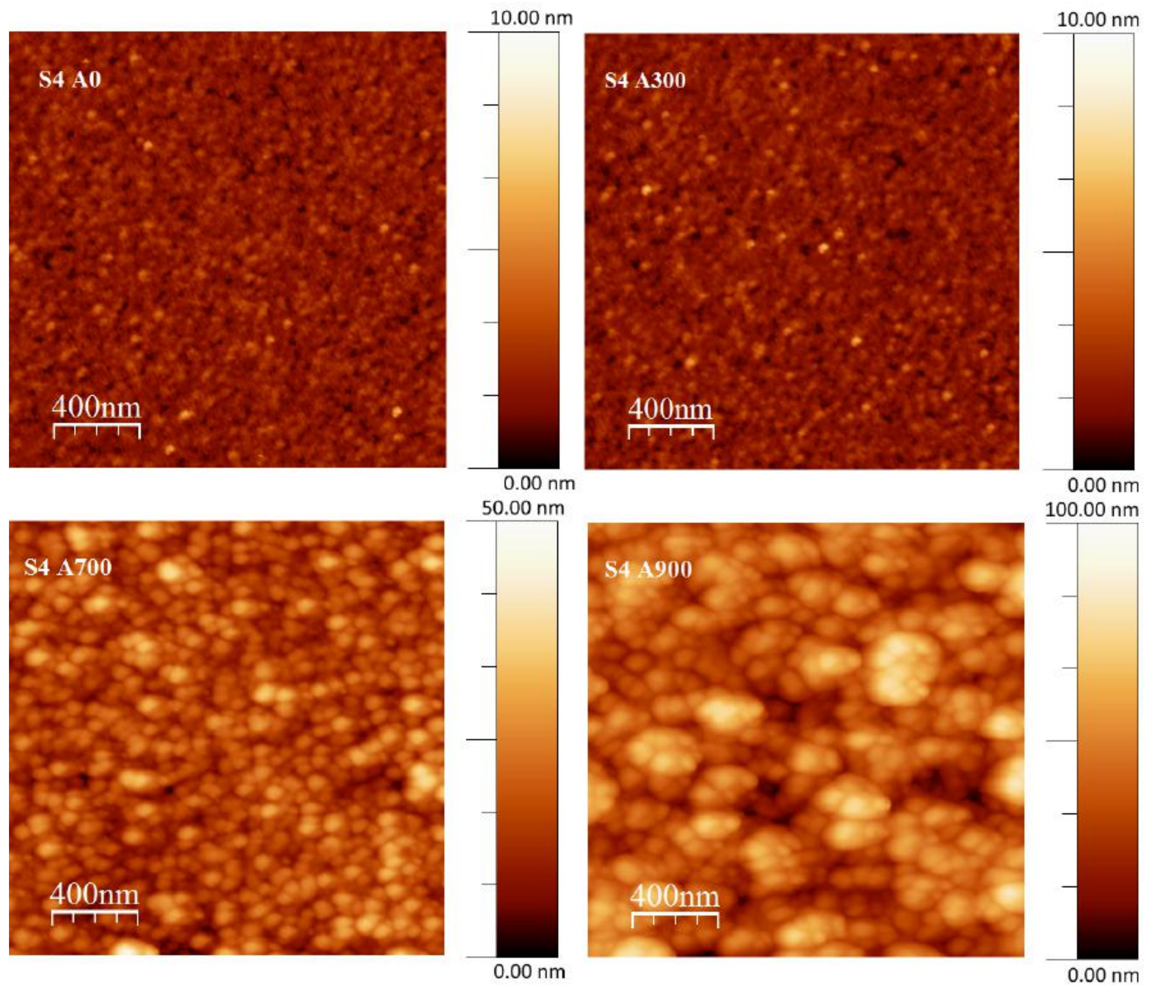

Figure 4.10 *AFM pictures for annealing series done to S4 (T=200). The annealing temperature is marked next to the sample ID. A0 marks no annealing and the rest reads as 'A' for annealing and the number states the temperature used as in °C.*

One can see that as the annealing temperature rises the surface roughness increases. The MgF_2 seems to form bigger clusters as the temperature grows and thus loses its smooth surface structure. The changes are rather small near the deposition temperature as between samples S4 A0 and S4 A300, where the *rmsr* of the samples differ only 0.0126 nm. The *rmsr* difference between the samples S4 A0 and S4 A900, however, is 12.937 nm, so the roughening increases as the temperature deviates from the initial deposition temperature. Inclusive numerical data for the measurements are tabled in table B.3.

The SEM imaging done to the sample series S1–S5 revealed good adhesion between MgF_2 film and the silicon substrate, as where the gold had started to withdraw from the MgF_2 surface, the layer bonding between MgF_2 and the substrate was still intact. A good example of this difference is presented in the figure 4.11.

The image is colored with GIMP and the overlaying gold can be seen up lifted from the MgF_2 surface as the MgF_2 layer is still uniformly attached to the silicon substrate.

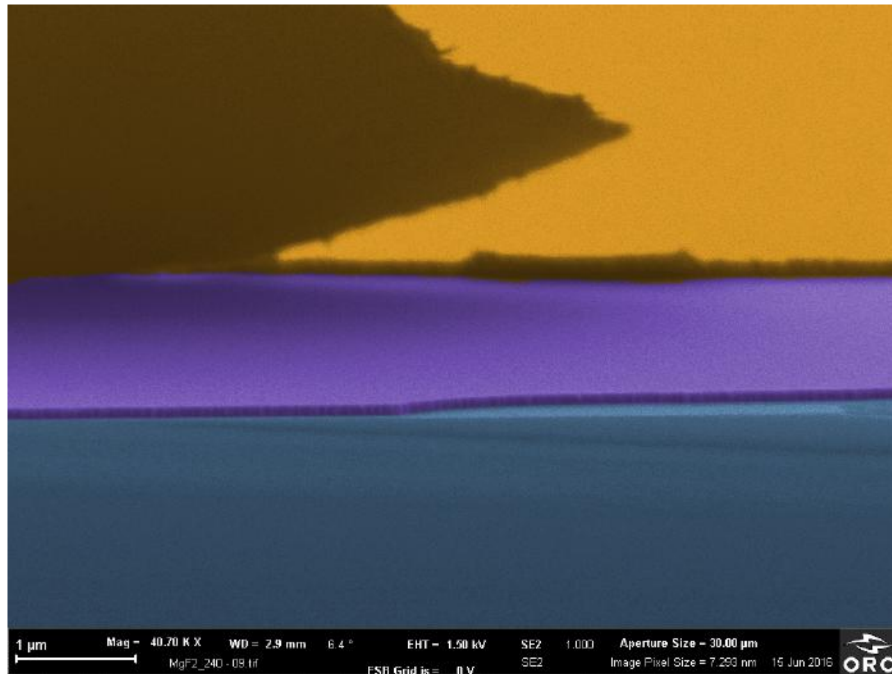

Figure 4.11 *SEM image of MgF_2 film deposited at 240 °C on a silicon substrate and covered with NiAu overlayer for imaging.*

All in all the SEM imaging of MgF_2 proved to be challenging as the dielectric nature of the films required a conductive overlayer, that was EBE deposited gold with some nickel between the dielectric and the gold layers. The samples were coated alongside with other components, so the surface imaging was neglected as the 100 nm thick metal layer covered most of the surface structures. The cross-sectional imaging, however, worked out fairly well and a couple of such images is shown in fig. 4.12.

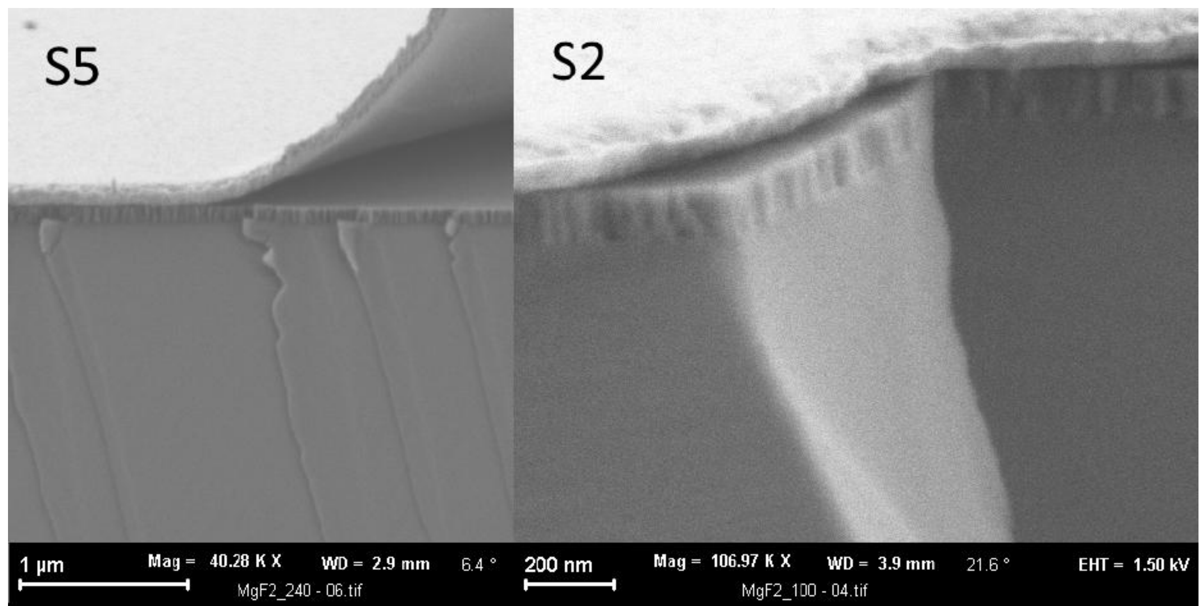

Figure 4.12 *A cross-sectional SEM image of the MgF_2 samples S5 and S2.*

From these images it can be seen that the films at either end of the sample series has the columnar pore structure, as was presented in the overview in the section 2.2.1 Both films also show the smooth surface structure that was proven with AFM measurements.

The characterizations included measuring the reflectances of the samples, that was done with spectrophotometer, to find out differences or structural defects causing irregularities in the films' behavior. The results are presented in fig. 4.13.

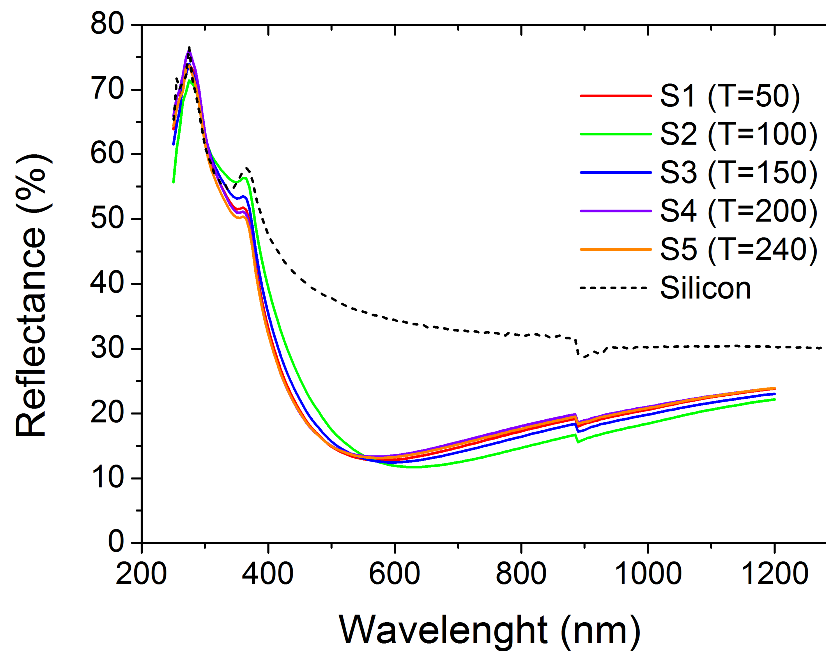

Figure 4.13 *The reflectance profiles for the MgF_2 test series S1-S5 measured with PerkinElmer spectrophotometer.*

The curves are very similar, but the S2 has a bit shifted reflectance from the other samples. This, however, can be explained by the thickness difference of the sample S2 when compared to others, as shown in fig. 4.2. Other notable thing is the lowest reflectance of S3, when excluding S2, that was predicted by the AFM measurements. Due to the possibly smoother surface, the film deposited at 150 °C might after all be more convenient choice for the AR structures than the chosen 200 °C, which must be noted in further designs and testing.

Lastly there are the ellipsometric measurements performed with VASE, that are crucial for the AR design. These dispersion curves are the basis of the modeling and calculations, done with the Essential Macleod program. As MgF_2 was the main interest for the lower index material, all the samples S1–S5 were measured with VASE and the results are shown in fig. 4.14. There are also few literature reference

curves from Dodge [48], Li [123] and Sopra [124].

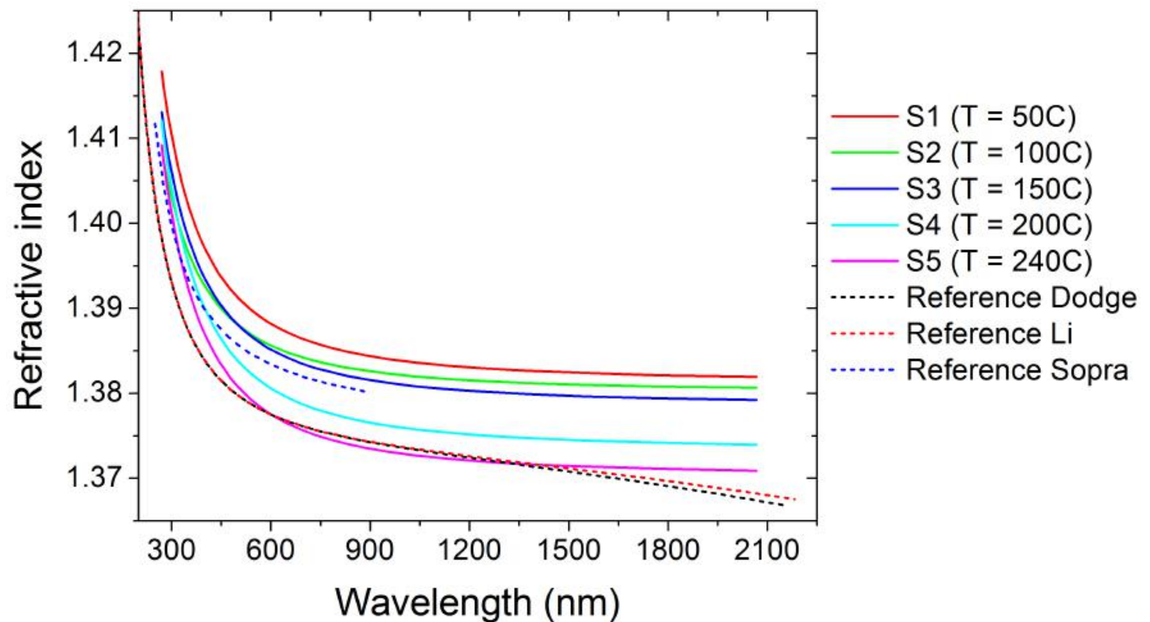

Figure 4.14 *The dispersion curves for MgF_2 measured with VASE.*

The curves follow each others accordingly to the monochromatic ellipsometer measurements. The biggest difference is between 150 °C and 200 °C, which is partially why the 200 °C was chosen to be the final deposition temperature. The 240 °C deposited sample is closest to the references, as its structure closes to the bulk structure of MgF_2.

As a conclusion of MgF_2 characterizations, the substance seems very suitable to lower index layer material for AR coatings, as it's mechanically durable and the refractive index is low enough and stable after a time. The main question remains whether the deposition temperature needs to be 200 °C or would the 150 °C be more suitable. In this thesis the previous was chosen for its better mechanical durability and lower refractive index profile.

4.1.2 Characterization of SiO_2 Nanoporous Films

The SiO_2 thin films were grown with PECVD method that is presented in the section 3.1.2. Every sample film was aimed to be 100 nm thick after deposition, but natural deviation occurs due so many variables affecting the final result. The goal was to lower the refractive index of the silica by increasing its structural porosity. This was done by decreasing the growth temperature and increasing the NO_2:SiH_4 gas ratio by reducing the SiH_4 gas flow. The growth parameters are presented in table A.2 and the main sample division in table 4.2.

Table 4.2 *The SiO_2 samples and their inspected growth related variable.*

Sample ID	Substance	Variable	Value
S9	SiO_2	Substrate Temperature (°C)	50
S10	SiO_2	Substrate Temperature (°C)	100
S11	SiO_2	Substrate Temperature (°C)	200
S12	SiO_2	Substrate Temperature (°C)	300
S10	SiO_2	Gas Ratio (sccm)	425
S13	SiO_2	Gas Ratio (sccm)	325
S14	SiO_2	Gas Ratio (sccm)	225
S15	SiO_2	Gas Ratio (sccm)	125
S16	SiO_2	Gas Ratio (sccm)	100
S17	SiO_2	Gas Ratio (sccm)	25

Similarly than with MgF_2 the SiO_2 was first characterized with monochromatic ellipsometer to find out the refractive indices and the film thicknesses of different samples. The aging time of two weeks and the water test were also applied to the SiO_2 films. The results for refractive indices of the temperature controlled samples (S9–S12) are presented in fig. 4.15 and for the thicknesses in fig. 4.16.

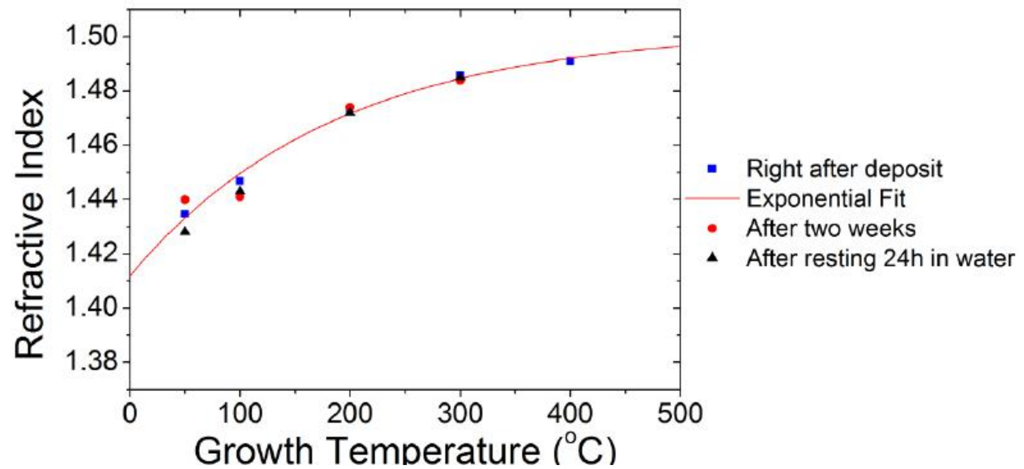

Figure 4.15 *The SiO_2 samples deposited in different temperatures and how their refractive indices and thicknesses change after time and water exposure.*

The refractive index seems to decrease hand in hand with the temperature and the trend fits to an exponential curve. The aging and water do not have as big influence than with MgF_2, but as the deposition temperature decreases the effects become more clear. This is likely due to increasing porosity, which has been caused by the lower deposition temperature.

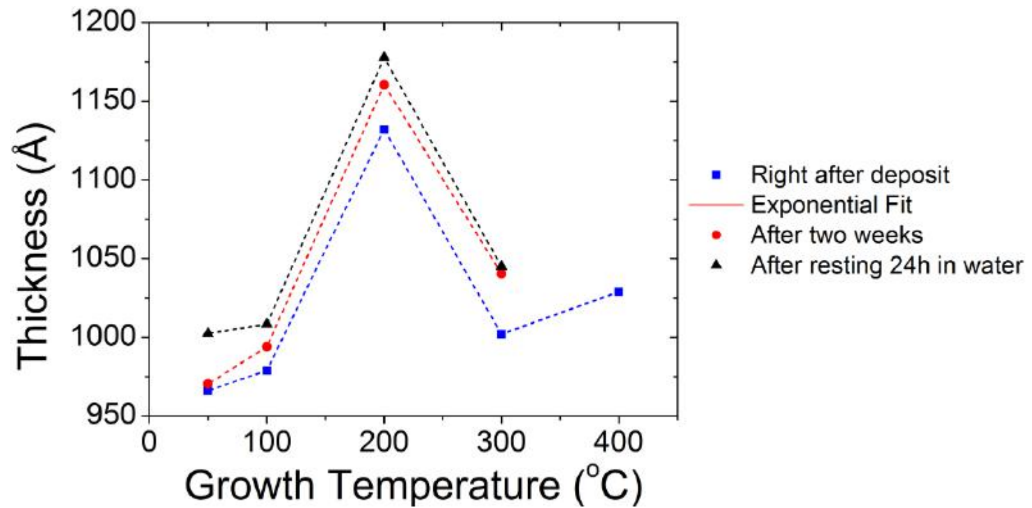

Figure 4.16 *The SiO_2 samples deposited in different temperatures and how their thicknesses change after time and water exposure.*

The thicknesses seem to grow few nanometers after a time and exposure to water swell the structures a bit more. When designing a layer structure, where the layer thicknesses have a crucial role for the film's functionality it would be recommendable to include these thickness changes into the design so that the film does not lose its optimal properties due structural deviations.

From the growth temperature series the temperature 100 °C was chosen to be the test condition for the flow rate series, where the gas flow of SiH_4 was reduced. The monochromatic ellipsometer measurement results for the refractive indices of the flow rate series are shown in fig. 4.17 for SiO_2 samples S10 and S13–S17. As with the magnesium fluoride and SiO_2 temperature series samples, also the flow rate series had re-measurements after two weeks exposure to room air and 24 hours in water.

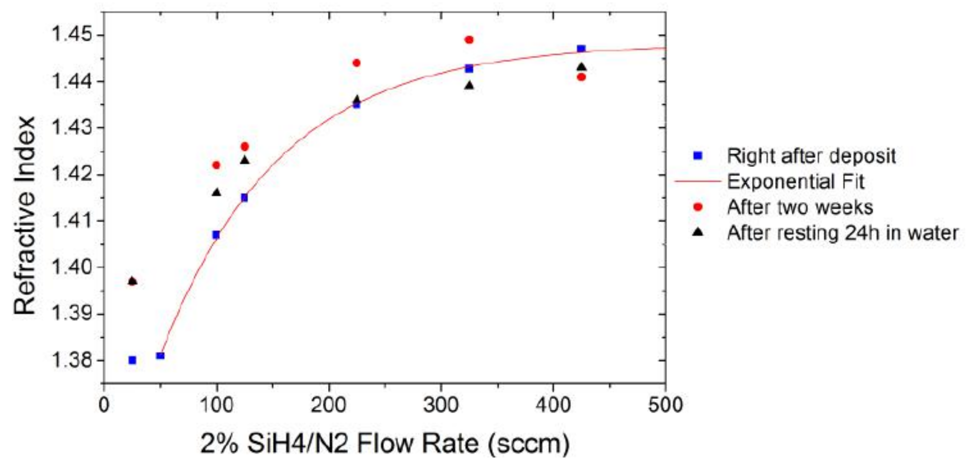

Figure 4.17 *The measured refractive indices of the* SiO_2 *flowrate series (S10, S13-S17) and their change after time and water exposure.*

The refractive index of SiO_2 seems to decrease as the flow of SiH_4 is reduced. This can partly be explained by the increased oxygen proportion in SiO_2 as the extend amount of NO_2 alters the molecular ratio of Si and O. Another presumption is that the structure of SiO_2 becomes more porous and the air content within the pores reduces the effective refractive index. There is some noticeable aging effects in the refractive indices as they seem to increase a bit after time, which probably is caused by absorbed humidity from the air. The corresponding thickness changes are shown in fig. 4.18.

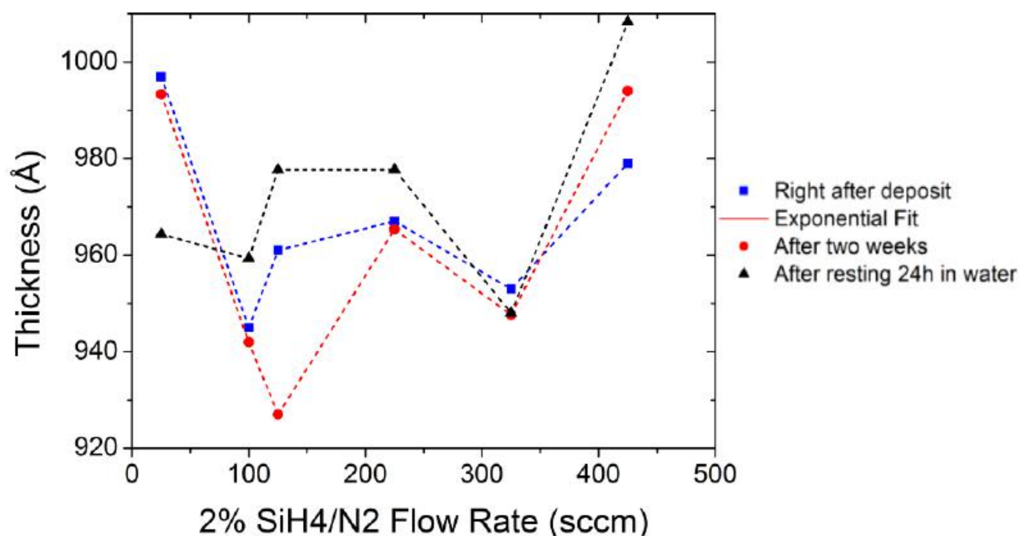

Figure 4.18 *The measured film thicknesses of the* SiO_2 *flowrate series (S10, S13-S17) and their change after time and water exposure.*

Unlike with the temperature series, the thickness variations over time and water exposure do not seem to have any clear trend to base assumption on. The thickness variations within a single film stay under 5 nm so big fluctuations of layer thicknesses are not presumable.

The same adhesion and abrasion tests were done to SiO_2 samples than to the MgF_2 films, namely the scotchtape test and scratching. In fig. 4.19 is presented some of the tape samples with the magnification of the microscope written next to the sample ID.

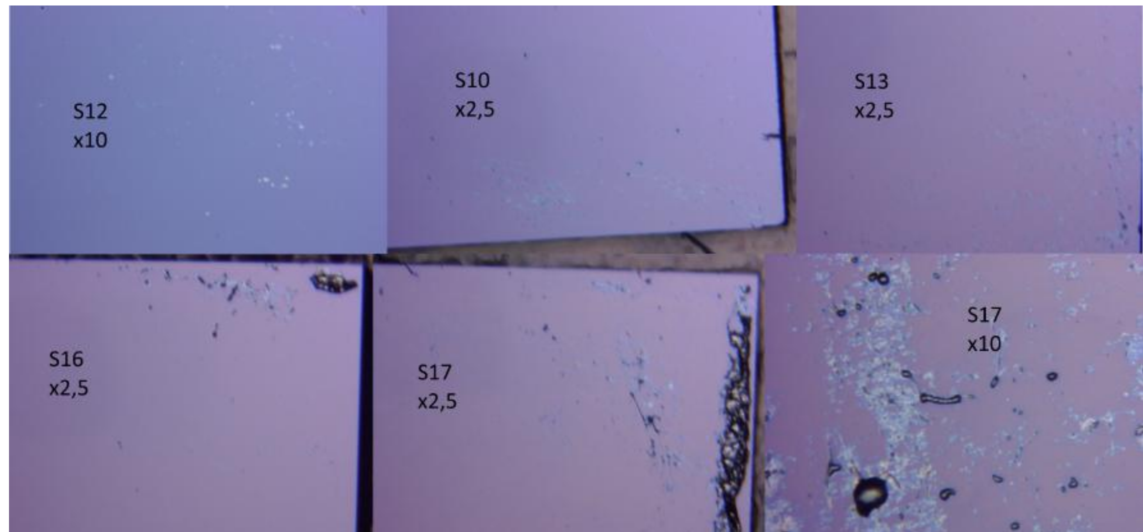

Figure 4.19 *The Scotch tape test results comparison for SiO_2 samples.*

SiO_2 has similar properties as MgF_2 what comes to mechanical durability, when the deposition conditions are regular. As the substrate temperature decreases so does the adhesion. When added the varied flow ratio the porousness makes the layer even more prone to peeling as can be seen in figure's 4.19 pictures of sample S17, where the edges have large stripes off peeled film and in the middle of the wafer there are lots of defects in the film caused by the tape test. The scratching results are shown in fig. 4.20 and this brings up some differences when compared to MgF_2.

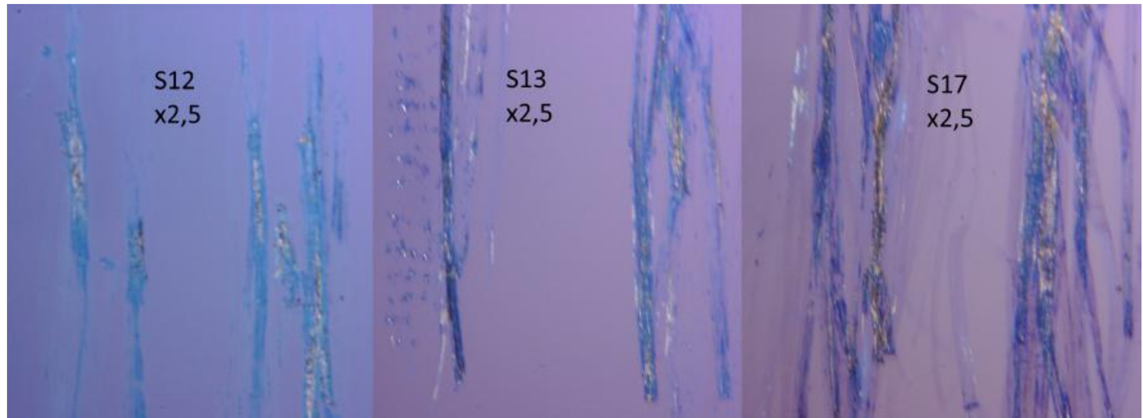

Figure 4.20 *The scratch test results for SiO_2 samples S12, S13 and S17.*

Even the higher index regularly deposited SiO_2 (sample S12) shows quite clear scratch marks, that the MgF_2 samples deposited over 100 °C temperature did not show. This would indicate that MgF_2 has a higher abrasion resistance than SiO_2. The sample S17 shows very clear scratch stripes, so when considering its usage on coating applications, this mechanical limitation must be taken into account, as wearing environment could damage the film and change its properties.

To find out whether our SiO_2 samples has in reality assumed porous structure, some of the samples were imaged with SEM. The opposite heads of the sample series were chosen to be imaged to get a clear vision on differences. The surface structure of SiO_2 deposited at 300 °C with the usual flow ratio is presented on the left and the lowest refractive index material of our SiO_2 samples is on the right in figure 4.21.

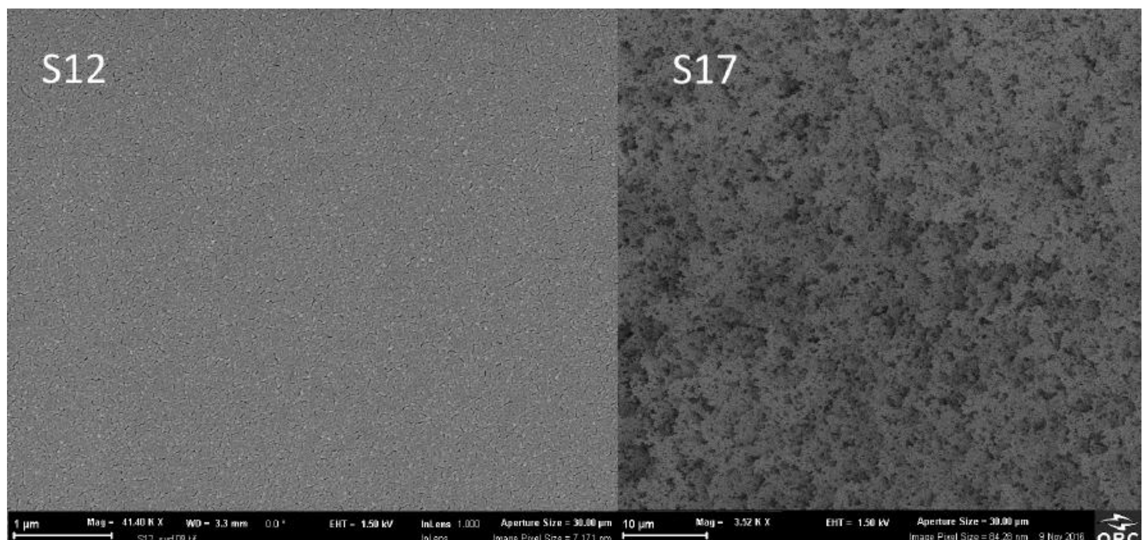

Figure 4.21 *Comparison between the surfaces of regular PECVD deposited SiO_2 and nanoporous SiO_2.*

The granular pattern shown on the surface of S12 is not caused by the SiO_2 surface structure, which is practically a smooth layer, but by the nanoclustered gold that was deposited on the sample surfaces to increase conductivity. [135] As the layer was only 10 nm thick, the gold formed cluster like structures with stripes that separate them. The metal layer is, however, uniformly distributed and eases the SEM imaging. By comparing these two extremes of the SiO_2 series, it is presumable that the lower temperature and the altered flow ratio are together increasing the porosity of SiO_2. Additional imaging and further testing would be in order to find out more of the contribution of each variable.

When taking the porous sample S17 under closer examination, the different sized pores reveal a quite variable structure, that is presented in fig. 4.22. It would seem that the main structure is constructed by a flake like sub-surfaces, which are filled with holes of many sizes. The pore size varies approximately from less than 100 nm to over a couple micrometers.

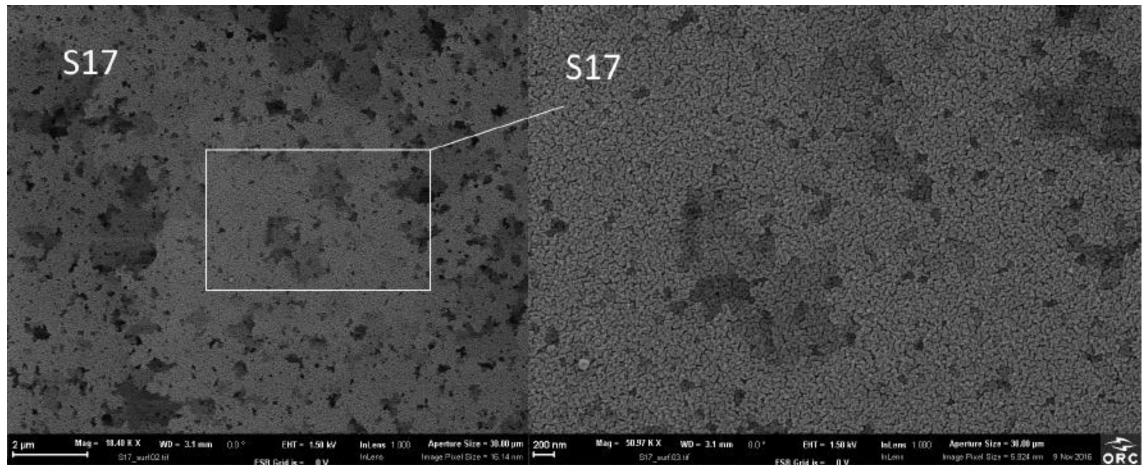

Figure 4.22 *A surface image of the nanoporous SiO_2, where the coral like structure is clearly visible.*

It is presumable that the porousness lowers the refractive index of SiO_2 as now the thin film is partially filled with air, which has refractive index close to 1. As with the smooth S12, also the S17 image shows the granular gold overlayer.

As MgF_2 is the topmost layer of some of our AR coating designs, so is the SiO_2. For the top layer another important factor beside refractive index is the surface roughness, as rougher surfaces scatter more light. To reduce the amount of scattering, we want to have as smooth surfaces as possible. In fig. 4.23 is presented the roughness values of the films according to their growth temperature.

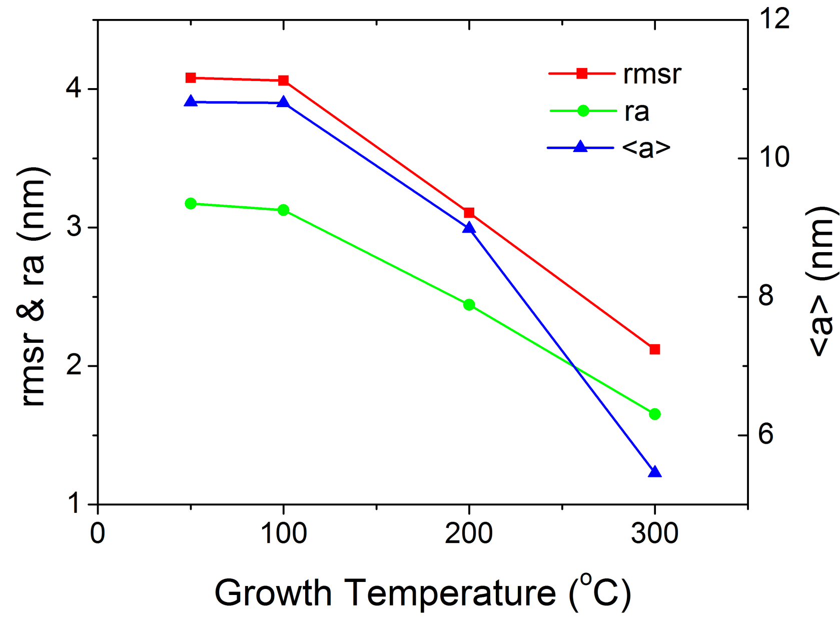

Figure 4.23 *AFM roughness measurement data of SiO_2 samples S9-S12, where the substrate temperature was the varied value.*

The trend with SiO_2 seems to be that the higher the growth temperature the smoother the surface. It would seem logical that as the porosity increases, so does the surface roughness. The actual height distribution maps can be found in fig. B.3 and the inclusive numerical data for roughness evaluation is shown in table B.4. In the fig. 4.24 is presented the same roughness analysis to the flow rate series. For them the surface topology maps are shown in fig. B.4 and the numerical results in table B.5.

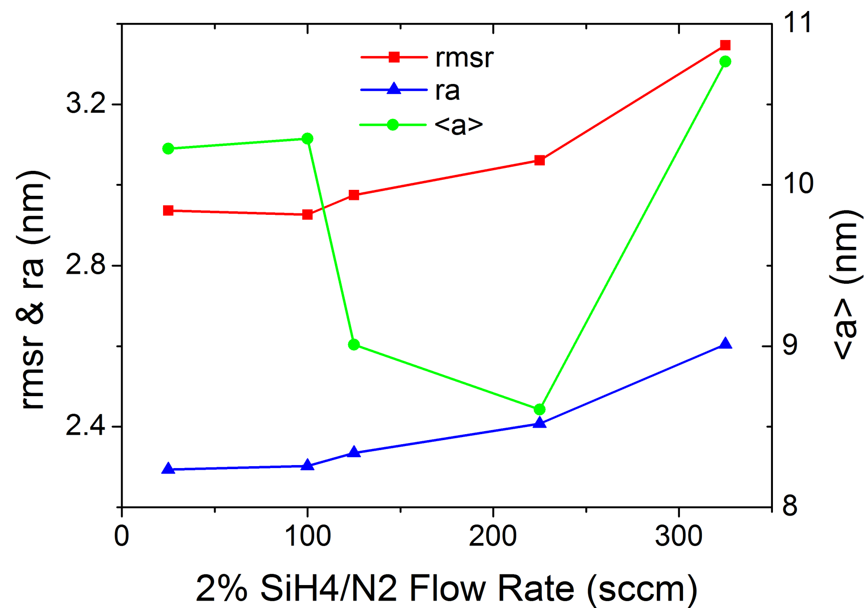

Figure 4.24 *AFM roughness measurement data of SiO_2 samples S13-S17, where the flow rate was the variable.*

Surprisingly the roughness indicators *rmsr* and *ra* both show decreasing trend as the SiH_4 flow is reduced. The changes are, however, so small (less than 0.5 nm) that the surface roughness does not indicate any effective changes in porosity. This could mean that the bigger contributor to the film porosity is the growth temperature and the precursor gas ratio would essentially affect mainly the molecular ratio of Si and O. Finding out for sure would require X-ray spectroscopy and additional SEM imaging not included in this thesis.

To design an AR coating one needs to know the dispersion behavior of the materials, that are supposedly constructing the coatings layer structure. This is why selected SiO_2 samples were also sent to VASE measurements and the results are shown in fig. 4.25.

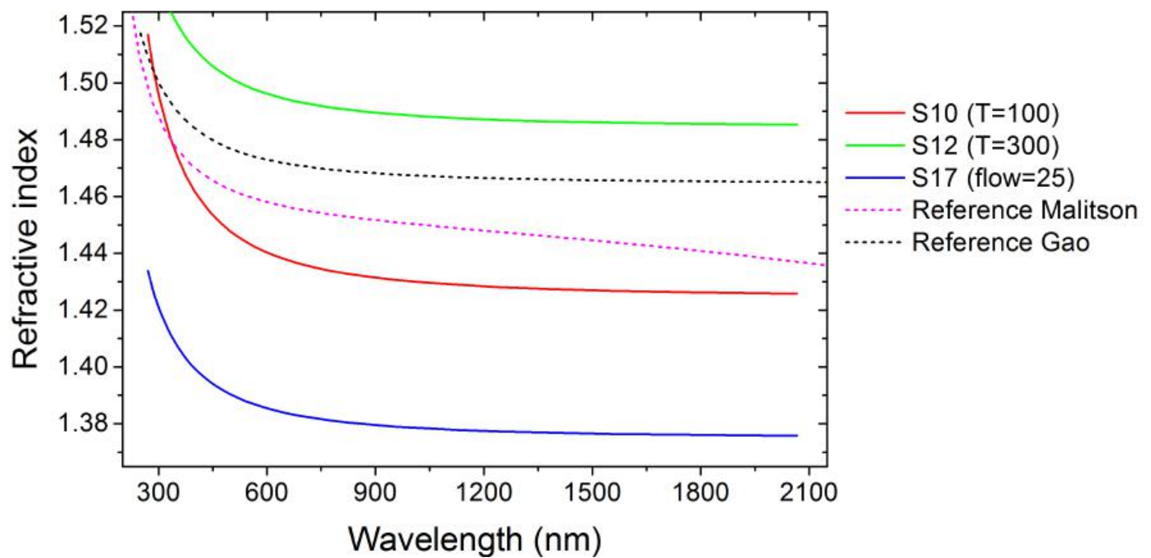

Figure 4.25 *The dispersion curves for SiO_2 samples S10, S12 and S17 measured with VASE and reference refractive indices from Malitson* et. al *[47] and Gao* et. al *[44].*

The sample S12 is our reference for normally deposited PECVD SiO_2. The main reason why it differs quite much from the literature references is that those values are acquired from bulk samples and not from thin films. [44, 47] More interestingly the S10 sample is the cross-point for the temperature and flow ratio series and thus gives a hint how the rest of the SiO_2 samples (S9, S11, S13–S16) would have settled in this graph. The lower the refractive index the smaller is the reflection of the boundary of air and coating's surface. This encouraged to choose the sample S17 for the third specimen in SiO_2 dispersion measurements. It can be seen from fig. 4.25 that the refractive index of the sample S17 goes as low as 1.38, which is essentially same than for MgF_2 on average.

The results would indicate that the refractive index of PECVD deposited SiO_2 thin films can effectively be manipulated by tuning the growth temperature and the

precursor gas ratio. There were also signs that the temperature would mainly affect the porosity of the film and that by gas ratio tuning one could alter the refractive index without decreasing the mechanical durability of the film. This, however, still requires some more studying before any certain conclusions can be made. From the SiO_2 samples the lowest acquired refractive index material is chosen to be used as an AR coating's low index layer, which namely means the sample S17.

4.1.3 Characterization of SC510K and SC800i Siloxanes

One part of the study was to characterize two commercial AR coating materials, that are developed and distributed by Pibond corporation. Main interest was to find out if these spinnable materials would be suitable for MJSC AR coatings. The layer deposition was done by spinning method that is presented in section 3.1.3. The coating solutions were supplied by Pibond and the tests were carried out at ORC. In the table 4.3 is presented the different samples fabricated from SC510K and SC800i. The samples S18 and S19 differ from the rest, as they were the first test samples done from these coatings and their spinning time was longer and they were just deposited with parameters that produced seemingly homogeneous layers. The extensive info of all the used parameters can be found in table A.3.

Table 4.3 *The siloxane samples and their inspected growth related variables.*

Sample ID	Substance	Variable	Value
S18	SC510K	Round speed (rpm)/open	2000
S19	SC800i	Round speed (rpm)/closed	2000
S20	SC800i	Round speed (rpm)/open	1500
S21	SC800i	Round speed (rpm)/closed	1500
S22	SC800i	Round speed (rpm)/open	2000
S23	SC800i	Round speed (rpm)/closed	2000
S24	SC800i	Round speed (rpm)/open	2500
S25	SC800i	Round speed (rpm)/closed	2500
S26	SC510K	Round speed (rpm)/open	1500
S27	SC510K	Round speed (rpm)/closed	1500
S28	SC510K	Round speed (rpm)/open	2000
S29	SC510K	Round speed (rpm)/closed	2000
S30	SC510K	Round speed (rpm)/open	2500
S31	SC510K	Round speed (rpm)/closed	2500

The main characterization device for the other two sample groups, namely MgF_2 and SiO_2, was the monochromatic ellipsometer that measured film thickness and the refractive index at the wavelength 632.8 nm, as it is easy to use and gives relative data quite fast. With siloxanes, however, the device limitations caused

problematics. With SC510K the extreme low refractive index and the thin film thickness probably exceeded the ellipsometer's measurement precision and it could not calculate any values for n and d. With SC800i the ellipsometer calculated values for the measurements, but the inconsistency between measurements proved the results unreliable, as measurements of the same sample wafer, 6 mm times 6 mm silicon piece coated with SC800i, gave values from 2.53 to 2.98, which are much too large values altogether. The explanation for the inconsistency of SC800i measurements was revealed later as the samples were characterized with AFM and SEM. The SC800i layer is inhomogeneous in the way, that is has distinct layers of different densities within the overall structure. Both of the coatings were measured with spectrophotometer and their reflectances are shown in fig. 4.26.

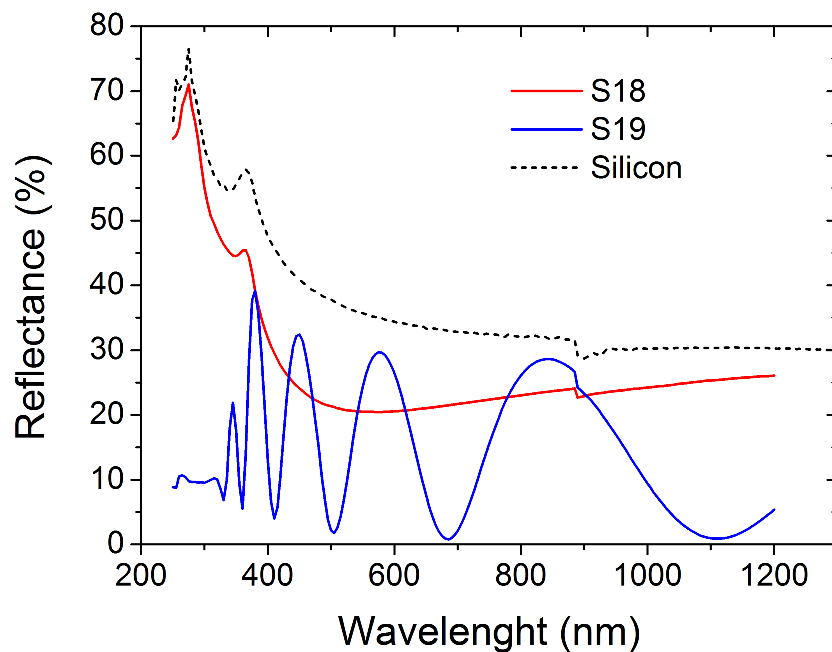

Figure 4.26 *The reflectances of the siloxanes SC510K and SC800i.*

The SC510K has similar reflectance profile than any other dielectrics measured in this thesis, but the SC800i shows a clear interference pattern, that cannot be caused by a single homogeneous layer. To find out more of the surface structure of the siloxanes, they were measured with AFM to characterize their surface roughness. In fig. 4.27 is presented a comparison between SC510K and SC800i.

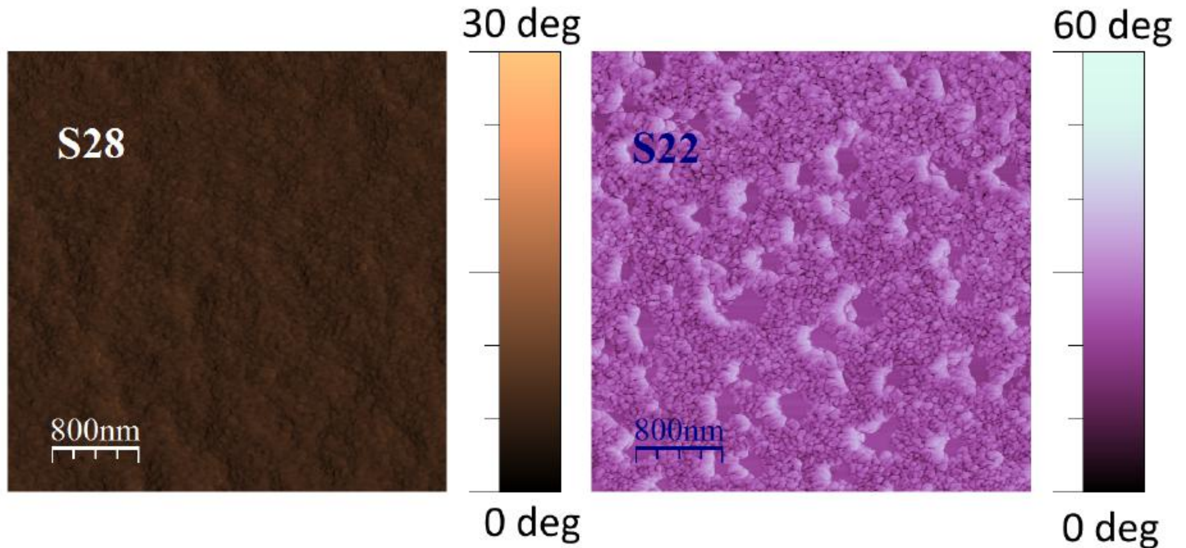

Figure 4.27 *AFM phase pictures for structural comparison between SC510K and SC800i.*

It is clear that the SC510K has far smoother and more uniform structure than SC800i. The phase imaging done with the AFM reveals the shapes of surface morphologies in a clearer way than the straightforward height figures. In SC800i one can see granular surface structures and large pores that of some are nearly 500 nm wide. To find out more of the siloxane surfaces and the examined parametrization each of the samples S20–S31 was measured with AFM and the results are gathered in fig. 4.28–4.31. The surface topology maps of SC800i and SC510K AFM measurements are presented in tables B.5 and B.6, respectively. The roughness analysis values for SC800i are tabled in table B.6 and for SC510K in table B.7. In fig. 4.28 are the results for SC800i that were spinned with lid open.

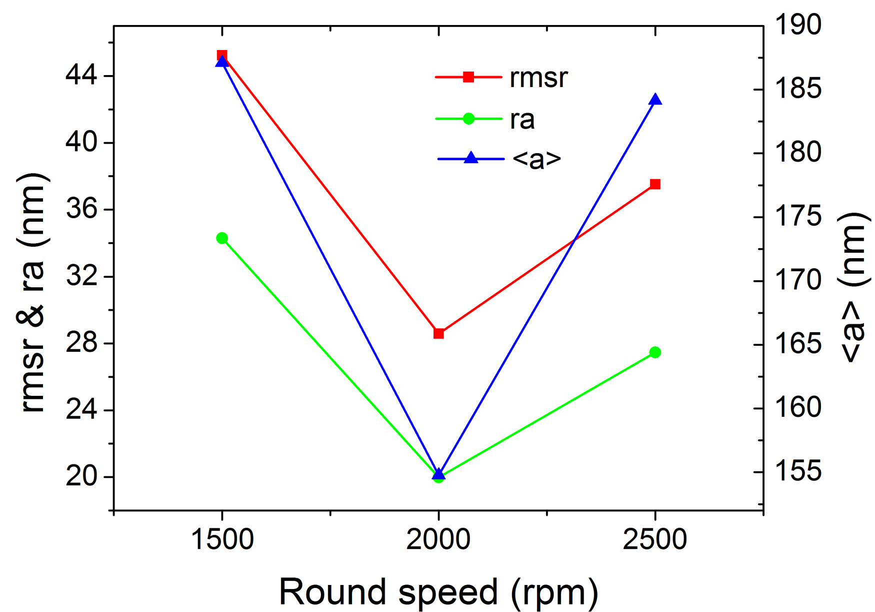

Figure 4.28 *Roughness data from AFM measurements for SC800i samples (S20, S22, S24), which have been spinned with the lid open.*

Noticeable is that with the round speed given by the manufacturer, the surface structure is at its smoothest form. Another thing is that for an optical thin film the roughness values are rather high (over 30 nm) when compared for example the silicondioxide's *ra* that was around 3 nm. In fig. 4.29 are the results for SC800i that were spinned with lid closed. The graph is quite similar to the lid open situation, but for the slowest speed (1500 rpm) the roughness has decreased from the lid open situation, the 2000 rpm is essentially remaining the same and for 2500 rpm there's a small shift towards rougher surface, but not meaningfully. A statement could be made that the process recommended by the supplier has been thouroughly optimized.

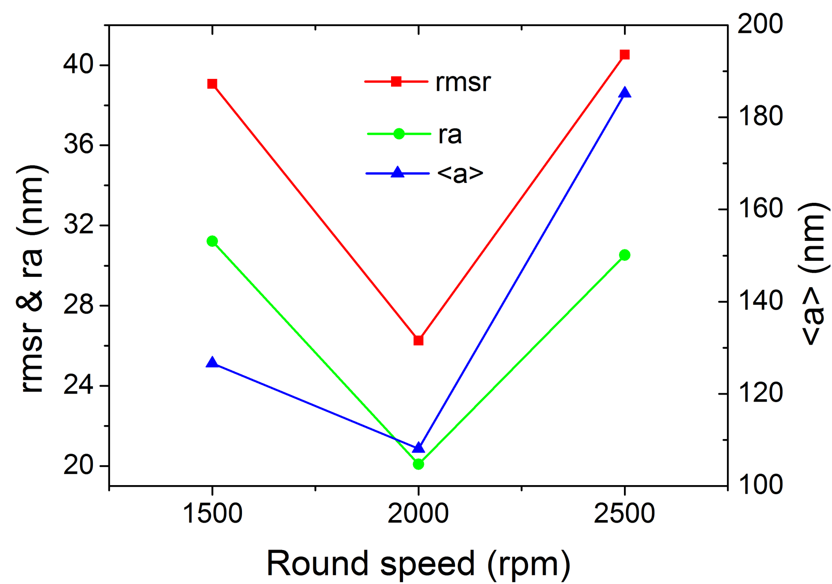

Figure 4.29 *Roughness data from AFM measurements for SC800i samples (S21, S23, S25), which have been spinned with the lid closed.*

In fig. 4.30 are the results for SC510K that were spinned with lid open. With the low refractive index material, it's not a surprise that the surface roughness is closer to the conventional values of dielectrics, as the usage as an AR coating on its own requires low loss at the surface interface and rough surface scatters light. With the SC510K the *rmsr* and the *ra* are rather constant, but small growth can be seen when going towards the larger scale.

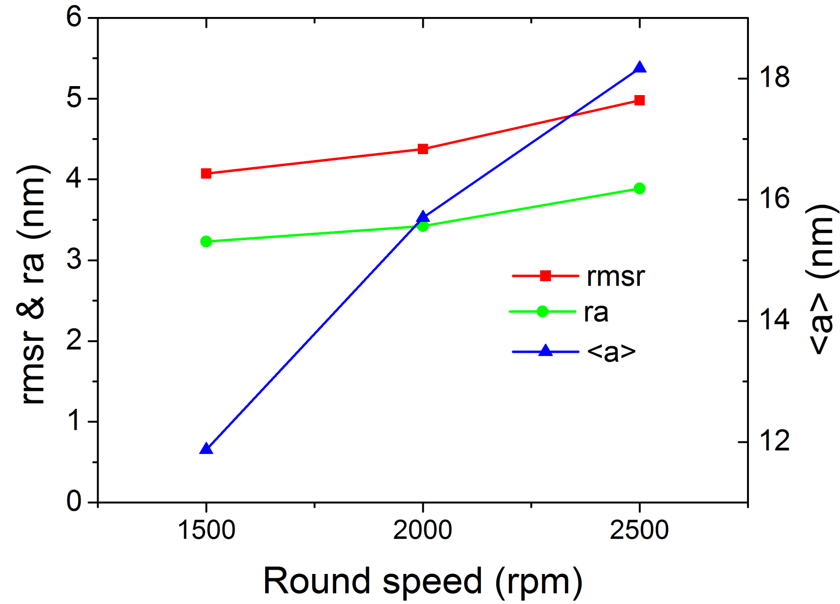

Figure 4.30 *AFM measurement results for SC510K samples (S26, S28, S30), which have been spinned with the lid open.*

In fig. 4.31 are the results for SC510K that were spinned with lid closed. These samples behave distinguishly from the others as the closed lid raises their refractive index and at the speed of 2000 rpm it has the highest *rmsr* of this substance samples differing about 6 nm from otherwise identical setup, but the different position of the lid.

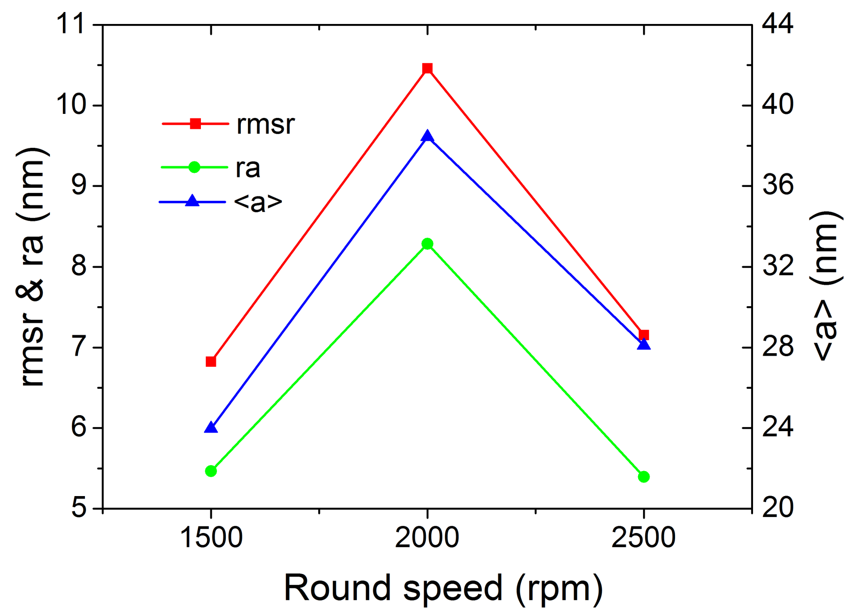

Figure 4.31 *AFM measurement results for SC510K samples (S27, S29, S31), which have been spinned with the lid closed.*

As the AFM measurements would indicate, the surface structures of the two siloxanes SC510K and SC800i differ greatly from each others. This was confirmed with SEM imaging as can be seen in fig. 4.32. The SEM image reveals that also the SC510K has pores in its film structure, but not as much SC800i.

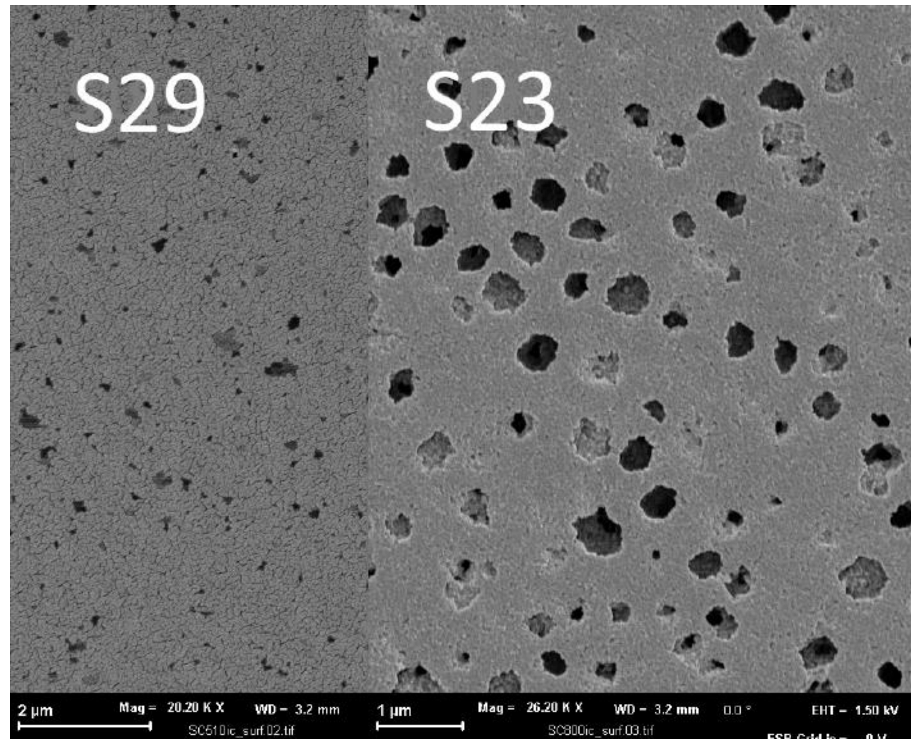

Figure 4.32 *SEM image comparison between the surfaces of SC800i (S23) and SC510K (S29) thin films.*

Both of the samples SC510K and SC800i were sent to ellipsometric VASE measurements to find out their dispersion profile. The inconsistent structure of SC800i, with TiO_2 nanoparticles, large number of pores and the distinctively inhomogeneous layers, resulted to unsuccessful measurement attempt and no dispersion curve was received. The SC510K, however, was more or less regular sample and its refractive index profile can be seen in fig. 4.33.

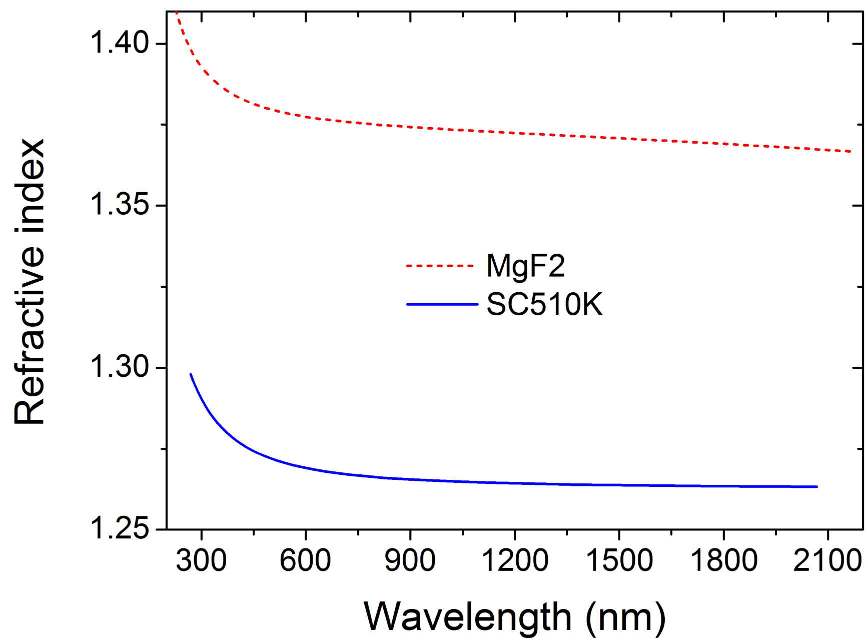

Figure 4.33 *The refractive index profile for SC510K measured with VASE and as comparison the MgF_2 dispersion curve from Dodge [48].*

To put the refractive index of SC510K into a right perspective there is also presented the dispersion curve of MgF_2 as it has the lowest natural refractive index among dielectrics. To find out more about the structure of the coating SC800i cross-sectional SEM images were taken.

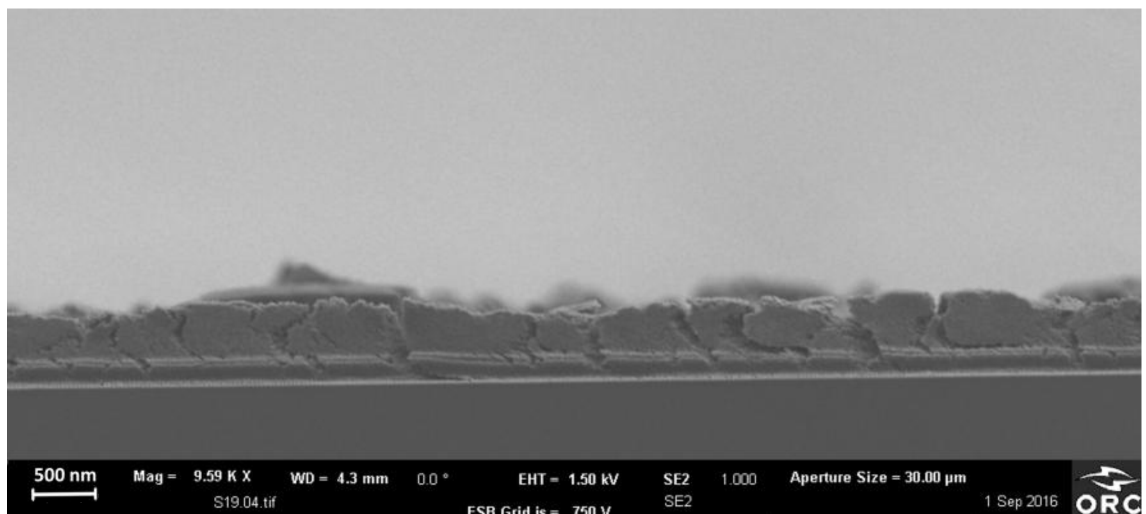

Figure 4.34 *Cross-sectional SEM picture of SC800i layer.*

In fig. 4.34 is clearly visible the cracking of the thin film, likely caused by cleaving

of the SEM sample, and inhomogeneous film structure as there seems to be different kinds of layers within the thin film. The bottom 200 nm next to the substrate seems rather intact and homogeneous, and after an intermediate layer the film structure starts cracking. One explanation could be that heating this thick layer on a heating plate creates a non-uniform heat distribution and only the lower part of the film is properly heated. A possibility would be to do the heating process in an oven for even heat conduction. In any case the intermediate visibly lighter layers should not be formed as the thin film theories consider mainly homogeneous structures and the cracking is not a good property for films in general.

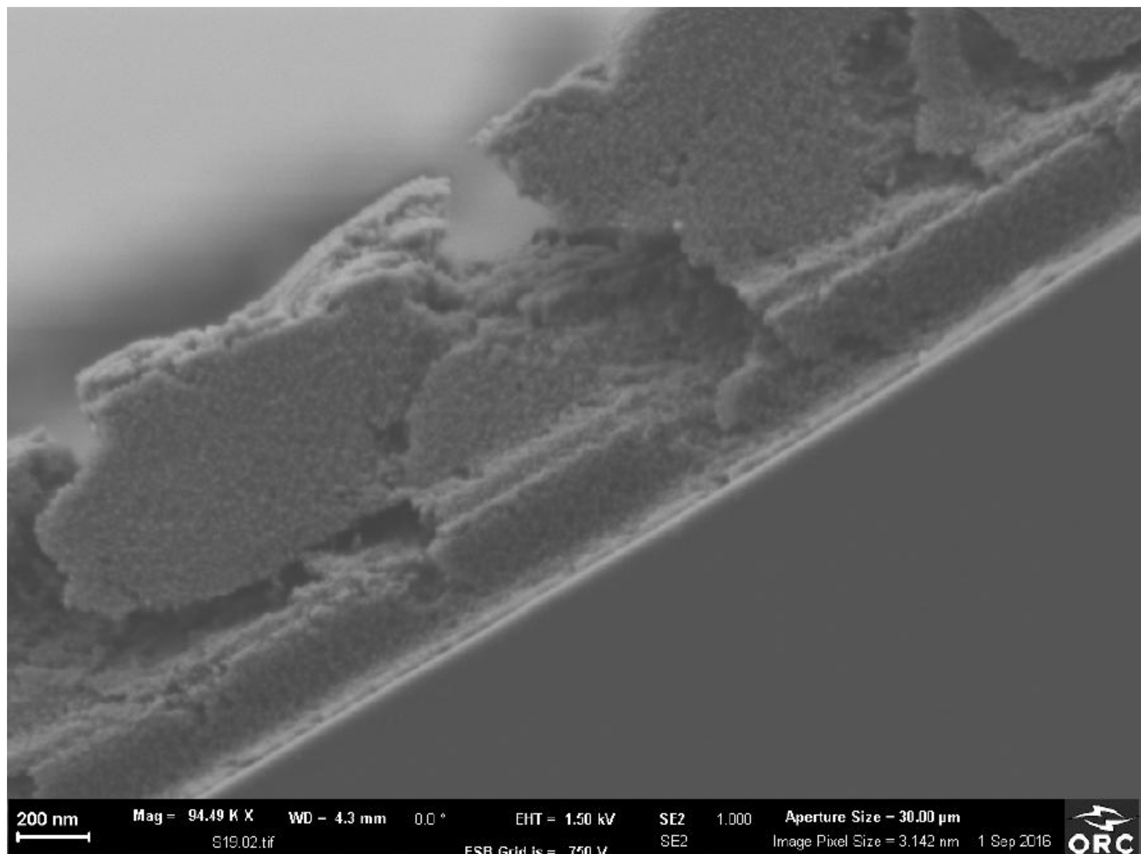

Figure 4.35 *A closer cross-sectional SEM picture of SC800i layer.*

A closer look in fig. 4.35 shows that the interface with silicon has different structure than the rest of the film. It appears lighter and somewhat denser than other structures. Then about 200 nm thick layer with uniform and dense appearance after which comes an inhomogeneous intermediate layer and then the rest of film starts cracking. There is also a clear difference in shades of the two main layers as the better quality lower layer has darker tone than the cracking upper part of the film. The figure also reveals the TiO_2 nanoparticles in the film as they give it the grainy appearance that differs from regular dielectric films.

Due to the characterization difficulties for SC800i siloxane, it was decided to leave it out from AR coating designs. Its properties, however, seem promising and more study would be in order. Main cause for the structural problems are likely from the processing steps that are somewhat different from the usual commercial scale it's designed for. For the characterization the included TiO_2 particles are a challenge for current optical theories, as the EMAs could not effectively fit any reliable dispersion curve for the ellipsometric measurement data. These reasons and the limited time window ruled the siloxane SC800i out of this thesis' AR designs.

With the SC510K the properties are even more promising for variable designs, although in this study it was tested only as a lower index layer with TiO_2. As with SC800i, more tests are in order and the fact that its refractive index is the lowest of all the tested materials within this thesis, shows that is has good possibility to be part of very effective AR designs after the processing is optimized for this purpose. As the manufacturer is able to fine-tune the thickness properties for the spinnable solutions with different solvent ratios the siloxanes can have numerous different applications in the field of optical thin films.

4.2 The Applicability of the Anti-reflective Coatings for Multi-junction Solar Cells

Four different AR coatings were simulated with Essential Macleod and fabricated on MJSCs, with the help of parametric information acquired from the characterizations of the material properties related to their deposition conditions. The coatings were MgF_2/TiO_2 double layer, nanoporous SiO_2 with TiO_2, SC510K/TiO_2 and triple layer AR of $MgF_2/Al_2O_3/TiO_2$. As a reference I have compared the results to the conventional SiO_2/TiO_2 double layer that has been previously used at ORC as a MJSC AR coating. The MJSC in question has subcells of InGaP, GaAs and GaInNAsSb fromtop to bottom, and which of the top cell, namely InGaP, has been the current limiting cell. This means that if we increase the current produced by the top cell, we increase the total current of the MJSC as long as the InGaP remains the limiting cell. In order to do so we must lower the reflectance at the UV range of the solar bandwidth for this particular MJSC design. The reflectance models of our optimized and simulated AR coatings are shown in fig. 4.36. It can be seen that the reflectance profiles of the coatings are quite similar and the differences are rather small. The most distinctive difference is the triple layer coating's lower reflectance near the UV region. Other clear difference is the MgF_2/TiO_2 coating's lowest reflectance in the range of 450–800 nm.

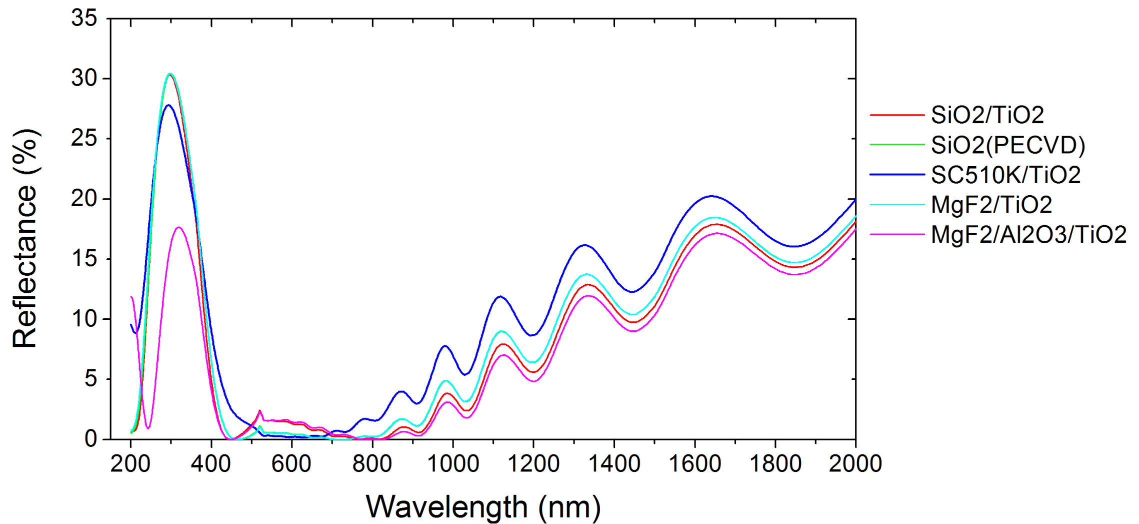

Figure 4.36 *The simulated reflectances of the AR coatings.*

The calculated average reflectances over the entire bandwidth from 200 to 2000 nm are 10.94 % for reference SiO_2/TiO_2, 11.30 % for MgF_2/TiO_2, 12.26 % for nanoporous SiO_2/TiO_2, 12.65 % for SC510K/TiO_2 and 10.49 % for $MgF_2/Al_2O_3/TiO_2$ triple-coating. No big differences are shown and eventually the functionalities will come down to the UV range performance as the InGaP subcell is the limiting section with this configuration. From these designs only the $MgF_2/Al_2O_3/TiO_2$ triple-layer seems to beat the reference coating's performance, but the reality will be seen after measurements. All in all it would be important to prove that the designs are fitting for MJSC AR coatings and that the parametric information gained in section 4.1 holds true. If this is the case the further improved designs with these materials will become a future prospect.

The I-V behavior of the solar cells, under one sun illumination with the AM1.5D spectrum, used in AR testing was measured before and after the deposition of AR coatings. Next figure 4.37 presents the I-V curves for uncoated test cells that were used to characterize the functionality of the designed AR coatings. The test SCs are identified with IDs C1–C11 and the I-V measurements revealed leakage in three cells namely C1, C3 and C7. Otherwise the cells have rather equal performance and their functionality fits well to the performance evaluation of the AR coatings. The cell C11 was kept as a reference cell and was not coated with AR coating.

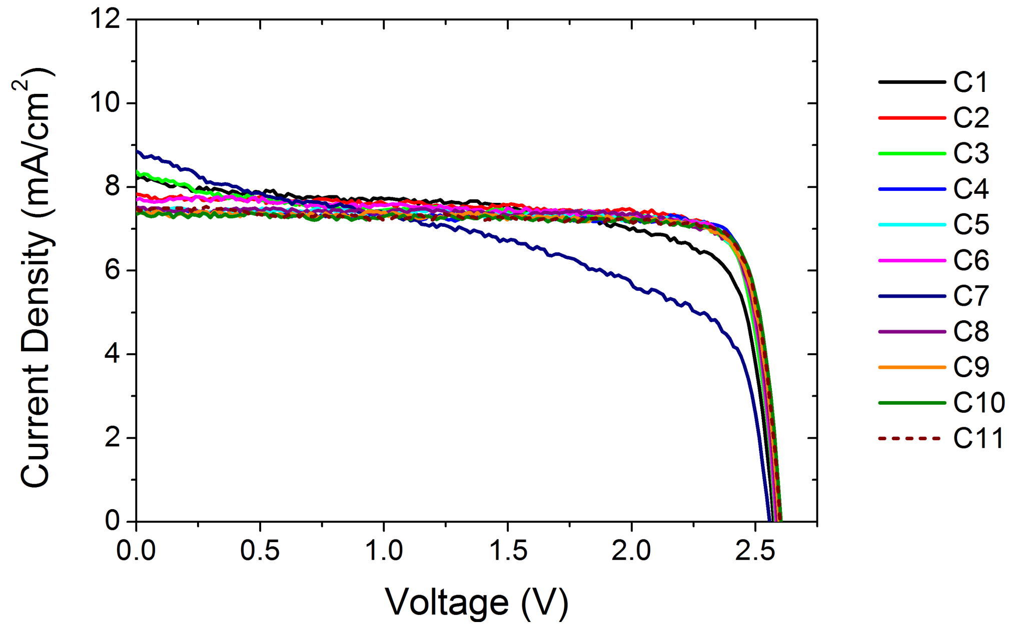

Figure 4.37 *The I-V measurements of the solar cells before AR coatings.*

The overall number of the test cells is rather small, but for indicative measurements of the AR coating functionalities larger number was not seen necessary. This, however, leaves more room for process errors and coincidences, so any wider applicative deductions are not possible. The table 4.4 presents the cell IDs coupled with the AR coatings that were used for each cell.

Table 4.4 *How the solar cells were coated with AR coatings.*

Sample ID	The AR Coating
C1, C2	SiO_2/TiO_2
C3, C4	SiO_2(PECVD)/TiO_2
C5, C6	SC510K/TiO_2
C7, C8	MgF_2/TiO_2
C9, C10	$MgF_2/Al_2O_3/TiO_2$
C11	Uncoated

The cells C1 and C2 are coated with the reference SiO_2/TiO_2, the C3 and C4 are having the nanoporous SiO_2 coatings, the cells C5 and C6 were applied with the siloxane SC510K/TiO_2 coating, the C7 and C8 had MgF_2/TiO_2 double layer AR coating and the cells C9 and C10 were coated with the triple layer design $MgF_2/Al_2O_3/TiO_2$.

The reference AR coatings' structure is previously optimized for MJSCs and has

widely been used on different kinds of cells at ORC. Its functionality is good and it provides reliable comparison for the coatings designed and manufactured with the materials included in the previous sections' parametrizations. The layer thicknesses of the coating are shown in fig. 4.5. To find out the solar cells' performance they were measured in solar simulator to get the I-V behavior. The used spectrum was AM1.5D, where the irradiance is normalized to 1000 W/m^2.

Table 4.5 *The structure of the reference SiO_2/TiO_2 AR coating.*

C1, C2	
Materials	**Layer Thickness (nm)**
SiO_2	100
TiO_2	60

An AR coatings performance is dependent on the amount of photons of different wavelengths that actually reach the cell structure and are not reflected away from the surface. This why the reflectance over the solar bandwidth plays a major role in the coatings applicability. In fig. 4.38 is shown the modeled reflectance spectrum for the reference coating SiO_2/TiO_2 and the measured spectra that were acquired with PL mapper and spectrophotometer.

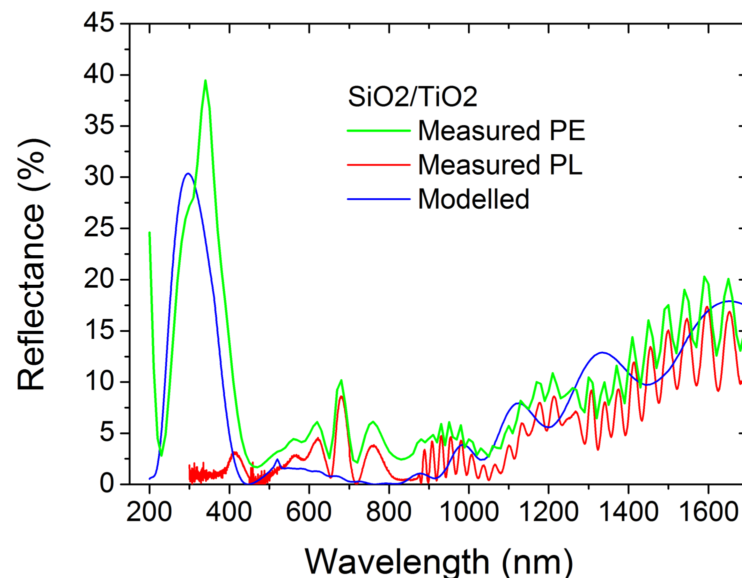

Figure 4.38 *Reflectance of the SiO_2/TiO_2 AR coating on MJSCs and the modeled reflectance from Essential Macleod.*

It can be seen that the modeled spectrum gives a rather good evaluation of

the actual reflectance, but some main differences occur. The fringing of the real spectra is caused by the additional layer structures that were not included in the theoretical model that calculated the values. The PL mapper curve follows the magnitude given by the modeled spectrum rather well and there are not any bigger differences. The curve measured with spectrophotometer, however, has constantly few per cent greater reflectance than the modeled curve. When averaged over the entire bandwidth from 200 to 2000 nm the difference is approximately 4 %. This deviation is explained by the omitting of scattered light in the theoretical model and with the PL mapper, as the spectrophotometer's integrating sphere module takes all reflected and scattered light in to notion. The modeled average reflectance over the entire bandwidth was 6.88 % and the real reflectance measured with the spectrophotometer is 10.94 %. The coating reduces the overall reflectance from the uncoated surface about 20.34 %.

In fig. 4.39 is presented the I-V curves for the cells C1 and C2, that were coated with the conventional EBE deposited SiO_2/TiO_2 AR coating. The dotted lines represent the uncoated cells' performance and the solid curves are the performance improved by the AR coating.

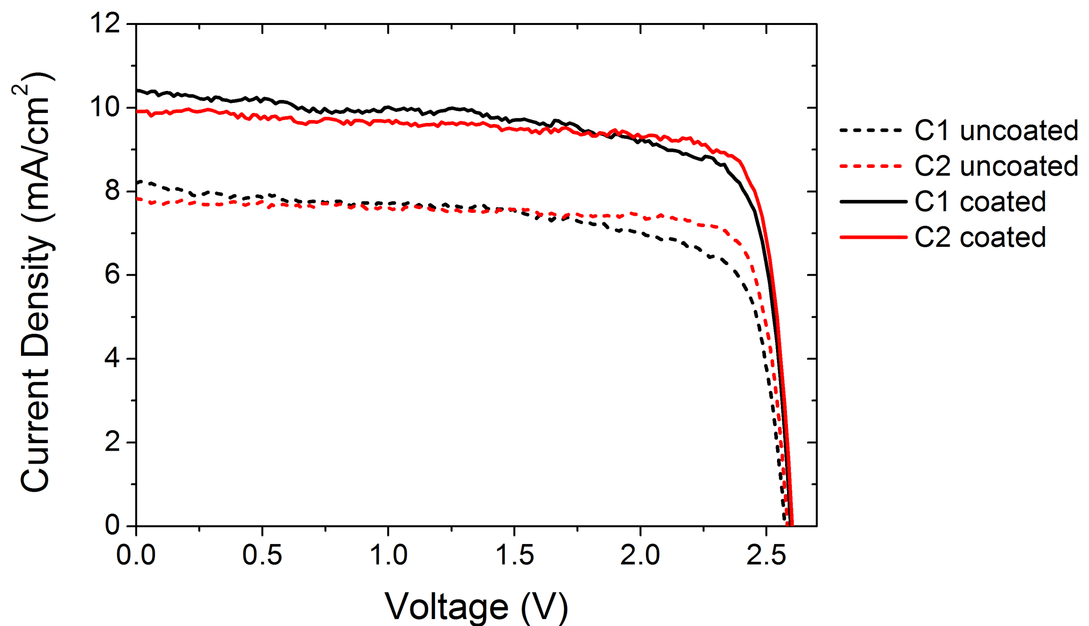

Figure 4.39 *The I-V-curves of MJSCs before and after the conventional SiO_2/TiO_2 AR coating.*

The cell C1 shows a possible current leakage behavior, as the curve rises towards the J_{sc} and then starts to fall long before the V_{oc}. The cell C2, however, has a nice looking curve, that provides suitable reference for all the other cells coated with

different AR coatings. With the solar simulator one gets many important values that can be used for cell comparison and performance evaluation. These values for the cells C1 and C2 are tabled in table 4.6.

Table 4.6 *Results of the I-V performance for cells C1 and C2 with SiO_2/TiO_2 AR coating.*

Sample ID			**C1**	
	No AR	**With AR**	**Change**	**Percentual Change (%)**
Efficiency (%)	14.75	19.78	5.04	34.2
$\mathbf{V_{oc}(V)}$	2.57	2.60	0.02	0.9
$\mathbf{I_{sc}(mA)}$	2.05	2.62	0.57	27.9
$\mathbf{J_{sc}(mA/m^2)}$	8.19	10.48	2.29	28.0
Fill Factor (%)	70.02	72.73	2.71	3.9
$\mathbf{P_{max}(mW)}$	3.69	4.95	1.26	34.1
Sample ID			**C2**	
	No AR	**With AR**	**Change**	**Percentual Change (%)**
Efficiency (%)	16.25	20.65	4.40	27.1
$\mathbf{V_{oc}(V)}$	2.58	2.60	0.02	0.7
$\mathbf{I_{sc}(mA)}$	1.95	2.48	0.53	27.1
$\mathbf{J_{sc}(mA/m^2)}$	7.81	9.93	2.12	27.1
Fill Factor (%)	80.56	79.99	-0.57	-0.7
$\mathbf{P_{max}(mW)}$	4.06	5.16	1.10	27.1

As this test MJSC's structure is optimized for AM0 environment and the characterization is done with AM1.5D, no high performance figures are to be expected. The relative changes, however, offer a suitable meter for AR coating evaluation, when the overall functionality is under inspection. Both cells C1 and C2 have approximately 27 % increase in their current densities which can be taken as a reference value, when the other coatings are inspected. Otherwise these I-V performance values of the cells C1 and C2 are regular values of an average functioning solar cell, outside its optimum working range. It's notable that for the properly working cell C2 the relative values of efficiency, current behavior and maximum power percentual changes are essentially equivalent, as they should be. If there's bigger deviation between these values the cell's functionality is somehow deteriorated. In addition to these values the limiting current densities were measured and calculated for each subcell of the cell C2. For InGaP, GaAs and GaInNAsSb subcells they were 9.9 mA/m^2 15.9 mA/m^2 and 17.2 mA/m^2 respectively. The values are tabled in table 4.15 for overall comparison between all AR coating designs.

With this background overview for the reference AR coatings and solar cells, we can now continue to the evaluation of the designed coatings.

4.2.1 The Anti-reflective MgF_2/TiO_2 Double Layer

In the earlier section 4.1.1 the EBE deposited MgF_2 parameters were studied in accordance to their influence to the optical and mechanical properties of the MgF_2 films. The dispersion behavior measured with VASE was noticed to change as the substrate temperature was altered. With the gained information of MgF_2 properties, one parametrization was chosen for AR coating low index layer participant. At the temperature of 200 °C deposited MgF_2 was combined with TiO_2 for manufacturing an AR coating for MJSC applications. The designing was done with Essential Macleod and the optimized a double layer structure MgF_2/TiO_2 was manufactured with EBE. This AR coating was fabricated on two triple-junction solar cells C7 and C8. The layer structure is presented in table 4.7.

Table 4.7 *The structure of the optimized MgF_2/TiO_2 AR coating.*

C7, C8	
Materials	**Layer Thickness (nm)**
MgF_2	103
TiO_2	56

The modeled reflectance for the coating is compared to the measurements done with PL mapper and spectrophotometer. The sample from which the reflectance is measured, is a MJSC coated with the AR coating, but without the front contacts. The reflectance spectra for MgF_2/TiO_2 are shown in fig. 4.40.

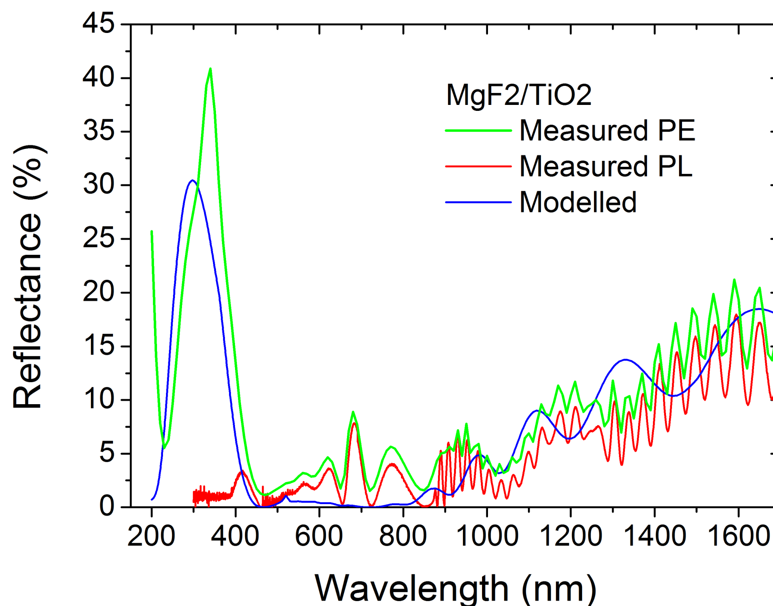

Figure 4.40 *Reflectance of the MgF_2/TiO_2 AR coating on MJSCs and the modeled reflectance from Essential Macleod.*

The spectra are almost identical with the reference spectra of SiO_2/TiO_2 AR coating. Calculated averages of the measured spectra over the entire bandwidth of 200–2000 nm differ less than 0.5 %, so their functionality is essentially the same.

As what comes to the test cells that MgF_2/TiO_2 AR coating was applied to, the cell C7 was faulty to begin with. The cell C8 had proper I-V curve before the AR coating, but after the applied coating the functionality did not improve as much as would have been expected according to the measured reflectance. The comparison of the cells covered with MgF_2/TiO_2 AR coating and the reference samples are shown in fig. 4.41.

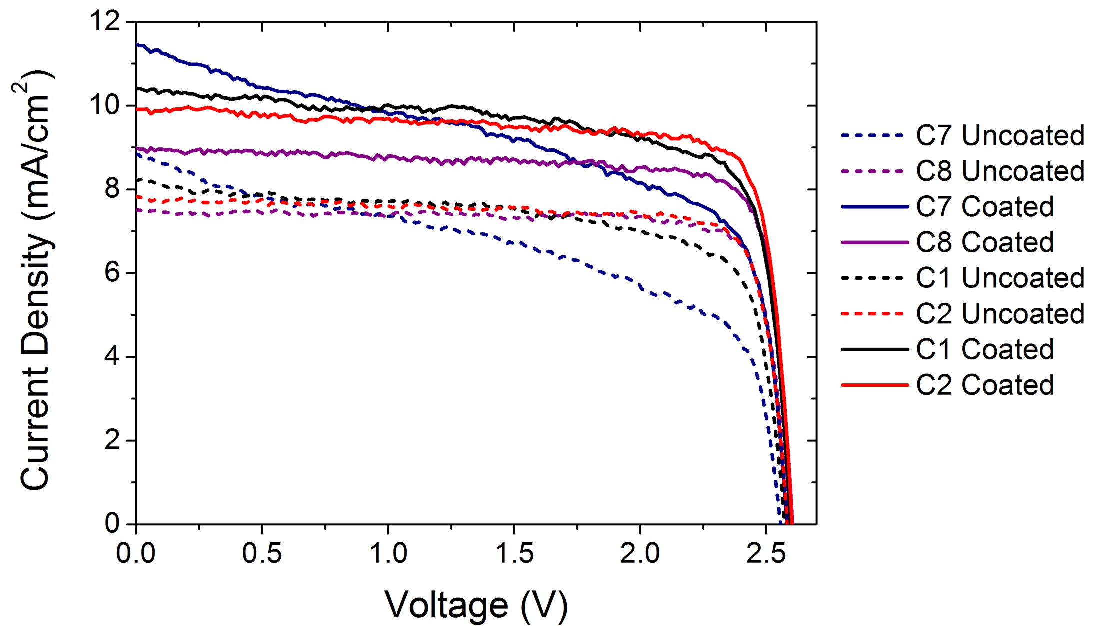

Figure 4.41 *The IV-curves of MJSCs before and after MgF_2/TiO_2 AR coating.*

As can be seen the coated C8 is about 1 mA/cm^2 behind in current density, when compared to the C2. The current improvement in C7 was exceptional, but it can be explained by its low starting figures and the possibility that the AR coating has passivated some leaking components on the cell's surface. The detailed I-V characteristics are shown in the table 4.8.

Table 4.8 Results of the I-V performance for cells C7 and C8 with MgF_2/TiO_2 AR coating.

Sample ID	C7			
	No AR	**With AR**	**Change**	**Percentual Change (%)**
Efficiency (%)	11.52	17.01	5.49	47.6
$\mathbf{V_{oc}(V)}$	2.56	2.58	0.03	1.0
$\mathbf{I_{sc}(mA)}$	2.22	2.90	0.67	30.2
$\mathbf{J_{sc}(mA/m^2)}$	8.89	11.58	2.69	30.2
Fill Factor (%)	50.69	56.90	6.21	12.3
$\mathbf{P_{max}(mW)}$	2.88	4.25	1.37	47.6
Sample ID	**C8**			
	No AR	**With AR**	**Change**	**Percentual Change (%)**
Efficiency (%)	16.02	18.89	2.87	17.9
$\mathbf{V_{oc}(V)}$	2.59	2.60	0.01	0.5
$\mathbf{I_{sc}(mA)}$	1.87	2.24	0.38	20.2
$\mathbf{J_{sc}(mA/m^2)}$	7.46	8.97	1.51	20.2
Fill Factor (%)	82.90	80.92	-1.98	-2.4
$\mathbf{P_{max}(mW)}$	4.00	4.72	0.72	18.0

The current improvement for C8 was only 20 % and the coating's effect on efficiency even lower. When taking a closer look to the table of the cell C8, we notice that the fill factor has decreased and that overall functionality does not seem good. Most likely the C8 has been damaged during the coating process, as even plastic tweezers can, with a bit bad luck, damage the side facets of the cell. As we had only two test cells for MgF_2/TiO_2 AR coating, where C7 did not function well even to begin with, we must make our conclusions based on the measured reflectance spectrum which showed that the coating should work as well as the reference coating SiO_2/TiO_2. Also the limiting currents of the subcells were measured for the cell C8 and the results are shown in the comparison table 4.15 in the conclusive AR section 4.2.5.

4.2.2 The Nanoporous SiO_2 Based Anti-reflective Coating

The PECVD deposited nanoporous SiO_2 was characterized with ellipsometry and AFM and SEM to find out suitable parameters that would produce low index dielectric films with suitable optical and mechanical properties for AR coatings. The dispersion behavior measured with VASE was noticed to decrease as the growth temperature and flow ratio were altered. With the lowest refractive index SiO_2 that was produced, an AR coating with TiO_2 as the high index material was designed and manufactured. The design was optimized with Essential Macleod and the layer structures are shown in fig. 4.9. This AR coating was fabricated on two MJSC test

cells, namely C3 and C4.

Table 4.9 *The structure of the optimized nanoporous SiO_2/TiO_2 AR coating.*

C3, C4	
Materials	**Layer Thickness (nm)**
SiO_2	102
TiO_2	56

The similarity to the reference SiO_2/TiO_2 spectrum and to the MgF_2/TiO_2 reflectance is almost indistinguishable. So any differences on cell performance are not straightforwardly due to the coating's reflectivity. More like just the opposite as the reflectance profiles are so identical.

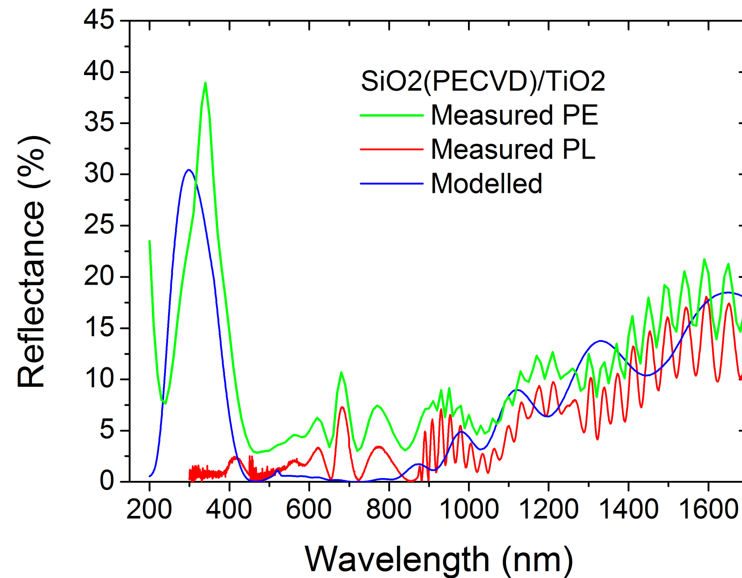

Figure 4.42 *Reflectance of the nanoporous SiO_2/TiO_2 AR coating on MJSCs and the modeled reflectance from Essential Macleod.*

The likeness can also be seen in the I-V behavior of the reference SiO_2/TiO_2 and the nanoporous SiO_2 with TiO_2 coating, as the I-V curves of C3 and C4 are overlapping with the curves of C1 and C2. At the open-circuit end of the curves the PECVD deposited SiO_2 coatings are slightly better, which improves their performance parameters past the reference coatings' values.

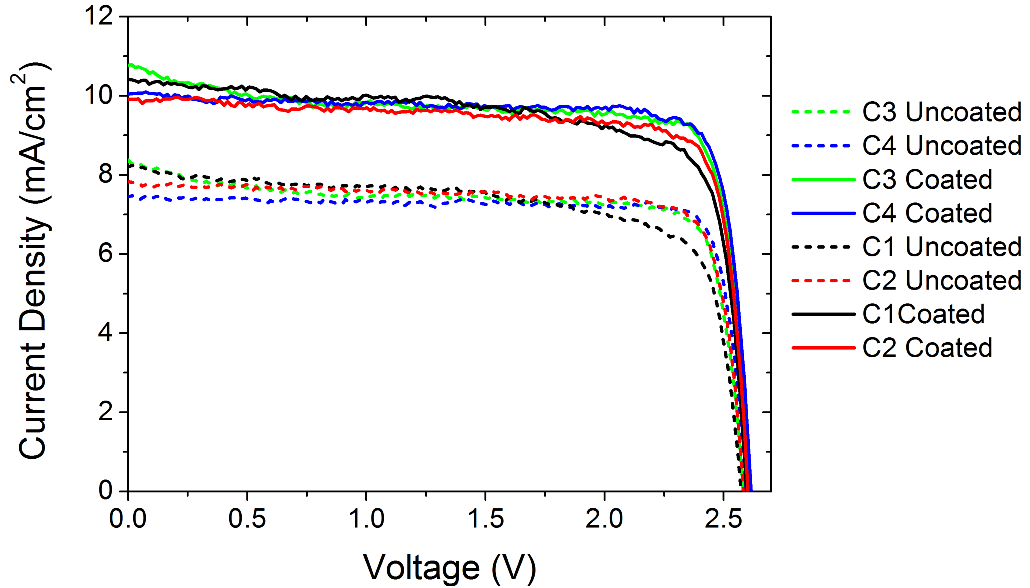

Figure 4.43 *The IV-curves of MJSCs before and after the deposition of the nanoporous SiO_2/TiO_2 AR coating.*

In table 4.10 is presented the I-V performance values of the cells C3 and C4 with SiO_2(PECVD)/TiO_2 AR coating. Both of the cells work well and there are no bigger differences between their performances. Their efficiency is roughly the same, but current behavior distinguishes them for each others.

Table 4.10 *Results of the I-V performance for the cells C3 and C4 with SiO_2(PECVD)/TiO_2 AR coating.*

Sample ID	C3			
	No AR	With AR	Change	Percentual Change (%)
Efficiency (%)	16.28	21.35	5.06	31.1
V_{oc}(V)	2.58	2.60	0.02	0.9
I_{sc}(mA)	2.10	2.70	0.59	28.2
J_{sc}(mA/m^2)	8.41	10.78	2.37	28.2
Fill Factor (%)	74.99	76.03	1.04	1.4
P_{max}(mW)	4.07	5.34	1.27	31.1
Sample ID	**C4**			
	No AR	**With AR**	**Change**	**Percentual Change (%)**
Efficiency (%)	16.46	21.53	5.07	30.8
V_{oc}(V)	2.60	2.61	0.02	0.8
I_{sc}(mA)	1.87	2.51	0.64	34.4
J_{sc}(mA/m^2)	7.46	10.02	2.57	34.4
Fill Factor (%)	85.05	82.14	-2.91	-3.4
P_{max}(mW)	4.12	5.38	1.27	30.8

The current density of the cell C4 is evidently better than of the C3, which has nearly the same current density than the reference cells C1 and C2. The C3, however, had a slight current leakage component in its I-V behavior even prior the AR coating. Thus it is presumable that both nanoporous SiO_2 with TiO_2 coatings worked with the MJSC quite well.

4.2.3 The Siloxane SC510K Based Anti-Reflective Coating

Despite the minor characterization challenges the SC510K seemed an interesting choice for the low index material to a double layer AR coating. As with all the other coatings the high index material was TiO_2. A considerable choice would also have been to use the SC510K on its own and see how it performs, but that is not included to this thesis. In the table 4.11 is presented the approximated layer thicknesses of the coating, as the siloxanes thickness was not tuned with diluting or concentrating the coating solution, so the layer thickness of SC510K was not calibrated in any way.

Table 4.11 *The structure of the optimized siloxane SC510K with TiO_2 AR coating.*

C5, C6	
Materials	**Layer Thickness (nm)**
SC510K	100
TiO_2	59

The unrefined thicknesses lead somewhat higher overall reflectance and the coating itself seemed blue to visible eye, which means that some amount of the visible spectrum at the range of blue is reflected. This is easily verified when seeing the measured reflectance graphs in fig. 4.44, as the reflectance starts sharply to increase at the wavelength of 500 nm which is already in the range of blue color.

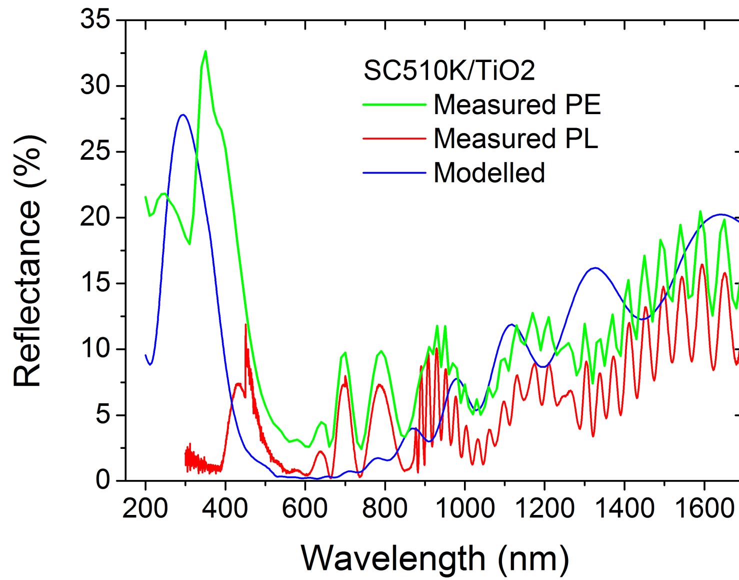

Figure 4.44 *Reflectance of the SC510K/TiO_2 AR coating on MJSCs and the modeled reflectance from Essential Macleod.*

When considered how visible was the difference to other AR coatings fabricated in this thesis the functionality of the SC510K was surprisingly good. In fig. 4.45 is presented the I-V curve for the cells C5 and C6 with and without AR coating.

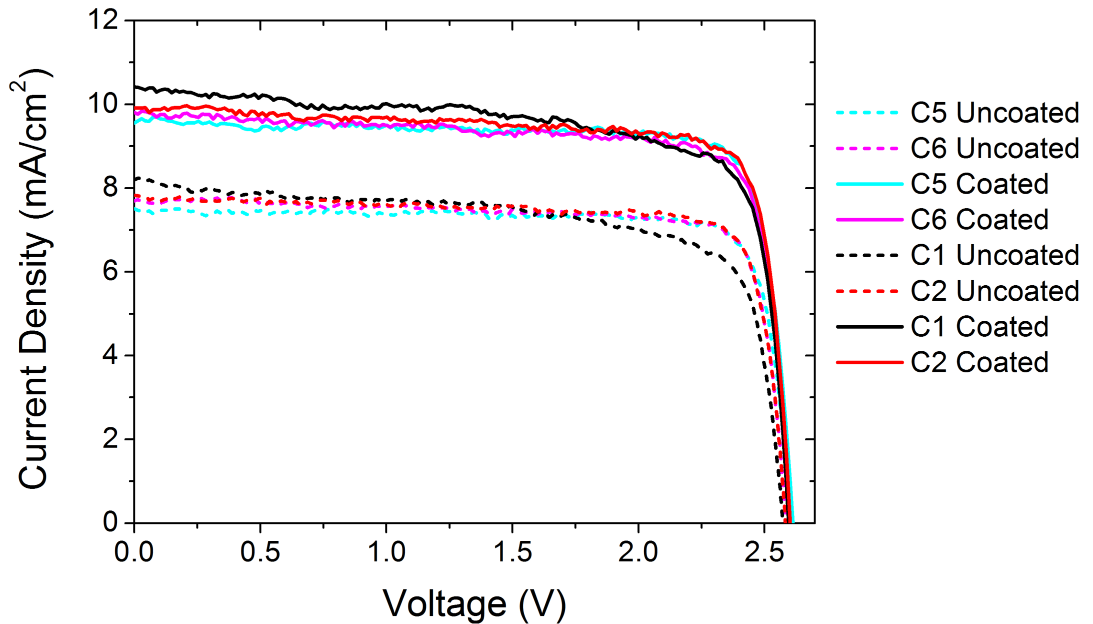

Figure 4.45 *The IV-curves of MJSCs before and after SC510K/TiO_2 AR coating.*

As one watches the I-V curves of the cells coated with SC510K/TiO_2 AR coating and the curve of the reference cell C2, there is no clear difference to be seen. The detailed performance of C5 and C6 is presented in table 4.12.

Table 4.12 *Results of the I-V performance for cells C5 and C6 with SC510K/TiO_2 AR coating.*

Sample ID	**C5**			
	No AR	**With AR**	**Change**	**Percentual Change (%)**
Efficiency (%)	16.19	20.62	4.43	27.4
$\mathbf{V_{oc}}$**(V)**	2.60	2.61	0.01	0.5
$\mathbf{I_{sc}}$**(mA)**	1.87	2.39	0.53	28.2
$\mathbf{J_{sc}}$**(mA/m²)**	7.47	9.57	2.10	28.2
Fill Factor (%)	83.38	82.46	-0.92	-1.1
$\mathbf{P_{max}}$**(mW)**	4.05	5.16	1.11	27.4
Sample ID	**C6**			
	No AR	**With AR**	**Change**	**Percentual Change (%)**
Efficiency (%)	16.21	20.11	3.90	24.1
$\mathbf{V_{oc}}$**(V)**	2.58	2.60	0.01	0.5
$\mathbf{I_{sc}}$**(mA)**	1.94	2.45	0.51	26.5
$\mathbf{J_{sc}}$**(mA/m²)**	7.74	9.79	2.05	26.5
Fill Factor (%)	81.04	79.05	-1.99	-2.5
$\mathbf{P_{max}}$**(mW)**	4.05	5.03	0.98	24.1

When examining the performance figures more closely it becomes even more clear that the siloxane coated C5 and C6 are matching the values of the reference cell C2 almost exactly.

4.2.4 The $MgF_2/Al_2O_3/TiO_2$ Triple Layer Anti-Reflective Coating

The triple layer AR coating of $MgF_2/Al_2O_3/TiO_2$ comes closest to smoothly grading the refractive index from air to the refractive index of AlInP window like a graded index layer. Although the change in this case is more step-graded than a smooth curve. Two MJSCs were coated with this triple layer AR coating, namely C9 and C10, and the coating's layer structure is presented in table 4.13.

Table 4.13 The structure of the optimized triple AR coating of $MgF_2/Al_2O_3/TiO_2$.

C9, C10	
Materials	**Layer Thickness (nm)**
MgF_2	76
Al_2O_3	39
TiO_2	50

The fabrication of a triple layer coating requires one additional manufacturing step, which increases the required time and adds the complexity of the process. If the improvement is considerable, the extra step pays itself off. In fig. 4.46 is presented the reflectance of the coating.

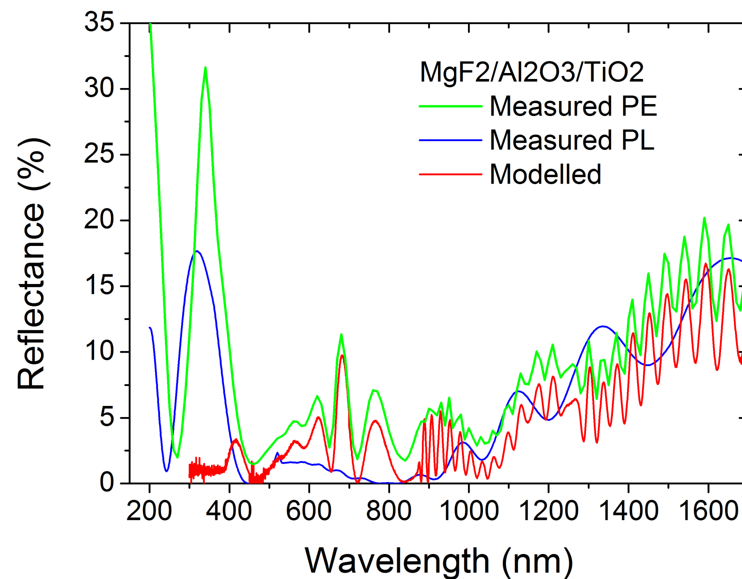

Figure 4.46 Reflectance of the $MgF_2/Al_2O_3/TiO_2$ AR coating on MJSCs and the modeled reflectance from Essential Macleod.

The reflectance peak at the UV range is somewhat shorter and narrower than other coatings in this thesis have and the overall reflectance is also lower than for the rest. These matters already confirms that testing the adding of a third layer paid off. The I-V characteristics of the cells C9 and C10 are presented in fig. 4.47

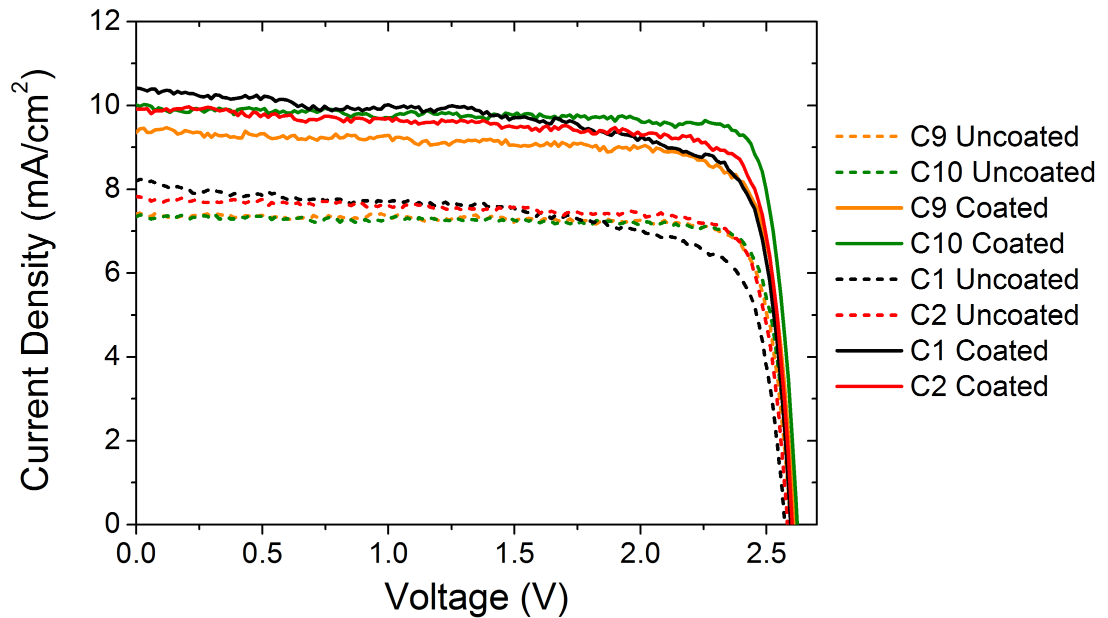

Figure 4.47 *The IV-curves of MJSCs before and after $MgF_2/Al_2O_3/TiO_2$ AR coating.*

The I-V curves reveal that the cell C9 has not performed as well as the C10. The cell C10 had worse starting current than either of the reference cells and with the triple layer AR coating it rose to be the best of these three. In table 4.14 is listed the performance values of the C9 and C10.

Table 4.14 *Results of the I-V performance for cells C9and C10 with$MgF_2/Al_2O_3/TiO_2$ AR coating.*

Sample ID	C9			
	No AR	With AR	Change	Percentual Change (%)
Efficiency (%)	16.09	19.63	3.54	22.0
V_{oc}(V)	2.60	2.61	0.01	0.5
I_{sc}(mA)	1.84	2.34	0.50	27.0
J_{sc}(mA/m^2)	7.37	9.36	1.99	26.9
Fill Factor (%)	84.05	80.39	-3.66	-4.4
P_{max}(mW)	4.02	4.91	0.88	22.0
Sample ID	C10			
	No AR	With AR	Change	Percentual Change (%)
Efficiency (%)	16.18	22.16	5.97	36.9
V_{oc}(V)	2.60	2.62	0.02	0.7
I_{sc}(mA)	1.84	2.49	0.65	35.3
J_{sc}(mA/m^2)	7.35	9.94	2.59	35.2
Fill Factor (%)	84.55	84.98	0.43	0.5
P_{max}(mW)	4.05	5.54	1.49	36.9

The cell C9 performs below the average performance of all the tested cells. From the fill factor one can see that something has changed, although it does not have any signs of a current leakage in its I-V curve. The C10, however, does an excellent job in its current-voltage behavior and offers the largest current density of the used test cells.

4.2.5 Comparison of the different Anti-reflective Designs

When the solar cells were not yet coated with AR coatings, their I-V curves looked pretty much the same, when excluding the three leaking cells (C1, C3 and C7). Now when combining the curves again in the same graph 4.48 there are some differences to be noted. The reference cell C11, that was not coated with AR coating has remained in the same magnitude.

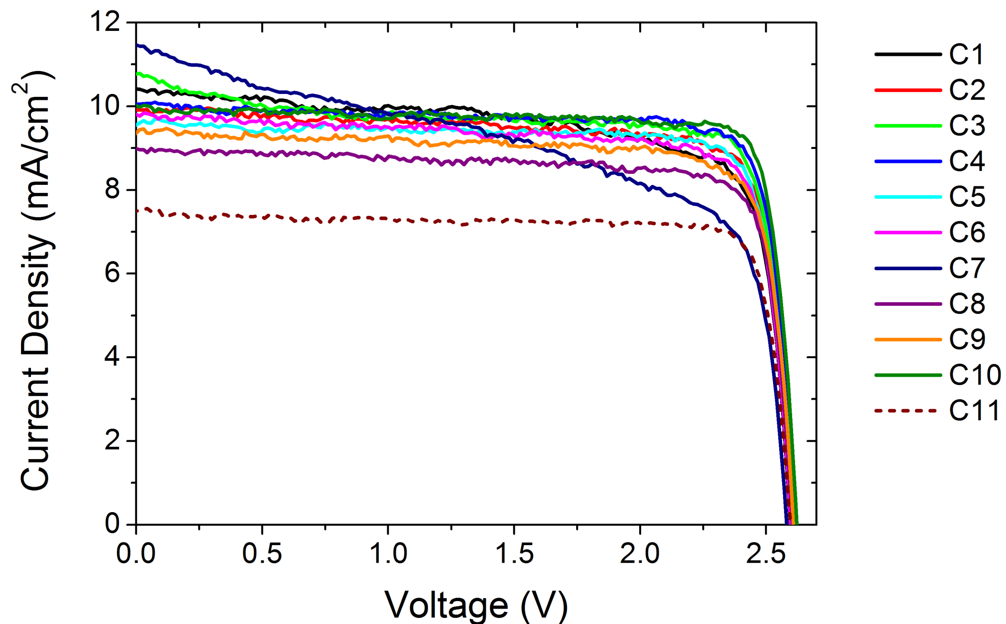

Figure 4.48 *The IV-curves of all the MJSCs after AR coatings and of the reference cell C11.*

It is clear that every AR coating has improved the cell's performance, so it's safe to say that almost any AR coating is better than no coating at all. From the graph it might be difficult to spot it but the best performance is gained with the triple layer AR with cell C10. Well earned second place is held by the nanoporous SiO_2 AR coatings as they both perform over the average of them all. The differences in I-V behavior should be traceable to the reflectances of the coatings, so in fig. 4.49 there is shown the reflectances of all the different coatings measured with PL

mapper. It is hard to interpret any proper causes for the different I-V behaviors, especially when the UV range is not visible at this scale.

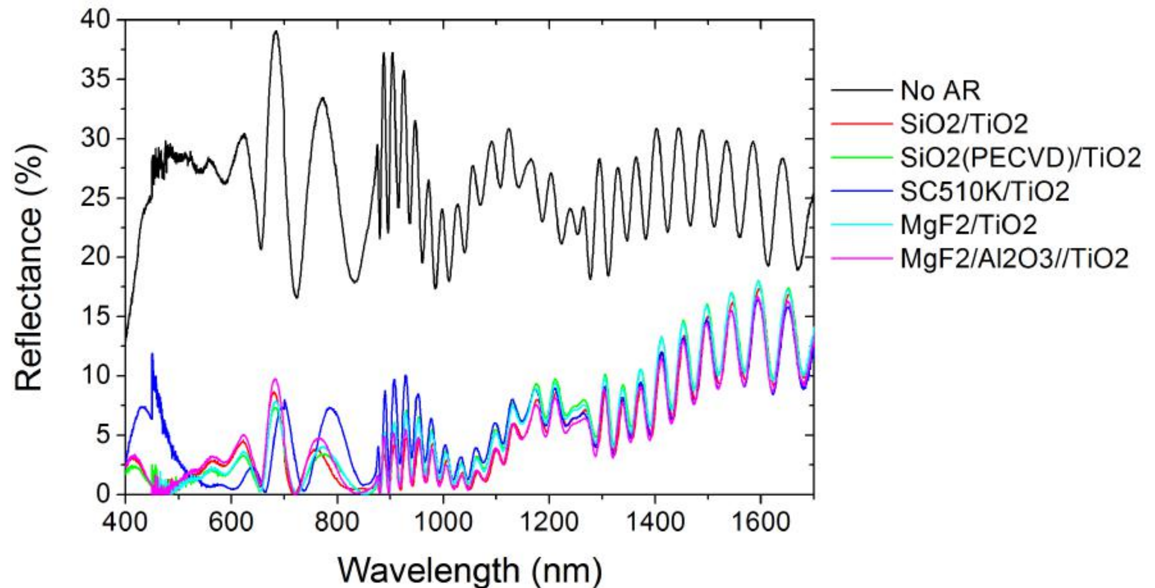

Figure 4.49 *Reflectances of the AR coatings on MJSCs and reflectance of the MJSC without any AR coating measured with PL mapper.*

As it was mentioned in section 3.2.1 the PL mapper cannot accurately measure the reflectance below 500 nm wavelength and on the other hand the detector's range reaches only up to 1700 nm or so. Thus the range for InGaP subcells is not visible and that complicates overall comparison between AR coatings. This is why also PerkinElmer spectrophotometer measurements were made and compared to these measured with PL mapper. In fig. 4.50 there is gathered the spectrophotometer reflectance measurement of all the coating designs. As could be seen in the comparisons of each individual AR coating's reflectance curves, the reflectances measured with PL mapper and PerkinElmer differ only few per cents, which can be deduced to be caused by the scattering that is neglected in PL mapper measurements. Otherwise the curves follow each others excellently and would indicate that our measurements are consistent and reliable. The difference between the PL curve and PE curve of the reflectances, varied between different coatings. The MgF_2 coatings for example had the lowest gap between PL curve and the PE curve and the SC510K coating had largest. This corresponds well with surface roughnesses measured with the AFM, as the chosen MgF_2 deposited at 200 ° had roughness average of $ra = 0.44$ nm and nanoporous SiO_2 had $ra = 2.3$ nm and the siloxane SC510K as the roughest one had $ra = 8.3$ nm. If the scattering effect truly is almost 2 % of the incoming light at some wavelengths, its contribution to the efficiency of the solar cells starts to be formidable.

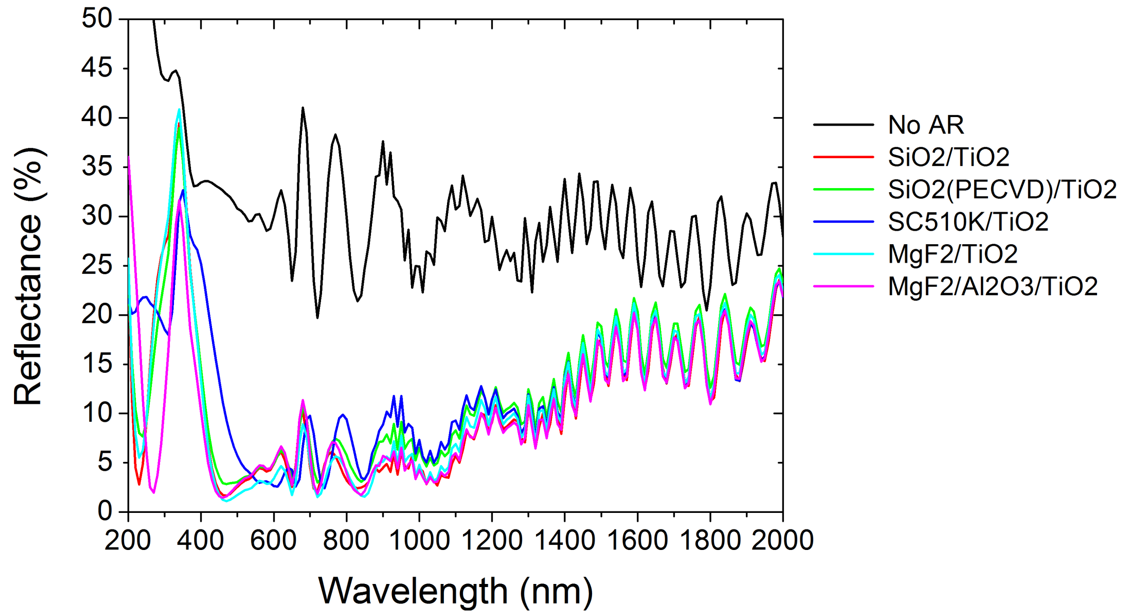

Figure 4.50 *Similar reflectance curves than in fig. 4.49, but measured with PerkinElmer spectrophotometer.*

In comparison of these reflectance curves one can see that the triple layer AR coatings reflectance at the UV range is the narrowest peak that is almost 10 % lower than the rest, except the siloxane coating which has low but broad reflectance peak at the UV bandwidth. Otherwise the differences in solar cells' I-V performances have to be explained due other factors as the reflectances are very similar.

In table 4.15 I have gathered the current limiting factors measured with the set-up described in section 3.2.4. Here it can be seen that no bigger differences arise between different AR coatings. The siloxane coating on C5 and the magnesium fluoride titania coating are the least functioning of these five, but as it was concluded in the section 4.2.1 in the case of MgF_2/TiO_2 coating most probably the cell in question is damaged during the coating process and the I-V behavior does not match to the coatings actual quality. With the siloxane coating the processing optimization with our research instrumentation requires more work to form more uniform coatings. Otherwise the cells' I-V performances were quite similar in relation to the limiting current behavior, as would be expected.

Table 4.15 *Limiting factors of the solar cell junctions with different AR coatings.*

Sample ID	**J_{SC} InGaP (mA/cm^2)**	**J_{SC} GaAs (mA/cm^2)**	**J_{SC} GaInNAsSb (mA/cm^2)**
C2	9.9	15.9	17.2
C3	10.0	15.5	16.4
C5	9.6	15.0	15.9
C8	9.0	15.6	16.6
C10	9.9	15.8	16.1

It is obvious by comparing the measured reflectances in fig. 4.50 and the current limiting factors of each subcell with different AR coatings in table 4.15, that the way to increase the efficiency is to shift the minimum reflectance furthermore to the UV range, as the InGaP cell limits the function of the whole MJSC. The current density difference between InGaP and the two other cells is over 5 mA/cm^2 with every design, so there is definitely room for improvement. An overall picture of the improvement of the solar cells' conversion efficiencies by AR coatings is presented in fig. 4.51.

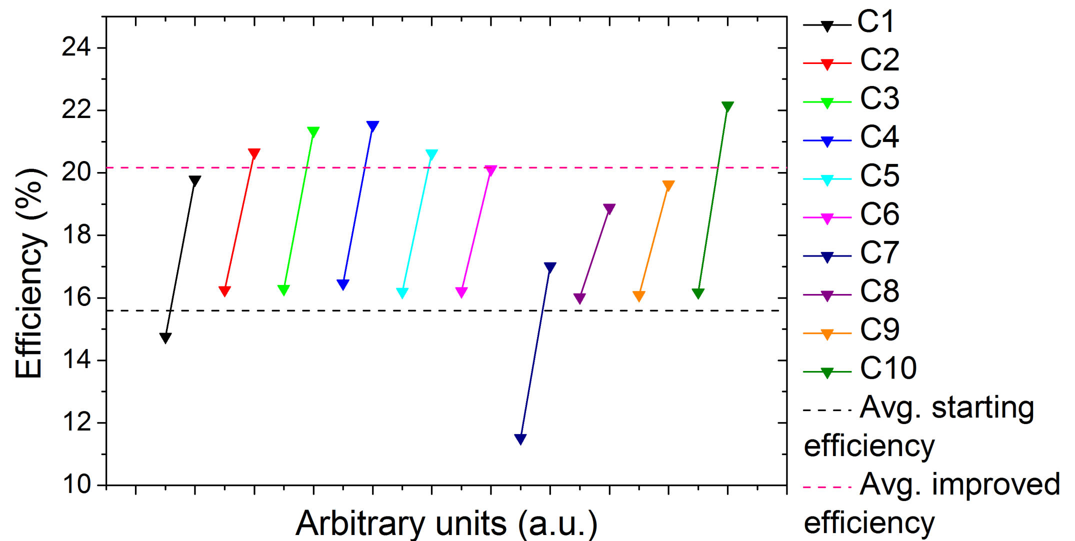

Figure 4.51 *Comparison graph for efficiency improvements for each solar cell and AR coating.*

Although the improvement of efficiencies was not the main goal of this thesis, they provide a nice overview of the solar cells' performance with and without AR coatings. Addition to that one can see with a quick glance how the different designs scaled against one another.

5. Conclusions

The main focus of this thesis was to optimize manufacturing and testing of different AR coatings for MJSC and see how they behave in accordance to standard SiO_2/TiO_2 double layer coating used previously. The emphasis lay on optimization of several dielectric deposition processes, namely EBE deposited MgF_2, PECVD deposited nanoporous SiO_2 and spinnable siloxane coatings SC510K and SC800i. Using the material data obtained from the ellipsometric measurements and microscopical examinations, four different AR coatings were designed and optimized with Essential Macleod thin film filter simulation program. The coatings were MgF_2 and TiO_2 double layer, nanoporous SiO_2 with TiO_2, the spinnable thin film SC510K as a double layer structure with TiO_2, and finally a triple layer coating consisting of MgF_2, Al_2O_3 and TiO_2.

The characterization of MgF_2 proved that the material is suitable for AR coating low index layer, as it has proper mechanical and optical properties. It was noted that the substrate temperature affects the dispersion curve of the film and by film comparison the deposition temperature for the AR coating was chosen to be 200 °C, although the temperature of 150 °C was a considerable candidate as well and was not totally ruled out as a future option. With PECVD deposited SiO_2 the emphasis was to lower the refractive index by porosity, that can be adjusted with deposition temperature and the precursor gas ratio. The lowest refractive index with SiO_2 was equivalent to the average MgF_2 film and addition to that the PECVD deposited SiO_2 might also have a passivation effect on the facets of the solar cells, which further improves its suitability for AR coating. The porous structure is not mechanically as durable as a dense film, which has to taken into account when designing a coating. With both of the siloxane coatings, SC510K and SC800i, there were some characterization issues, as the monochromatic ellipsometer could not provide refractive index and thickness data of these samples. The SC510K, however, was proven to be an easy to use and effective coating, with TiO_2 as the high index layer. Both coatings require process optimization, as they seem very promising materials and the easy to use spin coating method is a definite positive side. A good development direction would be to combine a siloxane coating and surface texturing by lithography.

All the fabricated AR coatings proved themselves suitable for MJSC's coating applications and with the acquired material data the coating structures can further be optimized for different kinds of MJSCs. A positive surprise was how well the nanoporous SiO_2 AR coating functioned and that the somewhat not-process-optimized siloxane AR coating functioned as well as the reference SiO_2/TiO_2. Unfortunately, the two solar cells that were coated with MgF_2/TiO_2, were damaged during the processing and I-V comparison to the other cells was not reliable. The reflectance spectrum of MgF_2/TiO_2 proved, however, that the design functioned as it should have, so new tests are expected to deliver presumed results in term of cell operation. One aspect to further the coating designs is to change the TiO_2 to Ta_2O_5, as tantalum pentoxide has lower absorption in the UV range than TiO_2 [13], which is a significant factor when the solar cell are designed for space application.

Recommendable experiments after these results would be to continue working with MgF_2 as the lower index material and to change TiO_2 to Ta_2O_5 for high index material. By optimizing this structure and a triple layer coating of $MgF_2/Al_2O_3/Ta_2O_5$ that can improve current-matching possibilities due to including the low UV reflectance, one could produce high-performance AR coatings to CPV and space applications. Also continuing the flow ratio study with PECVD SiO_2, would be profitable, for finding a fitting compromise between porosity and mechanical durability. Further process optimizing for siloxanes SC510K and SC800i would be in order, after which they could possibly provide standalone applications as solar cell coatings.

Bibliography

[1] H. A. Macleod, *Thin-Film Optical Filters.* CRC Press, 4 ed., 2010.

[2] H. K. Pulker, "Characterization of optical thin films," *Appl. Opt.*, vol. 18, pp. 1969–1977, Jun 1979.

[3] D. C. Leslie, A. Waterhouse, J. B. Berthet, T. M. Valentin, A. L. Watters, A. Jain, P. Kim, B. D. Hatton, A. Nedder, K. Donovan, E. H. Super, C. Howell, C. P. Johnson, T. L. Vu, D. E. Bolgen, S. Rifai, A. R. Hansen, M. Aizenberg, M. Super, J. Aizenberg, and D. E. Ingber, "A bioinspired omniphobic surface coating on medical devices prevents thrombosis and biofouling," *Nature Biotechnology*, vol. 32, pp. 1134–1140, Oct 2014.

[4] L. Wang and T. J. McCarthy, "Covalently Attached Liquids: Instant Omniphobic Surfaces with Unprecedented Repellency," *Angewandte Chemie International Edition*, vol. 55, no. 1, pp. 244–248, 2016.

[5] D. J. Aiken, "Antireflection coating design for series interconnected multijunction solar cells," *Progress in Photovoltaics: Research and Applications*, vol. 8, no. 6, pp. 563–570, 2000.

[6] H. K. Raut, V. A. Ganesh, A. S. Nair, and S. Ramakrishna, "Anti-reflective coatings: A critical, in-depth review," *Energy Environ. Sci.*, vol. 4, pp. 3779–3804, 2011.

[7] S. L. Diedenhofen, G. Grzela, E. Haverkamp, G. Bauhuis, J. Schermer, and J. G. Rivas, "Broadband and omnidirectional anti-reflection layer for III/V multi-junction solar cells," *Solar Energy Materials and Solar Cells*, vol. 101, pp. 308 – 314, 2012.

[8] A. Aho, J. Tommila, A. Tukiainen, V. Polojärvi, T. Niemi, and M. Guina, "Moth eye antireflection coated GaInP/GaAs/GaInNAs solar cell," *AIP Conference Proceedings*, vol. 1616, no. 1, pp. 33–36, 2014.

[9] "Renewables 2016 Global Status Report." http://www.ren21.net/status-of-renewables/global-status-report/. [Online; accessed September 20, 2016].

[10] M. A. Green, K. Emery, Y. Hishikawa, W. Warta, and E. D. Dunlop, "Solar cell efficiency tables (Version 45)," *Progress in Photovoltaics: Research and Applications*, vol. 23, no. 1, pp. 1–9, 2015. PIP-14-274.

[11] A. L. Luque and A. Viacheslav, *Concentrator Photovoltaics*. Springer, 1 ed., 2007.

[12] A. McEvoy, L. Castañer, and T. Markvart, eds., *Solar Cells (Second Edition)*. Elsevier, second edition ed., 2013.

[13] C. E. Valdivia, E. Desfonds, D. Masson, S. Fafard, A. Carlson, J. Cook, T. J. Hall, and K. Hinzer, "Optimization of antireflection coating design for multijunction solar cells and concentrator systems," 2008.

[14] P. H. Holloway and G. E. McGuire, *Handbook of Compound Semiconductors Growth, Processing, Characterization, and Devices*. Noyes Publications, 1 ed., 1995.

[15] E. Hecht, *Optics*. Addison Wesley, 4 ed., 2002.

[16] H. G. Tompkins and E. A. Irene, *Handbook of Ellipsometry*. William Andrew, Inc., 1 ed., 2005.

[17] K. Seshan, *Handbook of Thin Film Deposition*. Elsevier Inc., 3 ed., 2012.

[18] I. P. Herman, *Optical Diagnostics for Thin Film Processing*. Academic Press, Inc., 1 ed., 1996.

[19] A. Einstein, "'Uber einen die erzeugung und verwandlung des lichtes betreffenden heuristischen gesichtspunkt," *Annalen der Physik*, vol. 17, pp. 132–148, 1905.

[20] B. Saleh and M. Teich, *Fundamentals of Photonics*. John Wiley & Sons, Inc., 2 ed., 2007.

[21] "File:EM spectrum.svg." https://commons.wikimedia.org/wiki/File:EM_spectrum.svg. [Online; accessed June 15, 2016.

[22] M. Born and E. Wolf, *Principles of Optics*. Cambridge University Press, 7 ed., 1999.

[23] M. Fox, *Optical Properties of Solids.* Oxford University Press, 2 ed., 2010.

[24] D. R. Smith, J. B. Pendry, and M. C. K. Wiltshire, "Metamaterials and Negative Refractive Index," *Science*, vol. 305, no. 5685, pp. 788–792, 2004.

[25] J. Valentine, S. Zhang, T. Zentgraf, E. Ulin-Avila, D. A. Genov, G. Bartal, and X. Zhang, "Three-dimensional optical metamaterial with a negative refractive index," *Nature*, vol. 455, pp. 376–379, August 2008.

[26] A. Goswami, S. Aravindan, P. Rao, and M. Yoshino, "Structured Surfaces for Generation of Negative Index of Refraction," *Critical Reviews in Solid State and Materials Sciences*, vol. 41, no. 5, pp. 367–385, 2016.

[27] Z. Knittl, *Optics of Thin Films.* John Wiley & Sons, Ltd., 1 ed., 1976.

[28] L. Vaissie, O. V. Smolski, A. Mehta, and E. G. Johnson, "High efficiency surface-emitting laser with subwavelength antireflection structure," *IEEE Photonics Technology Letters*, vol. 17, pp. 732–734, April 2005.

[29] H. Weiss, "Physics and technology of data storage," *Solid-State Electronics*, vol. 19, no. 5, pp. 347 – 356, 1976.

[30] T. Okuno, "Development of Subwavelength Structure Coating (SWC) and its Application to Imaging Lenses," in *International Optical Design Conference and Optical Fabrication and Testing*, p. IMA2, Optical Society of America, 2010.

[31] M. Mildebrath and K. Klemm, "Ophthalmic optical coatings: the real world can be more aggressive than you think," 2006.

[32] Y. M. Song, E. S. Choi, G. C. Park, C. Y. Park, S. J. Jang, and Y. T. Lee, "Disordered antireflective nanostructures on GaN-based light-emitting diodes using Ag nanoparticles for improved light extraction efficiency," *Applied Physics Letters*, vol. 97, no. 9, 2010.

[33] H. K. Raut, A. S. Nair, S. S. Dinachali, V. A. Ganesh, T. M. Walsh, and S. Ramakrishna, "Porous SiO2 anti-reflective coatings on large-area substrates by electrospinning and their application to solar modules," *Solar Energy Materials and Solar Cells*, vol. 111, pp. 9 – 15, 2013.

[34] L. Remache, E. Fourmond, A. Mahdjoub, J. Dupuis, and M. Lemiti, "Design of porous silicon/PECVD SiOx antireflection coatings for silicon solar cells," *Materials Science and Engineering: B*, vol. 176, no. 1, pp. 45 – 48, 2011.

[35] L. Schirone, G. Sotgiu, and F. Califano, "Chemically etched porous silicon as an anti-reflection coating for high efficiency solar cells," *Thin Solid Films*, vol. 297, no. 1–2, pp. 296 – 298, 1997.

[36] A. Jain, S. Rogojevic, W. N. Gill, J. L. Plawsky, I. Matthew, M. Tomozawa, and E. Simonyi, "Effects of processing history on the modulus of silica xerogel films," *Journal of Applied Physics*, vol. 90, no. 11, pp. 5832–5834, 2001.

[37] J.-Q. Xi, M. Ojha, W. Cho, J. L. Plawsky, W. N. Gill, T. Gessmann, and E. F. Schubert, "Omnidirectional reflector using nanoporous SiO2 as a low-refractive-index material," *Opt. Lett.*, vol. 30, pp. 1518–1520, Jun 2005.

[38] A. K. Sood, G. Pethuraja, A. W. Sood, R. E. Welser, Y. R. Puri, J. Cho, E. F. Schubert, N. K. Dhar, P. Wijewarnasuriya, and M. B. Soprano, "Development of large area nanostructure antireflection coatings for EO/IR sensor applications," 2012.

[39] J.-Q. Xi, M. F. Schubert, J. K. Kim, E. F. Schubert, M. Chen, S.-Y. Lin, W. Liu, and J. A. Smart, "Optical thin-film materials with low refractive index for broadband elimination of Fresnel reflection," *Nature Photonics*, vol. 1, pp. 176–179, March 2007.

[40] X. A. Zhang, A. Bagal, E. C. Dandley, J. Zhao, C. J. Oldham, B.-I. Wu, G. N. Parsons, and C.-H. Chang, "Ordered 3D Thin-Shell Nanolattice Materials with Near-Unity Refractive Indices," *Advanced Functional Materials*, vol. 25, no. 42, pp. 6644–6649, 2015.

[41] O. S. Heavens, "Optical properties of thin films," *Reports on Progress in Physics*, vol. 23, no. 1, p. 1, 1960.

[42] J. D. T. Kruschwitz and W. T. Pawlewicz, "Optical and durability properties of infrared transmitting thin films," *Appl. Opt.*, vol. 36, pp. 2157–2159, Apr 1997.

[43] J. R. DeVore, "Refractive Indices of Rutile and Sphalerite," *J. Opt. Soc. Am.*, vol. 41, pp. 416–419, Jun 1951.

[44] L. Gao, F. Lemarchand, and M. Lequime, "Exploitation of multiple incidences spectrometric measurements for thin film reverse engineering," *Opt. Express*, vol. 20, pp. 15734–15751, Jul 2012.

[45] H. R. Philipp, "Optical properties of silicon nitride," *J. Electrochim. Soc.*, vol. 120, pp. 295–300, Jan 1973.

[46] I. H. Malitson, "Refraction and Dispersion of Synthetic Sapphire," *J. Opt. Soc. Am.*, vol. 52, pp. 1377–1379, Dec 1962.

[47] I. H. Malitson, "Interspecimen Comparison of the Refractive Index of Fused Silica∗,†," *J. Opt. Soc. Am.*, vol. 55, pp. 1205–1209, Oct 1965.

[48] M. J. Dodge, "Refractive properties of magnesium fluoride," *Appl. Opt.*, vol. 23, pp. 1980–1985, Jun 1984.

[49] T. Chuen-Lin, L. Tsai-Wei, T. Hung-Da, J. Yi-Jun, and L. Ming-Chung, "Temperature-dependent optical and mechanical properties of obliquely deposited MgF2 thin films ," *Indian Journal of Pure & Applied Physics*, vol. 52, pp. 117–123, February 2014.

[50] L. Dumas, E. Quesnel, J.-Y. Robic, and Y. Pauleau, "Characterization of magnesium fluoride thin films deposited by direct electron beam evaporation," *Journal of Vacuum Science & Technology A*, vol. 18, no. 2, pp. 465–469, 2000.

[51] C.-C. Jaing, M.-H. Shiao, C.-C. Lee, C.-J. Lu, M.-C. Liu, C.-H. Lee, and H.-C. Chen, "Effects of Ion Assistance and Substrate Temperature on Optical Characteristics and Microstructure of MgF 2 Films Formed by Electron-Beam Evaporation," *Japanese Journal of Applied Physics*, vol. 45, no. 6R, p. 5027, 2006.

[52] M. Alvisi, F. De Tomasi, A. Della Patria, M. Di Giulio, E. Masetti, M. R. Perrone, M. L. Protopapa, and A. Tepore, "Ion assistance effects on electron beam deposited MgF2 films," *Journal of Vacuum Science & Technology A*, vol. 20, no. 3, pp. 714–720, 2002.

[53] M.-C. Liu, C.-C. Lee, M. Kaneko, K. Nakahira, and Y. Takano, "Microstructure of magnesium fluoride films deposited by boat evaporation at 193 nm," *Appl. Opt.*, vol. 45, pp. 7319–7324, Oct 2006.

[54] K. ichi Nagata, "Inhomogeneity in Refractive Index of Evaporated MgF 2 Film," *Japanese Journal of Applied Physics*, vol. 7, no. 10, p. 1181, 1968.

[55] J. Sun, J. Shao, K. Yi, and W. Zhang, "Effects of substrate temperatures on the characterization of magnesium fluoride thin films in deep-ultraviolet region," *Appl. Opt.*, vol. 53, pp. 1298–1305, Mar 2014.

[56] R.-Y. Tsai, S.-C. Shiau, C.-H. Lee, F. C. Ho, and M.-Y. Hua, "Properties of optical thin films and coatings prepared by reactive electron-beam deposition with and without ion bombardments," *Optical Engineering*, vol. 36, no. 12, pp. 3433–3438, 1997.

[57] L. Dumas, E. Quesnel, J.-Y. Robic, and Y. Pauleau, “Characterization of magnesium fluoride thin films produced by argon ion beam-assisted deposition,” *Thin Solid Films*, vol. 382, no. 1–2, pp. 61 – 68, 2001.

[58] K. Kawamata, T. Shouzu, and N. Mitamura, “K-M-S (keep-molecules sputtering) deposition of optical MgF2 thin films,” *Vacuum*, vol. 51, no. 4, pp. 559 – 564, 1998.

[59] D. Ristau, S. Günster, S. Bosch, A. Duparré, E. Masetti, J. Ferré-Borrull, G. Kiriakidis, F. Peiró, E. Quesnel, and A. Tikhonravov, “Ultraviolet optical and microstructural properties of MgF2 and LaF3 coatings deposited by ion-beam sputtering and boat andelectron-beam evaporation,” *Appl. Opt.*, vol. 41, pp. 3196–3204, Jun 2002.

[60] L. Dumas, E. Quesnel, F. Pierre, and F. Bertin, “Optical properties of magnesium fluoride thin films produced by argon ion-beam assisted deposition,” *Journal of Vacuum Science & Technology A*, vol. 20, no. 1, pp. 102–106, 2002.

[61] J. I. Larruquert and R. A. Keski-Kuha, “Far ultraviolet optical properties of MgF2 films deposited by ion-beam sputtering and their application as protective coatings for Al ,” *Optics Communications*, vol. 215, no. 1–3, pp. 93 – 99, 2003.

[62] T. Pilvi, T. Hatanpaa, E. Puukilainen, K. Arstila, M. Bischoff, U. Kaiser, N. Kaiser, M. Leskela, and M. Ritala, “Study of a novel ALD process for depositing MgF2 thin films,” *J. Mater. Chem.*, vol. 17, pp. 5077–5083, 2007.

[63] S. Lee, S. Choi, and J. Yi, “Double-layer anti-reflection coating using MgF2 and CeO2 films on a crystalline silicon substrate,” *Thin Solid Films*, vol. 376, no. 1–2, pp. 208 – 213, 2000.

[64] H. Yu, H. Qi, Y. Cui, Y. Shen, J. Shao, and Z. Fan, “Influence of substrate temperature on properties of MgF_2 coatings,” *Applied Surface Science*, vol. 253, no. 14, pp. 6113 – 6117, 2007.

[65] G. Atanassov, J. Turlo, J. K. Fu, and Y. S. Dai, “Mechanical, optical and structural properties of TiO2 and MgF2 thin films deposited by plasma ion assisted deposition,” *Thin Solid Films*, vol. 342, no. 1–2, pp. 83 – 92, 1999.

[66] S. Ogura, N. Sugawara, and R. Hiraga, “Refractive index and packing density for MgF2 films: Correlation of temperature dependence with water sorption,” *Thin Solid Films*, vol. 30, no. 1, pp. 3 – 10, 1975.

[67] H. Pulker and E. Jung, "Correlation between film structure and sorption behaviour of vapour deposited ZnS, cryolite and MgF2 films," *Thin Solid Films*, vol. 9, no. 1, pp. 57 – 66, 1972.

[68] E. Ritter and R. Hoffmann, "Influence of Substrate Temperature on the Condensation of Vacuum Evaporated Films of MgF2 and ZnS," *Journal of Vacuum Science & Technology*, vol. 6, no. 4, pp. 733–736, 1969.

[69] A. Fujishima, X. Zhang, and D. A. Tryk, "TiO2 photocatalysis and related surface phenomena," *Surface Science Reports*, vol. 63, no. 12, pp. 515 – 582, 2008.

[70] U. Diebold, "The surface science of titanium dioxide," *Surface Science Reports*, vol. 48, no. 5–8, pp. 53 – 229, 2003.

[71] H. Selhofer, E. Ritter, and R. Linsbod, "Properties of titanium dioxide films prepared by reactive electron-beam evaporation from various starting materials," *Appl. Opt.*, vol. 41, pp. 756–762, Feb 2002.

[72] T. Amotchkina, M. K. Trubetskov, A. V. Tikhonravov, I. Angelov, and V. Pervak, "Reliable Characterization of e-beam Evaporated TiO₂ Films," in *Optical Interference Coatings*, p. FA.6, Optical Society of America, 2013.

[73] Y. Leprince-Wang and K. Yu-Zhang, "Study of the growth morphology of TiO2 thin films by {AFM} and {TEM}," *Surface and Coatings Technology*, vol. 140, no. 2, pp. 155 – 160, 2001.

[74] M. Colgan, B. Djurfors, D. Ivey, and M. Brett, "Effects of annealing on titanium dioxide structured films," *Thin Solid Films*, vol. 466, no. 1–2, pp. 92 – 96, 2004.

[75] C. Martinet, V. Paillard, A. Gagnaire, and J. Joseph, "Deposition of SiO2 and TiO2 thin films by plasma enhanced chemical vapor deposition for antireflection coating," *Journal of Non-Crystalline Solids*, vol. 216, pp. 77 – 82, 1997.

[76] D. Mergel, D. Buschendorf, S. Eggert, R. Grammes, and B. Samset, "Density and refractive index of TiO2 films prepared by reactive evaporation," *Thin Solid Films*, vol. 371, no. 1–2, pp. 218 – 224, 2000.

[77] Y.-Q. Hou, D.-M. Zhuang, G. Zhang, M. Zhao, and M.-S. Wu, "Influence of annealing temperature on the properties of titanium oxide thin film," *Applied Surface Science*, vol. 218, no. 1–4, pp. 98 – 106, 2003.

[78] D. Mardare, "Optical constants of heat-treated TiO2 thin films ," *Materials Science and Engineering: B*, vol. 95, no. 1, pp. 83 – 87, 2002.

[79] D. Hoffman and D. Leibowitz, "Al2O3 Films Prepared by Electron-Beam Evaporation of Hot-Pressed Al2O3 in Oxygen Ambient," *Journal of Vacuum Science & Technology*, vol. 8, no. 1, pp. 107–111, 1971.

[80] K. Shamala, L. Murthy, and K. N. Rao, "Studies on optical and dielectric properties of Al2O3 thin films prepared by electron beam evaporation and spray pyrolysis method," *Materials Science and Engineering: B*, vol. 106, no. 3, pp. 269 – 274, 2004.

[81] T. Maruyama and T. Nakai, "Aluminum oxide thin films prepared by chemical vapor deposition from aluminum 2-ethylhexanoate," *Applied Physics Letters*, vol. 58, no. 19, pp. 2079–2080, 1991.

[82] M. Aguilar-Frutis, M. Garcia, C. Falcony, G. Plesch, and S. Jimenez-Sandoval, "A study of the dielectric characteristics of aluminum oxide thin films deposited by spray pyrolysis from al(acac)3," *Thin Solid Films*, vol. 389, no. 1–2, pp. 200 – 206, 2001.

[83] M. S. Al-Robaee, G. Subbanna, K. N. Rao, and S. Mohan, "Studies of the optical and structural properties of ion-assisted deposited Al2O3 thin films," *Vacuum*, vol. 45, no. 1, pp. 97 – 102, 1994.

[84] G. Lucovsky, P. D. Richard, D. V. Tsu, S. Y. Lin, and R. J. Markunas, "Deposition of silicon dioxide and silicon nitride by remote plasma enhanced chemical vapor deposition," *Journal of Vacuum Science & Technology A*, vol. 4, no. 3, pp. 681–688, 1986.

[85] H. Nagel, A. G. Aberle, and R. Hezel, "Optimised antireflection coatings for planar silicon solar cells using remote PECVD silicon nitride and porous silicon dioxide," *Progress in Photovoltaics: Research and Applications*, vol. 7, no. 4, pp. 245–260, 1999.

[86] J. Batey and E. Tierney, "Low temperature deposition of high-quality silicon dioxide by plasma-enhanced chemical vapor deposition," *Journal of Applied Physics*, vol. 60, no. 9, pp. 3136–3145, 1986.

[87] M. R. Amirzada, A. Tatzel, V. Viereck, and H. Hillmer, "Surface roughness analysis of SiO2 for PECVD, PVD and IBD on different substrates," *Applied Nanoscience*, vol. 6, no. 2, pp. 215–222, 2016.

[88] A. Prasad, S. Balakrishnan, S. K. Jain, and G. C. Jain, "Porous silicon oxide anti-reflection coating for solar cells for solar cells," *J. Electrochem. Soc.*, vol. 129, pp. 569–599, March 1982.

[89] "SC 500 Process Guidelines V2.0." http://pibond.com/en/products/product-lines/sc, 2016. Espoo, Finland.

[90] "SC 800i Process Guidelines V1.0." http://pibond.com/en/products/product-lines/sc, 2016. Espoo, Finland.

[91] "Pibond Oy." http://pibond.com/en, 2016. Espoo, Finland.

[92] "ChemSketch, version 15.01." www.acdlabs.com, 2016. Toronto, Canada.

[93] J. Lee, T. Tanaka, S. Sasaki, S. Uchiyama, M. Tsuchiya, and T. Kamiya, "Novel design procedure of broad-band multilayer antireflection coatings for optical and optoelectronic devices," *Journal of Lightwave Technology*, vol. 16, pp. 884–891, May 1998.

[94] Z. Jun-Chao, X. Li-Min, F. Ming, and H. Hong-Bo, "Wide-angle and broadband graded-refractive-index antireflection coatings," *Chinese Physics B*, vol. 22, no. 4, p. 044201, 2013.

[95] E. Becquerel, "On Electric Effects under the Influence of Solar Radiation," *Compt. Rend.*, vol. 9, p. 561, 1839.

[96] R. Ohl, "Light-sensitive electric device," June 1946. US Patent 2,402,662.

[97] M. Riordan and L. Hoddeson, "The origins of the pn junction," *IEEE Spectrum*, vol. 34, pp. 46–51, Jun 1997.

[98] S. Benzer, "Excess-Defect Germanium Contacts," *Phys. Rev.*, vol. 72, pp. 1267–1268, Dec 1947.

[99] J. I. Pantchechnikoff, "A Large Area Germanium Photocell," *Review of Scientific Instruments*, vol. 23, no. 3, pp. 135–135, 1952.

[100] D. M. Chapin, C. S. Fuller, and G. L. Pearson, "A New Silicon p-n Junction Photocell for Converting Solar Radiation into Electrical Power," *Journal of Applied Physics*, vol. 25, no. 5, pp. 676–677, 1954.

[101] D. C. Reynolds, G. Leies, L. L. Antes, and R. E. Marburger, "Photovoltaic Effect in Cadmium Sulfide," *Phys. Rev.*, vol. 96, pp. 533–534, Oct 1954.

[102] S. M. Sze and K. K. Ng, *Physics of Semiconductor Devices*. John Wiley & Sons, Inc., 3 ed., 2006.

[103] X. Wei, H. Lee, and S. Choi, "Biopower generation in a microfluidic bio-solar panel," *Sensors and Actuators B: Chemical*, vol. 228, pp. 151 – 155, 2016.

[104] A. O. El-Ballouli, E. Alarousu, A. R. Kirmani, A. Amassian, O. M. Bakr, and O. F. Mohammed, "Overcoming the Cut-Off Charge Transfer Bandgaps at the PbS Quantum Dot Interface," *Advanced Functional Materials*, vol. 25, no. 48, pp. 7435–7441, 2015.

[105] D. R. Myers, K. Emery, and C. Gueymard, "Proposed reference spectral irradiance standards to improve concentrating photovoltaic system design and performance evaluation," in *Photovoltaic Specialists Conference, 2002. Conference Record of the Twenty-Ninth IEEE*, pp. 923–926, May 2002.

[106] J. Oh, H.-C. Yuan, and H. M. Branz, "An 18.2%-efficient black-silicon solar cell achieved through control of carrier recombination in nanostructures," *Nature Nanotechnology*, vol. 7, p. 743–748, 2012.

[107] M. A. Green, K. Emery, Y. Hishikawa, W. Warta, and E. D. Dunlop, "Solar cell efficiency tables (version 47)," *Progress in Photovoltaics: Research and Applications*, vol. 24, no. 1, pp. 3–11, 2016. PIP-15-272.

[108] "ASTM G173-03 Reference Spectra." http://rredc.nrel.gov/solar/spectra/am1.5/astmg173/astmg173.html. [Online; accessed June 15, 2016].

[109] C. N. Eisler, Z. R. Abrams, M. T. Sheldon, X. Zhang, and H. A. Atwater, "Multijunction solar cell efficiencies: effect of spectral window, optical environment and radiative coupling," *Energy Environ. Sci.*, vol. 7, pp. 3600–3605, 2014.

[110] V. Polojärvi, *Novel III-V Heterostructures for High Efficiency Solar Cells: Studies of Electrical and Optical Properties*. Tampere University of Techology. Publication, Tampere University of Technology, May 2016.

[111] M. Raappana, *Wet etching of dilute nitride and antimonide semiconductors for solar cells*. Tampere University of Technology, June 2015.

[112] "File:Amonix7700.jpg." https://commons.wikimedia.org/wiki/File:Amonix7700.jpg. [Online; accessed August 23, 2016].

[113] R. Levine, "Standard Operating Procedures: Electron Beam Evaporator, Version 1.6." https://www.engr.uky.edu/~cense/equipment/SOP/Standard%20Operating%20Procedures%20for%20Electron%20Beam%20Evaporator%201.6.pdf. [Online; accessed June 22, 2016].

[114] L. Martinu, O. Zabeida, and J. Klemberg-Sapieha, "Chapter 9 - Plasma-Enhanced Chemical Vapor Deposition of Functional Coatings," in *Handbook of Deposition Technologies for Films and Coatings (Third Edition)* (P. M. Martin, ed.), pp. 392 – 465, Boston: William Andrew Publishing, third edition ed., 2010.

[115] "Plasma Enhanced Chemical Vapour Deposition (PECVD)." https://www.oxford-instruments.com/products/etching-deposition-and-growth/plasma-etch-deposition/pecvd. [Online; accessed July 12, 2016].

[116] "Basic PECVD Plasma Processes (SiH4 based)." https://nanolab.berkeley.edu/process_manual/chap6/6.20PECVD.pdf. [Online; accessed July 12, 2016].

[117] H. Pulker, *Coatings on Glass*. Elsevier, 2 ed., 1999.

[118] *Essential Macleod Optical Coating Design Program - User's Manual, Version 8.11.* Thin Film Center Inc, 1999.

[119] M. Victoria, C. Domínguez, I. Antón, and G. Sala, "Antireflective coatings for multijunction solar cells under wide-angle ray bundles," *Opt. Express*, vol. 20, pp. 8136–8147, Mar 2012.

[120] "Ellipsometry Basics." http://www.sun-way.com.tw/Files/DownloadFile/Ellipsometry_basics.pdf. [Online; accessed June 22, 2016].

[121] "Rudolph Auto EL III Ellipsometer." http://ceas.uc.edu/cleanroom/equipment/Rudolph_Auto_Ellipsometer.html. [Online; accessed June 22, 2016].

[122] S. Upstone, "PerkinElmer Lambda X50 Series UV/Vis/NIR Spectrophotometer."

[123] H. H. Li, "Refractive index of alkaline earth halides and its wavelength and temperature derivatives," *Journal of Physical and Chemical Reference Data*, vol. 9, no. 1, pp. 161–290, 1980.

[124] "Optical Data from Sopra SA." http://www.sspectra.com/sopra.html. [Online; accessed July 21, 2016].

[125] "Reflectance Calculator." http://filmetrics.com/reflectance-calculator. [Online; accessed August 23, 2016].

[126] "NanoWizard® AFM Handbook Version 2.2a," 2012.

[127] R. Ahorinta, *Quick User Guide for Veeco Dimension 2100.* 2011.

[128] M. Adamov, B. Perović, and T. Nenadović, "Electrical and structural properties of thin gold films obtained by vacuum evaporation and sputtering," *Thin Solid Films*, vol. 24, no. 1, pp. 89 – 100, 1974.

[129] I. Horcas, R. Fernández, J. M. Gómez-Rodríguez, J. Colchero, J. Gómez-Herrero, and A. M. Baro, "WSXM: A software for scanning probe microscopy and a tool for nanotechnology," *REVIEW OF SCIENTIFIC INSTRUMENTS*, vol. 78, no. 013705, pp. 1–8, 2007.

[130] T. Lepistö, *Pyyhkäisyelektronimikroskopia ja Mikroanalysointi.* Juvenes Print, 1 ed., 2016.

[131] "ΣIGMA™ Field Emission Scanning Electron Microscope – Instruction Manual," 2011.

[132] "Class AAA Standard Solar Simulator." http://www.oainet.com/pdf/oai_AAA-solar-sim_brochure.pdf. [Online; accessed October 4, 2016].

[133] R. Isoaho, *Spectral and temperature dynamics of high-efficiency dilute nitride multijunction solar cells.* Tampere University of Technology, September 2016.

[134] "Magnesium Fluoride MgF2 for Optical Coating." https://materion.com/ResourceCenter/ProductData/InorganicChemicals/Fluorides/MagnesiumFluorideMgF2forOpticalCoating.aspx. [Online; accessed June 15, 2016].

[135] D. Gaspar, A. C. Pimentel, T. Mateus, J. S. J. P. Leitão, B. P. Falcão, A. Araújo, A. Vicente, S. A. Filonovich, H. Águas, R. Martins, and I. Ferreira, "Influence of the layer thickness in plasmonic gold nanoparticles produced by thermal evaporation," *Scientific Reports*, vol. 3, no. 1469, pp. 1–5, 2013.

A. Growth Parameter Tables

Growth parameter tables for the deposited samples. Most influental parameters of each substance according to their deposition method.

Table A.1 *Evaporation parameters used for EBE coating.*

Sample ID	Substance	Rate (nm/s)	T (°C)	p (mbar)	Current (mA)	Voltage (kV)
S1	MgF_2	0.3	50	$< 1 \cdot 10^{-4}$	6–10	8
S2	MgF_2	0.3	100	$< 1 \cdot 10^{-4}$	6–10	8
S3	MgF_2	0.3	150	$< 1 \cdot 10^{-4}$	6–10	8
S4	MgF_2	0.3	200	$< 1 \cdot 10^{-4}$	6–10	8
S5	MgF_2	0.3	240	$< 1 \cdot 10^{-4}$	6–10	8
S6	MgF_2	0.1	200	$< 1 \cdot 10^{-4}$	6–10	8
S7	MgF_2	0.5	200	$< 1 \cdot 10^{-4}$	6–10	8
S8	MgF_2	0.3	200	$< 1 \cdot 10^{-4}$	6–10	8
S8	TiO_2	0.1	200	$2.8 \cdot 10^{-4}$	72	9.5

Table A.2 *Deposition parameters used for PECVD coating.*

Sample ID	Substance	T (°C)	p (mTorr)	NO_2 gas flow (sccm)	2%SiH_4/N_2 gas flow (sccm)	RF (W)
S9	SiO_2	50	1000	710	425	20
S10	SiO_2	100	1000	710	425	20
S11	SiO_2	200	1000	710	425	20
S12	SiO_2	300	1000	710	425	20
S13	SiO_2	100	1000	710	325	20
S14	SiO_2	100	1000	710	225	20
S15	SiO_2	100	1000	710	125	20
S16	SiO_2	100	1000	710	100	20
S17	SiO_2	100	1000	710	25	20

Table A.3 *Growth parameters used for spinning coating.*

Sample ID	Substance	Spinning Speed (rpm)	Spinning Time (s)	Baking Temperature (°C)/ Time (min)	Lid position
S18	SC510K	2000	40	200/5	open
S19	SC800i	2000	40	200/5	closed
S20	SC800i	1500	20	200/5	open
S21	SC800i	1500	20	200/5	closed
S22	SC800i	2000	20	200/5	open
S23	SC800i	2000	20	200/5	closed
S24	SC800i	2500	20	200/5	open
S25	SC800i	2500	20	200/5	closed
S26	SC510K	1500	20	200/5	open
S27	SC510K	1500	20	200/5	closed
S28	SC510K	2000	20	200/5	open
S29	SC510K	2000	20	200/5	closed
S30	SC510K	2500	20	200/5	open
S31	SC510K	2500	20	200/5	closed

Table A.4 *Growth parameters for the manufactured AR coatings.*

Sample ID	Substance	Rate (nm/s)	T (°C)	p (mbar)	Current (mA)	Voltage (kV)
C1, C2	SiO_2	0.3	100	$5.2 \cdot 10^{-5}$	14	9.5
C1, C2	TiO_2	0.2	100	$1.8 - 2.0 \cdot 10^{-4}$	64	9.5
C3, C4	TiO_2	0.2	100	$1.8 \cdot 10^{-4}$	64	9.5
C5, C6	TiO_2	0.2	200	$1.8 - 2.0 \cdot 10^{-4}$	62	9.5
C7, C8	TiO_2	0.2	200	$1.8 \cdot 10^{-4}$	62	9.5
C9, C10	TiO_2	0.2	200	$1.8 \cdot 10^{-4}$	62	9.5
C7, C8	MgF_2	0.3	200	$3.2 \cdot 10^{-5}$	5–6	8
C9, C10	MgF_2	0.3	200	$3.2 \cdot 10^{-5}$	4–6	8
C9, C10	Al_2O_3	0.2	200	$3.2 \cdot 10^{-5}$	4–6	8
Sample ID	**Substance**	**T (°C)**	**p (mTorr)**	**NO_2 gas flow (sccm)**	**2%SiH_4/N_2 gas flow (sccm)**	**RF (W)**
C3, C4	SiO_2	100	1000	710	25	20
Sample ID	**Substance**	**Spinning Speed (rpm)**	**Spinning Time (s)**	**Baking Temperature (°C) / Time (min)**	**Lid position**	
C5, C6	SC510K	2000	20	200/5	closed	

B. Additional AFM Data

Topographical surface maps for every measured sample and the tabled results of their roughness analysis.

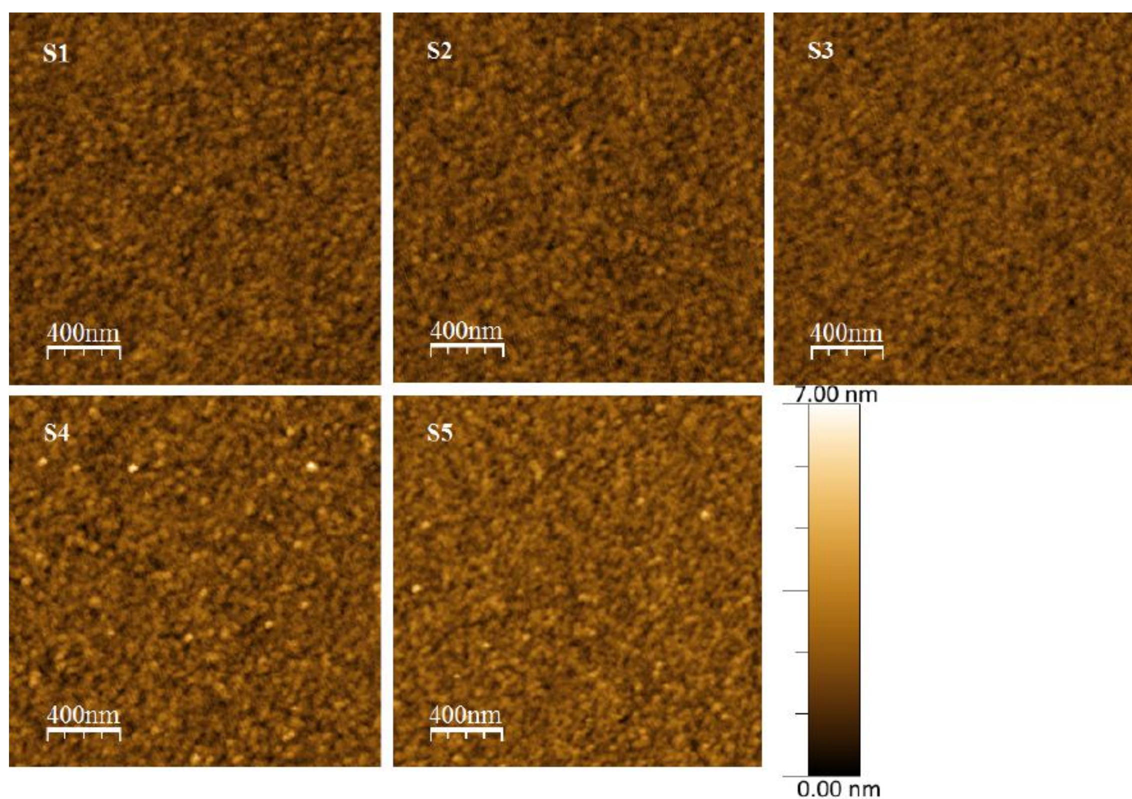

Figure B.1 *The results of AFM measurements for MgF_2 temperature series (samples S1-S5).*

Table B.1 AFM roughness analysis results for S1-S5.

Sample ID	rmsr (nm)	ra (nm)	<a> (nm)	S	K
S1	0.4752	0.3781	1.676	0.2632	3.1487
S2	0.4808	0.3828	1.681	0.2385	3.1505
S3	0.4371	0.3467	1.7403	0.126	3.1302
S4	0.5742	0.4406	1.8901	0.789	5.7657
S5	0.5633	0.4418	2.0701	0.4663	3.9673

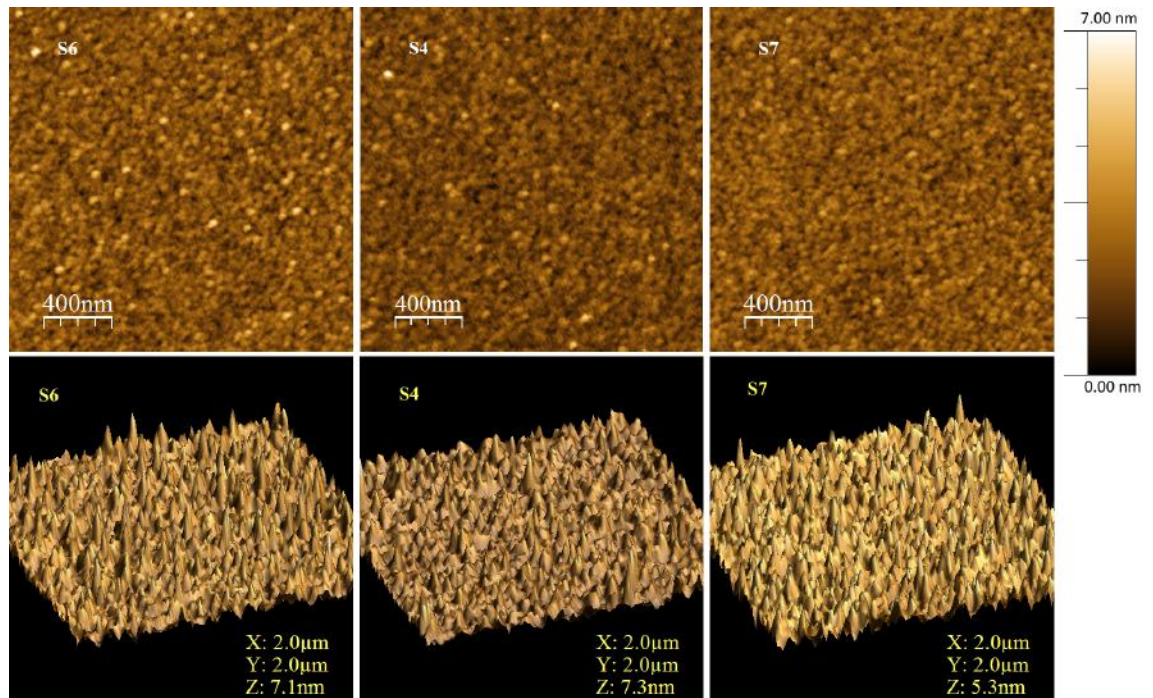

Figure B.2 AFM mappings for growth rate study of MgF_2. Upper row presents the 2D and lower row the 3D images for samples S4 (rate= 0.3), S6 (rate=0.1) and S7 (rate=0.5).

Table B.2 AFM roughness analysis for MgF_2 rate change series (S4,S6,S7).

Sample ID	rmsr (nm)	ra (nm)	<a> (nm)	S	K
S6	0.6907	0.5271	2.2246	0.8522	5.1719
S4	0.5765	0.4417	1.8888	0.821	5.709
S7	0.6031	0.4778	2.2063	0.3113	3.2587

Table B.3 *AFM roughness analysis results for annealing series done for sample S4 (T=200).*

Sample ID	rmsr (nm)	ra (nm)	<a> (nm)	S	K
S4 A0	0.5708	0.4393	1.8829	0.7167	5.2673
S4 A300	0.5834	0.4402	1.8262	1.0526	6.6656
S4 A700	5.4215	4.2331	16.4879	0.6648	3.8242
S4 A900	13.5078	10.8439	39.0587	0.3173	2.8915

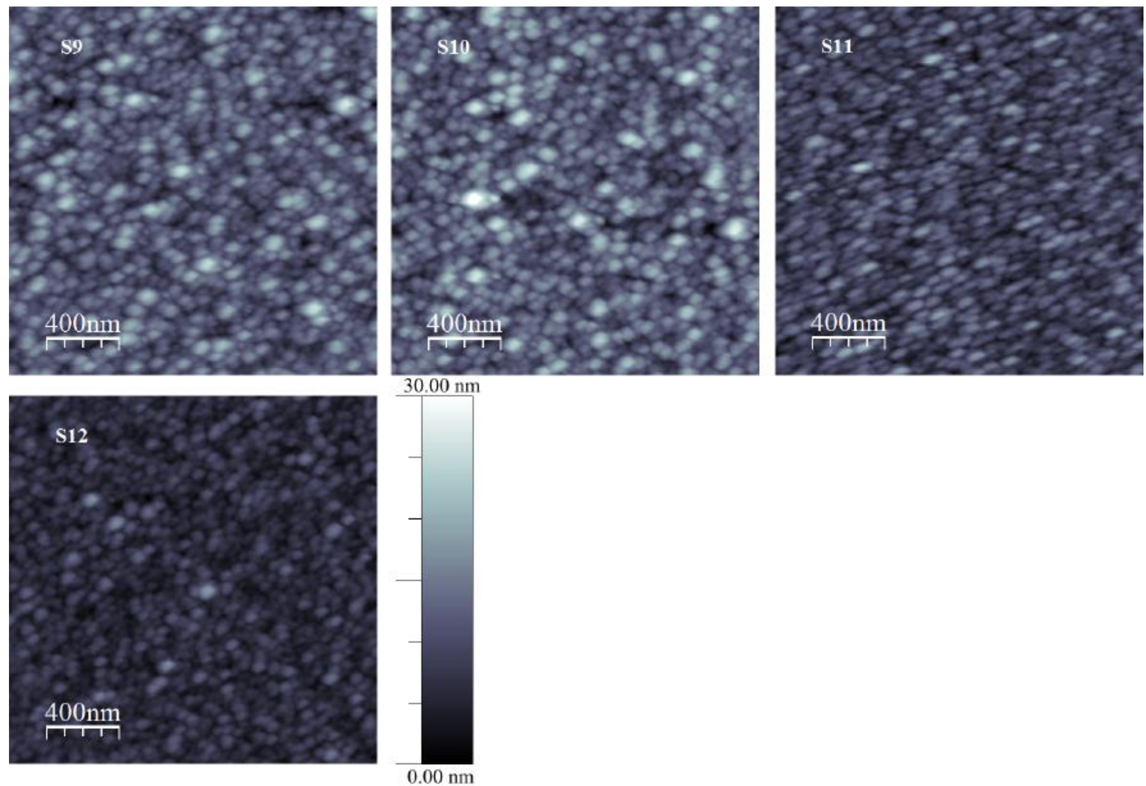

Figure B.3 *AFM scans for SiO_2 samples (S9-S12).*

Table B.4 *AFM roughness analysis results for SiO_2 samples S9-S12.*

Sample ID	rmsr (nm)	ra (nm)	<a> (nm)	S	K
S9	4.0811	3.1732	10.8139	0.7682	4.0194
S10	4.0613	3.1259	10.8017	0.9445	4.8912
S11	3.1062	2.4435	8.985	0.6318	3.5774
S12	2.1201	1.6528	5.4575	0.8919	4.5328

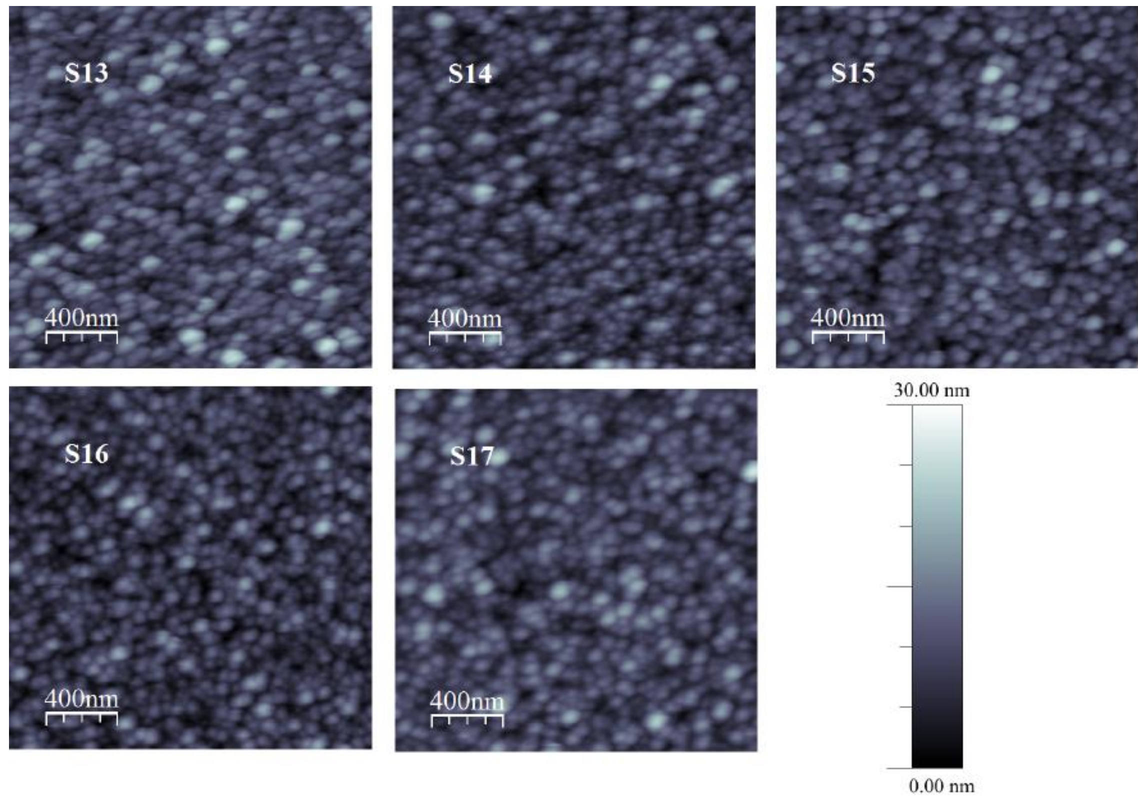

Figure B.4 *AFM scans for SiO_2 samples (S13–S17).*

Table B.5 *AFM roughness analysis results for SiO_2 samples S13–S17.*

Sample ID	**rmsr (nm)**	**ra (nm)**	**<a> (nm)**	**S**	**K**
S13	3.3468	2.6043	10.7659	0.6845	3.9351
S14	3.0612	2.4076	8.6062	0.6215	3.7109
S15	2.9749	2.3345	9.0103	0.5225	3.5882
S16	2.9259	2.3026	10.2875	0.5639	3.5002
S17	2.9364	2.2938	10.2251	0.5783	3.7521

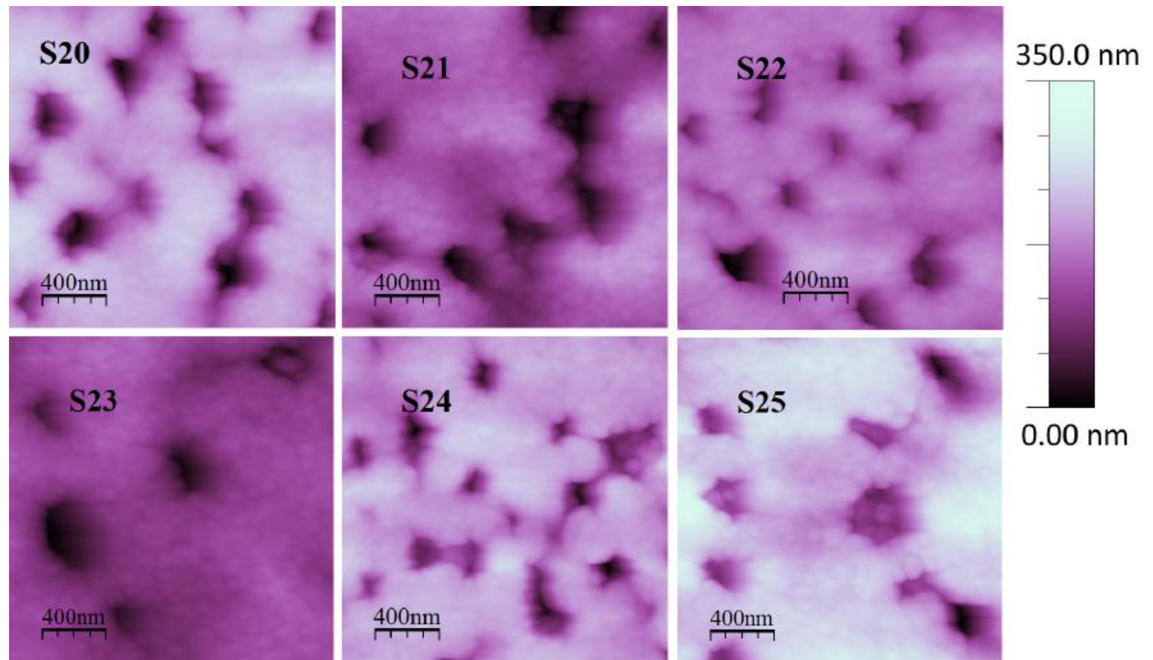

Figure B.5 *AFM scans for siloxane SC800i samples (S20–S25).*

Table B.6 *AFM roughness analysis results for SC800i samples S20–S25.*

Sample ID	rmsr (nm)	ra (nm)	<a> (nm)	S	K
S20	45.2458	34.2852	187.116	-1.4488	4.7691
S21	39.0614	31.2157	126.622	-0.7582	3.2052
S22	28.5963	19.9877	154.783	-1.7403	7.2377
S23	26.2603	20.0857	108.080	-0.9991	4.2372
S24	37.518	27.4703	184.159	-1.5474	5.5759
S25	40.5255	30.526	185.156	-1.1988	4.7204

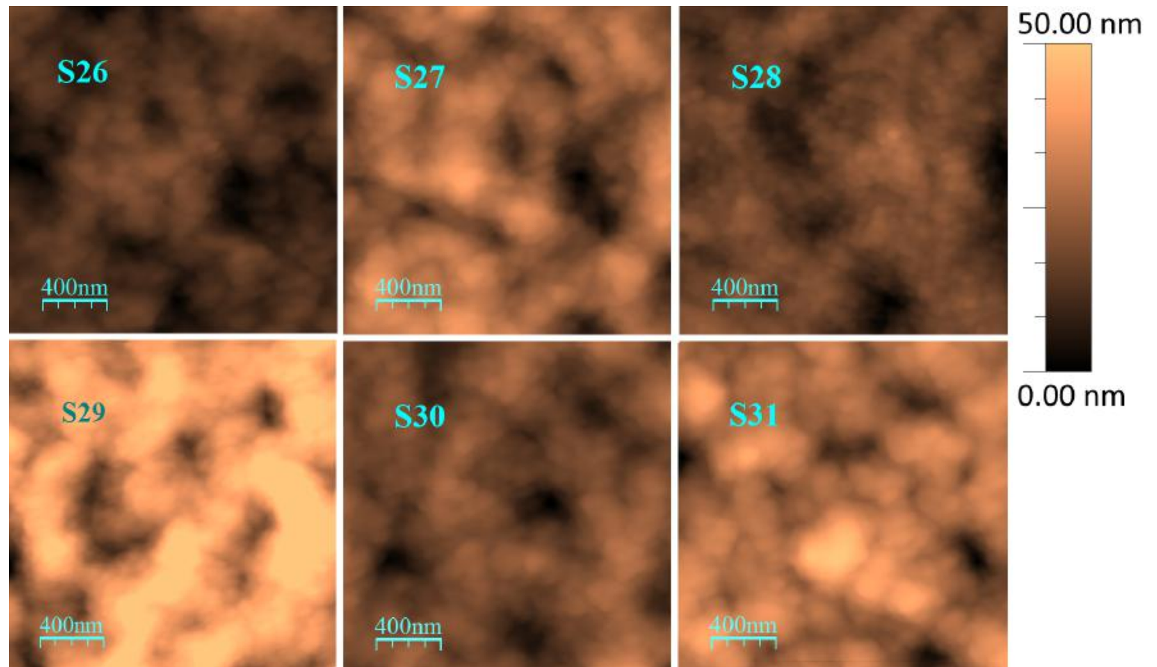

Figure B.6 *AFM scans for siloxane SC510K samples (S26–S31).*

Table B.7 *AFM roughness analysis results for SC510K samples S26–S31.*

Sample ID	rmsr (nm)	ra (nm)	<a> (nm)	S	K
S26	4.0713	3.2308	11.8721	-0.0997	2.8781
S27	6.8249	5.4665	23.9759	-0.3039	2.9779
S28	4.3738	3.4198	15.6998	-0.492	3.53
S29	10.4599	8.2838	38.4499	-0.314	2.9646
S30	4.9779	3.8873	18.1682	-0,2168	3.316
S31	7.1529	5.3955	28.1032	-0.2299	3.9394

C. Physical constants

Tabled values of widely used important physical constants.

Table C.1 *Some important physical constants*

Name	**Symbol**	**Value**
Avogadro's number	N_{Av}	$6.023 \cdot 10^{23}$ 1/mol
Boltzmann constant	k_b	$1.381 \cdot 10^{-23}$ J/K
Unit charge	e	$1.602 \cdot 10^{-19}$ C
Free electron mass	m_0	$9.109 \cdot 10^{-31}$ kg
Velocity of light in free space	c	$2.998 \cdot 10^{8}$ m/s
Permittivity of free space	ϵ_0	$8.854 \cdot 10^{-12}$ F/m
Permeability of free space	μ_0	$1.257 \cdot 10^{-6}$ H/m
Planck's constant	h	$6.625 \cdot 10^{-34}$ J·s
	$\hbar = h/2\pi$	$1.055 \cdot 10^{-34}$J·s